Summer 6-2011

COMPUTATIONAL MICROMECHANICS MODELING OF DAMAGE-DEPENDENT BITUMINOUS COMPOSITES BASED ON TWO-WAY COUPLED MULTISCALE APPROACH

Jamilla Lutif
University of Nebraska - Lincoln, jamilla@huskers.unl.edu

Lutif, Jamilla, "COMPUTATIONAL MICROMECHANICS MODELING OF DAMAGE-DEPENDENT BITUMINOUS COMPOSITES BASED ON TWO-WAY COUPLED MULTISCALE APPROACH" (2011). *Civil Engineering Theses, Dissertations, and Student Research*. 31.
http://digitalcommons.unl.edu/civilengdiss/31

COMPUTATIONAL MICROMECHANICS MODELING OF DAMAGE-DEPENDENT BITUMINOUS COMPOSITES BASED ON TWO-WAY COUPLED MULTISCALE APPROACH

by

Jamilla Emi Sudo Lutif

A DISSERTATION

Presented to the Faculty of
The Graduate College at the University of Nebraska
In Partial Fulfillment of Requirements
For the Degree of Doctor of Philosophy

Major: Engineering
(Civil Engineering)
Under the Supervision of Professor Yong-Rak Kim

Lincoln, Nebraska
June, 2011

COMPUTATIONAL MICROMECHANICS MODELING OF DAMAGE-DEPENDENT BITUMINOUS COMPOSITES BASED ON TWO-WAY COUPLED MULTISCALE APPROACH

Jamilla Emi Sudo Lutif, Ph.D.

University of Nebraska, 2011

Adviser: Yong-Rak Kim

This study presents a multiscale computational model with its verification and validation to mechanical behavior predictions of bituminous composites that are subject to fracture damage. Bituminous composites are classical examples of multi-phase composites in different length scales. The understanding of the mechanical behavior of asphaltic media has been a challenge to the pavement mechanics community due to multiple complexities involved: heterogeneity, anisotropy, nonlinear inelasticity, and damage growth in multiple forms. To account for this problem in an accurate and efficient way, this study proposes the use of the two-way coupled multiscale computational modeling technique.

The two-way coupled multiscale model is based on continuum thermo-mechanics and is implemented using a finite element formulation. Two length scales (global and local) are two-way coupled in the model framework by linking a homogenized global scale to a heterogeneous local scale representative volume element (RVE). With the unique multiscaling and the use of the finite element technique, it is possible to take into account

the effect of material heterogeneity, inelasticity, and anisotropic damage accumulation in the small scale on the overall performance of larger scale structures.

Along with the theoretical model formulation, several example problems are shown: some to verify the model and its benefits through comparisons with analytical solutions and single-scale simulation results, and others to validate the applicability of the approach to model bituminous composite where material viscoelasticity, mixture heterogeneity, and cohesive zone fracture are involved.

DEDICATION

To my husband, Victor Ferreira Teixeira, for his unconditional love.

AKNOWLEDGEMENTS

I would like to express my deepest gratitude to my advisor, Dr. Yong Rak Kim, for his excellent guidance during years of research, which contributed significantly to my education. His determination and focus on challenging research projects motivated me as a research assistant. With his constant encouragement and efforts I was able to accomplish many professional goals that made me grow as a researcher.

I also would like to express my gratitude to my supervisory committee, Dr. Raymond K. Moore, Dr. Christopher Tuan, Dr. Yong Cho, and Dr. Flavio Souza, for their technical support and reviews of this dissertation, providing me valuable comments. I am particularly grateful to Dr. Flavio Souza for kindly sharing his knowledge. Whenever I approached him with questions, he always answered patiently with great detail.

I would like to thank my co-workers, Dr. Hoki Ban, Francisco Aragao, Soohyok Im, Pravat Karki, Mohammad Haft Javaherian, and Jun Zhang, for their help in different stages of my research.

Thanks also go out to all friends that I made during this journey as a graduate student. Special thanks are due to my friends Mr. Flavio Souza and Mrs. Isabela Souza, Mr. Leonardo de Souza and Mrs. Ingryd Pinto, Mr. Felipe Loureiro and family, Mr. Ocelio Lima and Mrs. Michelle Lima, Mrs. Emmeline Watson, and Mrs. Andreia Bianchini for their friendship and joyful hours shared together.

I would like to express my sincere gratitude to my parents, Antonio Ramos Lutif and Elisa Massa Sudo Lutif, to my brothers, Herickson Akihito Sudo Lutif and Samir Yuji Sudo Lutif, and to my sister, Ellen Yoshie Sudo Lutif, for their love and words of encouragement. Finally, I would like to thank my husband, Victor Ferreira Teixeira, for always being patient and kind throughout my Ph.D. program, giving me love and support by any means.

GRANT INFORMATION

I would like to acknowledge the financial support provided by the National Science Foundation under grant number CMMI-0644618.

Table of Contents

List of Figures

List of Tables

Chapter 1

Introduction

It is well known that the economical development of a country is directly affected by its transportation system. Roadways are used to transport people and products from one point to another. From an economic perspective, travel time accounts for almost half of all costs experienced by highway users. The United States has the largest network of roadways of any country with a total length of about 6.5 million kilometers. From that, 4.2 million kilometers are considered paved roadways, of which 94% are asphalt surfaced.

Even though 65% are considered paved, the majority of U.S. roadways require maintenance before reaching their design life. According to the American Association of State Highway and Transportation Officials (AASHTO, 2009), 50% of the roads are rated as in bad condition, which increase not only the travel time spent by the users on site but also the maintenance costs on their vehicles.

Cumulative distresses, such as permanent deformation, fatigue cracking, raveling, and stripping, are visible on the pavement surface layer. The excessive distresses lead to major areas of deteriorations like potholes (Figure 1). Those distresses are a result of a combination of various factors, i.e., improper choice of material combinations (percentage of asphalt binder and aggregates, aggregate’s gradation and source, etc), excessive traffic loadings (more or heavier loads than anticipated in design), environmental effects (moisture conditions, seasonal climate changes), etc. Thus, pavement design methods need to take into consideration those factors in order to obtain reliable structures.

Figure 1: Potholes formed due to excessive fatigue cracking and permanent deformation.

The large damaged areas (macrocracks, surface depressions, potholes, etc) observed on the pavement surface layer usually arise after the combination of small scale phenomena (microcracks, aggregate particles interactions, and mixture constituents accommodation). Thus, it is important to understand when, where, and why the microscale damage will initiate and propagate. Figure 2 illustrates the formation of macrocracks after the coalescence of microcracks at the smaller scale.

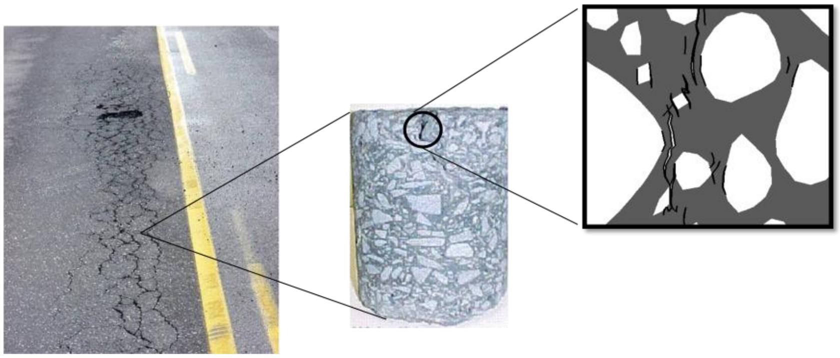

Figure 2: Macrocracks formation due to microcracks.

Department of roads usually rely on extensive and costly laboratory tests to determine whether or not asphalt mixtures would be appropriate for field applications. The results from performance tests to access mixture’s moisture resistance and rutting susceptibility have been used as pass/fail criteria of asphalt mixtures. Those results can be useful in ranking different material combinations; however, the phenomena that occur inside the specimens (aggregate and asphalt binder interactions, and crack initiation and propagation) that lead to either a successful or a weak blend of materials cannot be fully assessed.

There is a need for mechanistic models that can account for the existing complexities of asphaltic composites, e.g., heterogeneity, anisotropy, nonlinear inelasticity, and damage growth in multiple forms.

Some researchers use the so-called continuum damage models to predict the fracture behavior of asphalt composites. The composite overall damage-dependent behavior is accounted by the use of internal variables, which are phenomenologically defined after a fitting process of experimental results with the assumed damage evolution model. Although this approach is relatively simple to apply, it does not account for the interactions among materials constituents and the creation of internal boundaries (such microcracks). Besides, it requires extensive laboratory performance tests for every combination of materials and applied loading conditions.

Alternatively, other researchers have been using computational microstructure approaches with discrete fracture involved to predict the damage-dependent behavior of bituminous composites. In those models, the material heterogeneity can be taken into account and crack initiation and growth can be predicted during the analysis. However, bituminous mixtures typically contain thousands of irregularly-shaped, randomly-oriented aggregate particles along with thousands of potential cracking sites. The solution for such a problem would require the use of a tremendous amount of computational time and effort, which is rarely feasible with the computing power currently available. Therefore, there is a pressing need for reliable models that could account for mixture complexities yet using a fair computational effort.

One approach, which has been receiving attention from the mechanics community, is that of computational micromechanics multiscale modeling. In this approach, different length scales within the macroscopic structure are separately analyzed and then linked together. A micromechanics problem is solved at the smaller scale using only basic constituent properties, and, when statistical homogeneity on the smaller scale representative volume element (RVE) is satisfied, constitutive equations for the larger scale can be produced using a homogenization principle. Therefore, the global constitutive behavior of heterogeneous materials can be determined by the solution of a micromechanical boundary value problem of the smaller scale RVE, reducing considerably the computational time required to solve the problem compared to the ones in the single scale microstructure models.

1.1 Research Objectives

The main objective of this dissertation is to model bituminous composites using a computational micromechanics model based on two-way coupled multiscale. Since the large scale damage is associated with small scale phenomena, it is fundamental to understand not only the interactions among material constituents, but also the initiation and propagation of internal boundaries, which may lead to major distresses on asphaltic structures. That said, better material combinations and/or sources can be chosen leading to more reliable designs.

More specifically, the research objectives are as follows:

- Verify the two-way coupled multiscale model by comparing numerical results with analytical solutions developed;
- Develop a procedure to determine representative volume element (RVE) for bituminous composites using image analysis techniques;

- Obtain fundamental material properties experimentally to be used as input on the multiscale model;

- Validate the two-way couple multiscale model to predict the damage-dependent behavior of laboratory-fabricated bituminous mixture;

- Investigate damage evolution characteristics on bituminous composites.

- Perform a parametric analysis to verify the influence of important design variables on the bituminous composite mechanical response.

1.2. Organization of Dissertation

Following this introduction, this dissertation is organized as follows. *Chapter 2* is dedicated to literature review of the main modeling approaches applied to predict mechanical behavior of bituminous composites. *Chapter 3* consists of the description of the two-way coupled multiscale computational model used and verification by means of comparisons of closed-form solution problems with numerical results. In *Chapter 4* the laboratory testing methods required for the model validation are described. Details about bituminous composite specimen geometry and material properties, as well as the loading conditions used in the bending beam tests for model validation are shown. Furthermore, required fundamental material properties for local scale analysis are pointed-out altogether with suggested laboratory testing methods to obtain the material parameters.

Chapter 5 is focused on the determination of bituminous composite representative volume elements through the use of image analysis of bituminous composite internal structure as well as the analysis of effective properties of the composite based on finite element simulations. *Chapter 6* consists of validation-calibration of the model to predict damage-dependent behavior of laboratory fabricated asphaltic composites. Comparisons of experimental results with numerical results are presented. In *Chapter 7*, a parametric analysis of some design variables to study their impact on the overall bituminous composite behavior is performed. Finally, in *Chapter 8* the outcomes from this dissertation and concluding remarks are drawn.

Chapter 2

Literature Review

Composite materials have been widely used in many engineering applications, such as in aircrafts, tank armors, commercial and residential buildings, bridges, pavement structures, and many others. Composites are made of two or more constituent materials, and the overall structural performance of the composite when it is subject to mechanical loads can be improved by taking advantage of the characteristics of the constituents. Understanding the contribution of the constituent phase on the overall behavior of the composite is of fundamental importance.

Bituminous composite is an example of a composite material that is made by combining aggregate particles, an asphalt binder, and voids. Additives such as styrene-butadiene-styrene (SBS), warm mixture additives, hydrated lime, and others can also be incorporated into the mixture to enhance other characteristics of the composite. Figure 3 illustrates a typical cross section of a bituminous specimen fabricated in a laboratory.

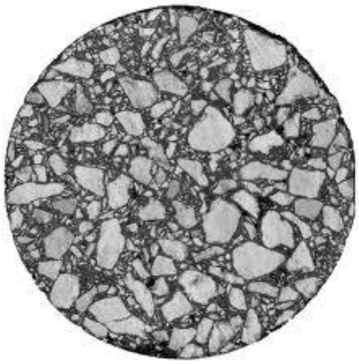

Figure 3: Typical cross-section area of a laboratory fabricated bituminous specimen.

Understanding the mechanical behavior of bituminous composites has been a challenge to the civil engineering community due the existence of multiple complexities: heterogeneity, anisotropy, nonlinear inelasticity, and damage growth in multiple forms. The role played by each constituent material and its effects on the overall behavior of the composite needs to be carefully investigated.

Many investigative approaches have been developed by the scientific community. The two main modeling techniques used to predict damages in asphalt composites are the continuum damage technique and the discrete fracture technique that considers the microstructure of the composite. Advantages and shortcomings exist in both techniques when modeling the bituminous composite.

2.1 Continuum Damage Modeling

The continuum damage models have been commonly used to determine the damage behavior of asphaltic composites. In such models, asphalt composites are treated as homogenous bodies. In those models, microstructure analysis is not performed, but structural degradations in the microstructures are considered in a homogenized way using internal state variables.

The choice of the functional form for the damage evolution function is somewhat arbitrary. Generally, damage parameters are phenomenologically determined by matching experimental testing results with damage evolution characteristics. Thus, the use of the continuum damage approach could be cumbersome because large numbers of experimental tests would be required to produce statistically derived empirical functions to predict the damage-dependent asphalt behavior. In addition, the damage parameters depend on the mixture and loading type, which means that for every analysis of a specific mixture and/or loading of interest, another large set of experimental tests would be required.

Even though this approach presents some limitations, many researchers have been using it to characterize the structural degradation of asphalt media due its simplicity (Schapery, 1990; Park *et al.*, 1996; Lee and Kim, 1998; Lee *et al.*, 2000; Christensen, 2002; Daniel and Kim, 2002; Chehab *et al.*, 2003; Gibson *et al.*, 2003; Tashman *et al.*, 2004; Masad *et al.*, 2005).

Because the cracks do not need to be explicitly modeled in the continuum damage approach, the computational effort is tremendously reduced compared to that required in the discrete fracture based models. Thus, the use of continuum damage models can be an alternative for asphaltic composite modeling. However, those models do not fully account for the fundamental characteristics, particularly the formation of numerous cracks on multiple length scales.

2.2. Microstructure Models with Discrete Fracture

Microstructure models have been receiving attention from the asphalt mechanics community. Using this approach, the effects of material heterogeneity is taken into account by addressing the mixture constituents separately. Thus, the interactions of individual components on the overall behavior of asphalt mixtures with regard to heterogeneity and anisotropy can be carefully investigated. Effects of changes in internal variables (such as volume fraction, particle size distribution and orientation) on the overall composite response can be evaluated without having to perform costly and time-consuming large-scale mechanical tests.

Furthermore, the addition of the discrete fracture model into the microstructure approach allows the prediction of the formation and growth of internal boundaries (cracks) during analysis. One well-known approach to model cracks is the cohesive zone model. The cohesive zone model uses mathematical formulations to remove stress singularities ahead of the crack tip. Thus, the fracture behavior of materials can be regarded as a gradual phenomenon in which separation takes place across an extended crack tip or cohesive zone (also called the fracture process zone), where fracture is resisted by cohesive tractions. More details about cohesive zone models will be described in section 2.4 of this chapter.

2.3. Micromechanics Multiscale Approach with Discrete Fracture

Although the microstructure models appear to be suitable for prediction of bituminous composites behavior, it requires an impractical number of degrees of freedom in order to discretize all heterogeneities that typically exist in bituminous mixtures.

In an attempt to improve the efficiency of microstructure-based models, some researchers have been using computational micromechanics multiscale models, as demonstrated in many studies (Feyel and Chaboche, 2000; Fish and Wagiman, 1993; Fish and Shek, 2000; Ghosh and Raghavan, 2001; Oden et *al.*, 1999; and Haj-Ali and Muliana, 2004; Souza and Allen, 2011; Lutif *et al*., 2010). In the multiscale approach, different length scales within the macroscopic structure are analyzed separately and then linked together.

The main goal of the multiscale modeling is to determine the locally averaged global constitutive behavior of a composite by taking into account the phenomena that occur on the smaller scales. By applying the two-way coupled multiscale modeling approach to a multiple scale problem, the constitutive behavior of the global structure can be obtained by the solution of a boundary value problem of the smaller scale RVE. Different length scales are linked by applying homogenization principles (Christensen, 1979; Mura, 1987; Nemat-Nasser and Hori, 1993; and Allen, 2001). Thus, the role played by each material constituent is accounted for at the local scale level, and homogenized tensors are transferred back to the larger scale structure. Thus, the heterogeneity is still considered in this analysis with no need to discretize all heterogeneities of the global structure.

Therefore, to accomplish the two-way coupled multiscale modeling with a certain degree of accuracy, appropriate representative volume elements (RVEs) must be identified, given that the effective properties of a heterogeneous bulk mixture are obtained by a homogenization process of a heterogeneous RVE. An RVE is defined as the smallest but sufficiently large volume element that can represent the effective properties of the large-scale composite. Thus, the mechanical analysis of large heterogeneous asphalt composite can be reasonably converted into the mechanical analysis of much smaller heterogeneous mixtures, since the selected smaller sample (RVE) is sufficient to reflect the overall statistically homogeneous behavior of the large-scale bituminous composite.

One of primary requirements for an appropriate RVE is statistical homogeneity: in other words, the averaged characteristics (mechanical or geometrical) in an RVE should be statistically homogeneous so that the bulk sample characteristics and the RVE characteristics are the same. In the case of complex particulate composites such as asphalt composites, where aggregate particles in various shapes and sizes are dispersed randomly in the asphalt binder, the identification of an appropriate RVE is not trivial due to the significant geometric complexity of the mixture. Several mixture variables need to take into consideration during the analyses to properly define the RVE size.

2.4. Cohesive Zone Models

The modeling of a fracture with discrete cracks is not trivial. The first attempts to predict crack growth in a material was attributed to Griffith (1920). In his model, the author assumed that a crack initiated whenever the material energy release rate was greater than the critical energy release rate, which was a material property. Another important assumption in Griffith's theory was that plastic deformations were negligible. Thus, Griffith's theory was known as the linear elastic fracture mechanics (LEFM).

However, some materials are extremely ductile and undergo significant nonlinear inelastic deformation before reaching complete failure, which is the typical case in bituminous composites. To account for the nonlinear constitutive behavior of materials, cohesive zone models have been used by many researchers (e.g., Dugdale, 1960; Barenblatt, 1962; Needleman, 1987; Schapery, 1975; Tvergaard, 1990; Costanzo and Allen, 1993; and Allen and Searcy, 2001).

The cohesive zone is defined as the potential damage zone ahead of a crack tip, where cohesive tractions are developed to resist fracture. As a result, the initiation and growth of internal boundaries (cracks) can be analyzed before the total fracture of the material occurs. Figure 4 presents a schematic illustration of the cohesive zone in an object in mode I fracture (opening of the crack faces).

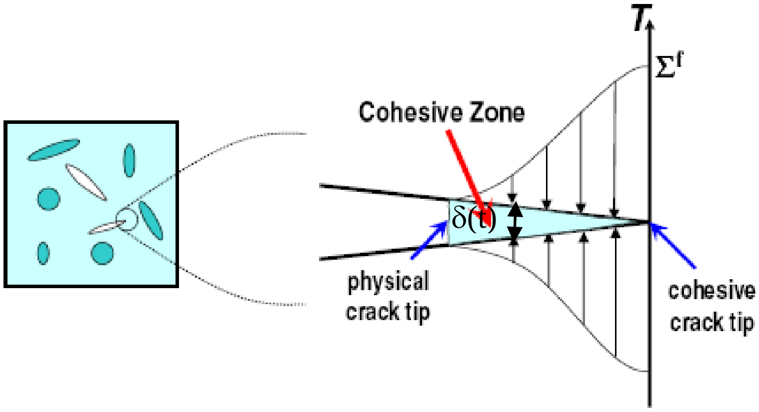

Figure 4: Schematic illustration of cohesive zone at the crack tip.

Based on the cohesive zone concept, separation starts when a maximum traction ($T_{\max}$) is reached. Then, the tractions decrease until they become null, and full separation occurs (at the critical cohesive displacement, δ_c). The constitutive relations, $T(\delta)$, between cohesive tractions and displacements are defined as softening curves. Various softening functions have been proposed in the literature and differ mainly in two characteristics, i.e., i) the existence of an initial cohesive stiffness and ii) the shape of the softening curve. Figure 5 illustrates some cohesive zone models with three distinct initial stiffness values and shapes used to model the behavior of composite media.

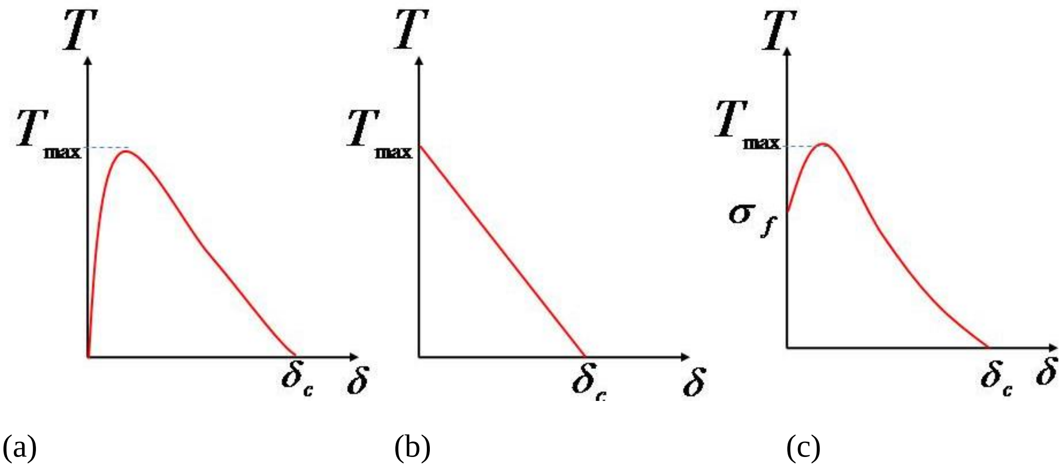

(a) (b) (c)

Figure 5: Examples of traction-displacement models for cohesive zones; a)Tvergaard (1990), b) Camacho and Ortiz (1996), c) Allen and Searcy (2001).

Models that assume an artificial initial stiffness (e.g., Figure 5a) are called intrinsic models, while models that assume an initial rigidity (e.g., Figure 5b and c) are called extrinsic models. Although the intrinsic models are easier to be implemented in a finite element formulation, they can be cumbersome because they require the insertion of cohesive elements a priori in the mesh. In the case of extrinsic formulations, the cohesive zones are inserted by an adaptive process as the stress initiation criteria are reached, which is a more realistic representation of the physical phenomena.

Regarding the shape of the curves, Figure 5a presents a polynomial softening function of the third degree, first described by Needleman (1987) for the pure normal separation and then extended by Tvergaard (1990) for mixed-mode loading. This model is one of the most popular cohesive zone models used to predict cracks in ductile materials. A purely decreasing linear law, mainly used to predict the behavior of brittle materials, was described by Camacho and Ortiz (1996), as shown in Figure 5b. This law assumes infinite stiffness in the cohesive zones until the maximum traction is reached. Then, the cohesive zone stress starts to decrease linearly until the critical displacement criteria are reached. In Figure 5c, a non-linear viscoelastic softening model proposed by Allen and Searcy (2001) is presented. In this model, cohesive zone elements are inserted in the body if the stress in the material reaches certain level, σ^f, defined as a requisite stress level to initiate damage. Then, cohesive elements still present certain strength until the cohesive tractions reach a maximum, $T_{\max}$. After that, the cohesive tractions start to gradually decrease until they finally vanish (at the critical cohesive displacement criteria).

Bituminous composites typically present nonlinear viscoelastic fracture process which has been demonstrated by numerous studies (Kim *et al.*, 2007; Kim *et al.*, 2006; Souza *et. al.*, 2004; Freitas, 2007). Thus, for this study, the extrinsic non-linear viscoelastic traction-displacement model proposed by Allen and Searcy (2001) was adopted. More details about this model are presented in the next chapter.

Chapter 3

Multiscale Model

The multiscale computational model used herein is based on the finite element method. In this approach, a two-way coupling strategy is adopted: i) the state of deformation observed on the global structure is passed to the boundary of the RVE and ii) once the local scale initial boundary value problem is solved for the applied loading (coming from the global scale), the homogenized material properties, or homogenized stresses, are passed back to the global scale (Souza *et al.*, 2008; Souza, 2009; Souza and Allen, 2010). The two-way coupling is especially important when evolving microstructures, such as microcracks, are involved because the evolution process could be not only spatially but also time dependent.

Thus, the larger scale structure (global scale) can be idealized as a homogeneous material which dramatically reduces the mesh refinement. Consequently, the required computational time would be reduced while the smaller scale body (local scale) is considered heterogeneous. It is important to note that, from a computational point of view, a local scale RVE is attached to each global scale integration point of the selected global scale finite element.

3.1. Global Scale Initial Boundary Value Problem

As mentioned earlier, the main goal of the two-way coupled multiscale modeling is to determine the locally averaged global constitutive behavior of a composite by taking into account the phenomena that occur on the smaller scales. Consider an object of volume V and a boundary ∂V, which is divided into two parts, ∂V_t (where the traction boundary conditions are known) and ∂V_u (where the displacement boundary conditions are specified), as shown in Figure 6.

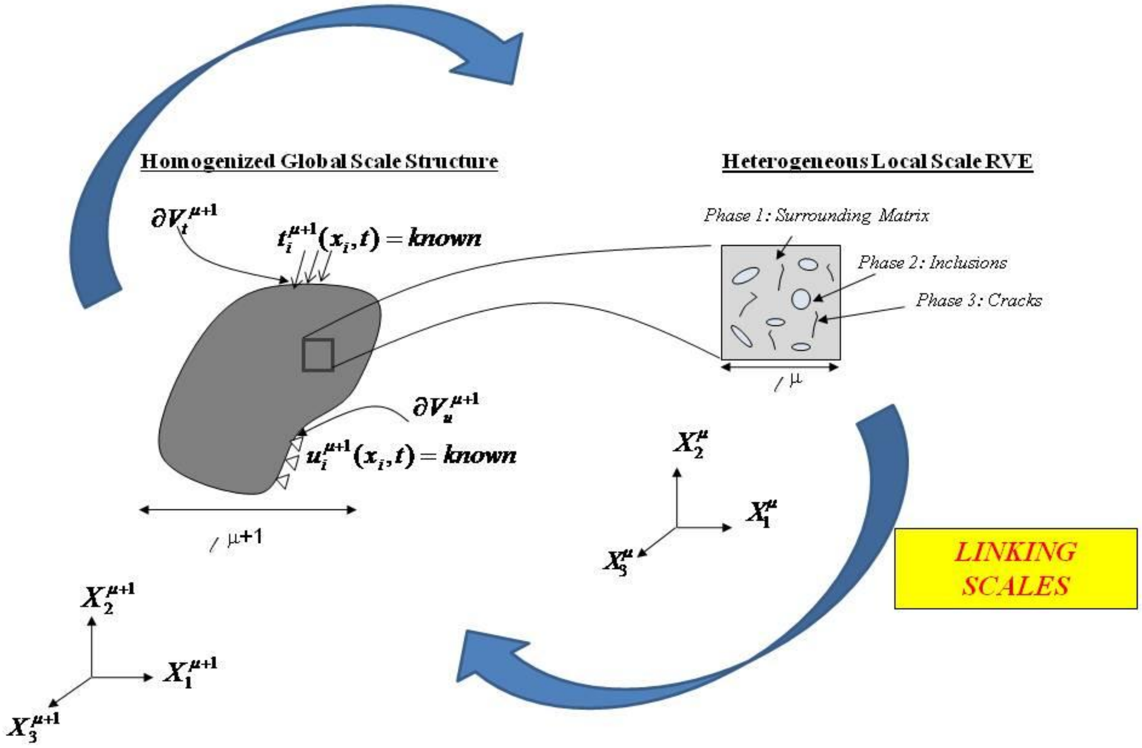

Figure 6: Multiscale Modeling with Two Scales.

The object is statistically homogeneous at the global scale but heterogeneous at the local scale RVE. The primary variables used in the model are the following: the displacement vector $u_i\ (x_k, t)$, the strain tensor $\varepsilon_{ij}\ (x_k, t)$, and the Cauchy stress tensor $\sigma_{ij}\ (x_k, t)$, where t and x_k are independent variables related to time and spatial coordinate, respectively. The superscripts μ and $\mu+1$ are used to denote the global scale (problem of interest) and local scale (RVE), respectively. The subscripts are used to denote the conventional rectilinear coordinate system.

The problem is assumed to be quasi-static in both length scales. Thus, the initial boundary value problem (IBVP) for the global scale can be posed as follows:

3.1.1. Conservation of Linear Momentum

$$\sigma_{ji,j}^{\mu+1} + \rho f_i^{\mu+1} = 0 \text{ in } V^{\mu+1} \tag{3. 1}$$

where superscript $\mu+1$ refers to the global scale, ρ is the material density, and $f_i^{\mu+1}$ represents the body force per unit mass.

3.1.2. Kinematics

Assuming that the deformations are infinitesimal, the strain-displacement relationship can be written as:

$$\varepsilon_{ij}^{\mu+1} = \frac{1}{2}\left(u_{i,j}^{\mu+1} + u_{j,i}^{\mu+1}\right) \text{ in } V^{\mu+1} \tag{3. 2}$$

3.1.3. Constitutive Equations

$$\sigma_{ij}^{\mu+1}\left(x_k^{\mu+1},t\right)=\Omega_{\tau=0}^{\tau=t}\left\{\varepsilon_{kl}^{\mu+1}\left(x_k^{\mu+1},t\right)\right\} \text{ in } V^{\mu+1} \tag{3. 3}$$

where τ is the time scale and Ω is a functional mapping of the entire history of strain at any point in the body. In the case of the global scale, Ω is determined from the locally averaged constitutive behavior of the RVE.

3.1.4. Initial Conditions

$$u_i^{\mu+1}\left(x_k^{\mu+1},0\right)=0 \tag{3. 4}$$

$$\varepsilon_{ij}^{\mu+1}\left(x_k^{\mu+1},0\right)=0 \tag{3. 5}$$

$$\sigma_{ij}^{\mu+1}\left(x_k^{\mu+1},0\right)=0 \tag{3. 6}$$

3.1.5. Boundary Conditions

$$t_i^{\mu+1}\left(x_k^{\mu+1},t\right)=\hat{t}_i \text{ in } \partial V_t^{\mu+1} \tag{3. 7}$$

$$u_i^{\mu+1}\left(x_k^{\mu+1},t\right)=\hat{u}_i \text{ in } \partial V_u^{\mu+1} \tag{3. 8}$$

3.2. Local Scale Initial Boundary Value Problem

The same set of governing equations used to pose the global scale IBVP can be applied to the local scale IBVP. However, some assumptions and simplifications regarding the local scale boundary conditions are necessary to produce reasonably accurate predictions through the multiscale process. One of the assumptions is that the global length scale needs to be much larger than the local length scale, allowing the use of spatially homogeneous boundary conditions (in this study, linear boundary displacements are applied to the RVE boundaries) (Mura, 1987):

$$l^{\mu+1} >> l^{\mu} \tag{3. 9}$$

The second assumption is that the length scale associated with the cracks is much smaller than the local scale length. This assumption is important to guarantee statistical homogeneity in the RVE.

Thus, the local scale IBVP for the local RVE is well posed by uniform initial boundary conditions and the following set of governing equations:

$$\sigma^{\mu}_{ji,j} + \rho f_i^{\mu} = 0 \text{ in } V^{\mu} \tag{3. 10}$$

$$\varepsilon^{\mu}_{ij} = \frac{1}{2}\left(u^{\mu}_{i,j} + u^{\mu}_{j,i}\right) \text{ in } V^{\mu} \tag{3. 11}$$

$$\sigma^{\mu}_{ij}\left(x^{\mu}_{k}, t\right) = \Omega^{\tau=t}_{\tau=0}\left\{\varepsilon^{\mu}_{kl}\left(x^{\mu}_{k}, \tau\right)\right\} \text{ in } V^{\mu} \tag{3. 12}$$

$$G^{\mu}_{m} \geq G^{\mu}_{cm} \text{ in } V^{\mu} \tag{3. 13}$$

where the subscript μ refers to the local scale, G^{μ}_{m} is the fracture energy release rate at a certain position and time, G^{μ}_{cm} is the critical energy release rate of the material, and the subscript m refers to the mode of fracture.

The functional mapping $\Omega_{\tau=0}^{\tau=t}$ is known a priori for all local scale material constituents. In this study, the RVE is defined as a composite made of three different material phases, i.e., i) aggregates, which are assumed to be linear-elastic; ii) asphalt matrix, which is assumed to be linear-viscoelastic; and iii) cohesive zones, whose behavior is described by a traction-displacement relationship. The constitutive equations for the linear-elastic and linear-viscoelastic materials are described as follows, respectively:

$$\sigma_{ij}^{\mu}(x_k,t) = E_{LE}^{\mu}\varepsilon_{kl}^{\mu}(x_k,t) \tag{3. 14}$$

$$\sigma_{ij}^{\mu}(x_k,t) = \int_0^t E_{LVE}^{\mu}(t-\tau)\frac{\partial \varepsilon_{kl}^{\mu}}{\partial \tau}d\tau \tag{3. 15}$$

where E_{LE}^{μ} is the linear-elastic modulus tensor, which is not time-dependent; t is the time of interest; $E_{LVE}^{\mu}$is the time-dependent linear-viscoelastic relaxation modulus tensor; and τ is the time-history integration variable.

For the cohesive zones, the following non-linear rate dependent traction-displacement relationship developed by Allen and Searcy (2001) is assumed herein:

$$T_i^{\mu}(t) = \frac{1}{\lambda^{\mu}}\frac{\delta_i^{\mu}}{\delta_i^{*\mu}}\left[1-\alpha^{\mu}(t)\right]\left\{\sigma_i^{f\mu} + \int_0^t E_{cz}^{\mu}(t-\tau)\frac{\partial \lambda^{\mu}}{\partial \tau}d\tau\right\} \text{ in } \partial V_{cz}^{\mu} \tag{3. 16}$$

where T_i^{μ} is the traction acting on the cohesive zone boundary; δ_i^{μ} is the cohesive zone opening displacement; $\delta_i^{*\mu}$is the material length parameter, which typically reflects a length intrinsic to the scale of the damage zone; $\alpha^{\mu}(t)$ is the internal damage parameter, which represents the time-varying area fraction of the growing voids with respect to the cross-sectional area of the idealized cohesive zone; $\sigma_i^{f\mu}$ is the required stress level to initiate damage; E_{cz}^{μ} is the time-dependent relaxation modulus of the cohesive zone; and λ^{μ} is the Euclidean norm of the damaged zone opening displacements, and it is given by:

$$\lambda(t) = \sqrt{\left[\frac{\delta_n(t)}{\delta_n^*(t)}\right]^2 + \left[\frac{\delta_t(t)}{\delta_t^*(t)}\right]^2 + \left[\frac{\delta_r(t)}{\delta_r^*(t)}\right]^2} \tag{3. 17}$$

where subscripts n, t and r refer to the normal, tangential and radial components of the damage zone opening displacements, respectively.

An internal variable damage evolution law is necessary to complete the cohesive zone traction-displacement relationship. Conceptually, when the internal damage parameter $\alpha^{\mu}(t)$ reaches unity, the traction vector becomes zero and implies that a free surface is created or, equivalently, that a crack has propagated (Souza, 2009). According to Allen and Searcy (2001), a simple phenomenological damage law, which is a generalization of the continuum damage evolution formulation proposed by Kachanov (1958) and Rabotanov (1969), can express the diminishing damage zone volume fraction given by:

$$\dot{\alpha} = A\lambda^m \text{ when } \dot{\lambda} > 0 \text{ and } \alpha < 1 \tag{3. 18}$$

$$\dot{\alpha} = 0 \text{ when } \dot{\lambda} \leq 0 \text{ or } \alpha = 1 \tag{3. 19}$$

where A and m are material parameters.

3.3. Homogenization Principles Connecting Different Length Scales

To establish a link between the global and local scales, some mathematical relationships that relate stress and strain field variables of the local length scale to those of the global length scale are required. One approach to link both scales is through the use of mean field theories. Consider the notational operator for a generic function, *f*:

$$f\left(x_i^{\mu+1}, t\right) \equiv \frac{1}{V^{\mu}} \int_{V^{\mu}} f\left(x_i^{\mu}, t\right) dV \tag{3.20}$$

Using the divergence theorem and conservation of linear momentum, the volume integral of the stress field can be transformed into a surface integral equation. Therefore, if the boundary conditions at the local scale are homogeneous, the homogenized stresses at the global scale in terms of the local stresses can be written as follows (Allen, 2001):

$$\sigma_{ij}^{\mu+1} = \bar{\sigma}_{ij}^{\mu} = \frac{1}{V^{\mu}} \int_{V^{\mu}} \sigma_{ij}^{\mu} dV \tag{3.21}$$

The local scale homogenized strains are described in terms of two components:

$$\bar{\varepsilon}_{ij}^{\mu} = \frac{1}{V^{\mu}} \int_{V^{\mu}} \varepsilon_{ij}^{\mu} dV = \varepsilon_{ij}^{\mu+1} + \alpha_{ij}^{\mu+1} \tag{3.22}$$

The first component, $\varepsilon_{ij}^{\mu+1}$, represents the homogenized strains at the RVE boundary, while the second component, $\alpha_{ij}^{\mu+1}$, takes care of the RVE internal boundaries due to heterogeneities and cracks. Thus, they can be described as follows:

$$\varepsilon_{ij}^{\mu+1} = \frac{1}{V^{\mu}} \int_{\partial V_E^{\mu}} \frac{1}{2}\left(u_i^{\mu} n_j^{\mu} + u_j^{\mu} n_i^{\mu}\right) dS \tag{3. 23}$$

$$\alpha_{ij}^{\mu+1} = \frac{1}{V^{\mu}} \int_{\partial V_I^{\mu}} \frac{1}{2}\left(u_i^{\mu} n_j^{\mu} + u_j^{\mu} n_i^{\mu}\right) dS \tag{3. 24}$$

where ∂V_E^{μ} and ∂V_I^{μ} are the external and internal boundaries of the local length scale, respectively, and $n_{\boldsymbol{k}}^{\mu}$ denotes the unit outer normal vector to the volume of the local scale body.

Finally the constitutive relationship between global and local length scales needs to be establish. This can be done by the direct substitution of the local scale constitutive equation (Equation 3.12) into the volume average of stresses (Equation 3.21). Furthermore, in the two-way couple multiscale approach, there is no need to determine the global scale constitutive tensor, $C_{ijkl}^{\mu+1}$, since it is determined concurrently as the analysis is performed by solving the local scale IBVP.

Souza (2009) and Souza and Allen (2009) introduced a new quantity, the so-called localization tensor, λ_{ijk}^{μ}, which relates the local displacement field to the deformation on the external boundary of the RVE. This is the key feature that allows the computation of the full homogenized anisotropic tangent constitutive tensor (Souza and Allen, 2010). In the case of viscoelastic materials, the following incremental constitutive relation has been obtained as follows (Souza and Allen, 2010; Souza, 2009; and Souza and Allen, 2009):

$$\Delta\sigma_{ij}^{\mu+1} = C_{ijkl}^{\mu+1}\Delta\varepsilon_{kl}^{\mu+1} + \Delta\sigma^{R}{}_{ij}^{\mu+1} \tag{3. 25}$$

$$C_{ijkl}^{\mu+1} = \frac{1}{V^{\mu}}\int_{V^{\mu}} \left\{ C'^{\mu}_{ijkl} + C'^{\mu}_{ijpq}\left[\frac{1}{2}\left(\lambda^{\mu}_{pkl,q} + \lambda^{\mu}_{qkl,p}\right)\right] \right. dV \tag{3. 26}$$

$$\Delta\sigma^{R}{}_{ij}^{\mu+1} = \frac{1}{V^{\mu}}\int_{V^{\mu}} \left(C'^{\mu}_{ijkl}\,\Delta\varepsilon^{\mu}_{kl} + \Delta\sigma^{R}{}^{\mu}_{ij} \right) dV \tag{3. 27}$$

where $C_{ijkl}^{\mu+1}$ is the homogenized instantaneous (tangent) constitutive tensor evaluated at the previous time step t, which is a time dependent quantity affected by the amount of damage accumulated at the local RVE, thus producing a nonlinear behavior at the global scale; C'^{μ}_{ijkl} is the local scale constitutive tensor; and $\Delta\sigma^{R}{}_{ij}^{\mu+1}$ is the so-called homogenized history-dependent stress term, which represents the rate-dependence in the material (both bulk and cohesive zones) behavior and is recursively computed at each time step.

3.4. Multiscale Algorithm

The two-way coupled multiscale model used in this research was implemented in a time-stepwise computational procedure developed by Souza (2009). The code, called

MULTIMECH (an acronym for MULTIscale MECHanics), was based on the finite element method and written using the C++ programming language.

To avoid initial compliance to the finite element mesh with the insertion of cohesive zone elements prior crack initiation and reduce the maximum bandwidth of the stiffness matrix, the computational model adopted herein uses an algorithm to automatically insert cohesive zone elements into the finite element mesh at the moment in time at which the criterion for cohesive zone initiation is satisfied, called *AICZ* (Automatic Insertion of Cohesive Zones). The Lagrange multipliers technique has been implemented to avoid interpenetration of objects, simulating frictionless contact conditions. Lagrange multipliers are also used to avoid interpenetration of cohesive zones, especially in problems where compressive stresses are highly noticeable.

Furthermore, the multiscale code used herein has been parallelized. Since the multiscale approach assumes that the local scale meshes are interdependent, they can be solved simultaneously by different processors. Thus, parallel programming can significantly increase the computational power available for the solution of multiscale problems. Details about *MULTIMECH* code implementation, *AICZ* and parallelization of the multiscale code used herein can be found in Souza (2009).

Basically, the code is operated with seven main steps: i) input data for global and local scales; ii) obtain homogenized constitutive tensor for the global scale; iii) obtain global scale solution; iv) apply global scale deformation to the local scale problem; v) obtain local scale solution; vi) homogenize local scale field variables; and vii) update homogenized results into the global scale problem. Figure 7 illustrates the steps involved during the multiscale procedure in a flow chart.

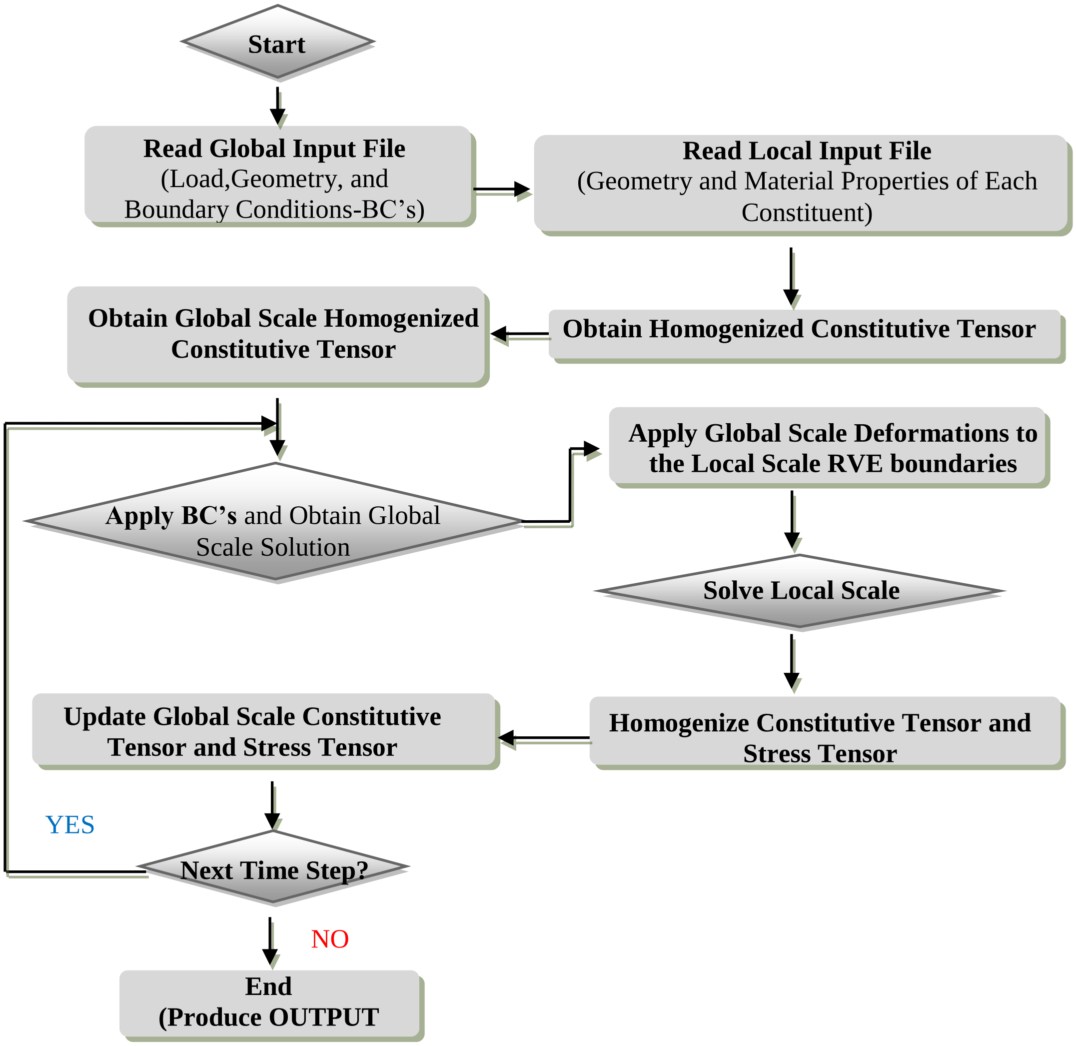

Figure 7: Flowchart of Multiscale Model Algorithm.

It is important to mention that the global scale solution is applied to the local scale problem by computing the strains at the integration points of each global element and sending this information to its respective local mesh. Thus, for each element of the global scale, a local analysis is performed using information from the upper scale. The two-way coupled global elements can be selected a priori without requiring the entire structure to be multiscaled. In this manner, the amount of computational time to solve the problem can be reduced; however, it may introduce some loss in accuracy.

3.5. Two-way coupled Multiscale Code Verification

To verify the two-way coupled multiscale model, a closed-form solution problem was solved. Thus, numerical results were compared to analytical solutions to determine the efficiency and accuracy of the model. Because one of the unique features of multiscale modeling is the capability of visualizing the component interactions at smaller scale lengths, a problem in which a non-homogeneous stress distribution could be observed was selected, which gave different local scale responses. Thus, a heterogeneous tapered bar problem as presented in Figure 8 was introduced.

The tapered bar problem was selected because of its inhomogeneous state of stress (as a result of its varying cross-section along the bar), which allowed the verification of different local scale behaviors. The tapered bar was assumed to be a composite of a viscoelastic matrix and elastic particles. Due to the axis of symmetry, only half of the bar was modeled, and monotonically increasing displacements were applied at the right end of the bar, as shown in Figure 8. The local scale RVE was represented by a unit cell determined by equating the volume fraction and the level of mesh refinement obtained from the global scale structure. Table 1 presents the material properties of the matrix and the particles. The properties used for this study are arbitrarily assumed for simulation purposes only.

Table 1: Material Properties used for the Model Verification

Elastic Properties (Inclusions)			
E	55.2GPa		
ν	0.15		
Viscoelastic Properties (Matrix)			
E_{inf}	7020kPa	ν	0.35
E_1	245649kPa	η_1	7.36945kPa.sec
E_2	422264kPa	η_2	126.680kPa.sec
E_3	399319kPa	η_3	1197.96kPa.sec
E_4	251828kPa	η_4	7554.83kPa.sec
E_5	69097kPa	η_5	20729.1kPa.sec
E_6	22586kPa	η_6	67757.4kPa.sec
E_7	7817kPa	η_7	234497kPa.sec
E_8	3460kPa	η_8	1037880kPa.sec
Fracture-Damage Parameters (Cohesive Zone)			
δ_n^*	50 mm		
δ_s^*	50 mm		
σ_n^f	1500 kPa		
σ_s^f	1500 kPa		
A	10		
M	0.5		

**Viscoelastic relaxation modulus is the same as that given for the bulk material*

The analytical solution for this problem is given by:

$$\varepsilon(x,t)=\frac{0.1t}{\ln(2)}\left(\frac{1}{20-x}\right) \tag{3. 28}$$

$$\sigma(x,t)=\frac{0.1}{\ln(2)}\left(\frac{1}{20-x}\right)\overline{E}(t) \tag{3. 29}$$

$$\overline{E}(t)=E_{\infty}^{c}t-\sum\left(\eta_{i}^{c}e^{-\frac{E_{i}^{c}}{\eta_{i}^{c}}t}\right)+\sum\eta_{i}^{c} \tag{3. 30}$$

where the Prony series terms ($E_{\infty}^{c}, E_{i}^{c}, \eta_{i}^{c}$) used to represent the composite material property, $\overline{E}(t)$, were obtained by simulating a relaxation test on the heterogeneous RVE.

The global and local scale objects were discretized, and the finite element meshes were constructed as shown in Figure 8. The finite element mesh (15,437 triangular elements) of the global scale object with particles (Figure 8 (a)) was finally developed by repeating a mesh refinement process until the finite element numerical solution without cracks converged and closed to an analytical solution. To validate the multiscale modeling technique, a set of homogeneous global scale meshes in a different level of mesh refinement (8 to 56 triangular elements as presented in Figure 8(b-d)) was simulated by linking the meshes with the local scale RVE (Figure 8 (e)).

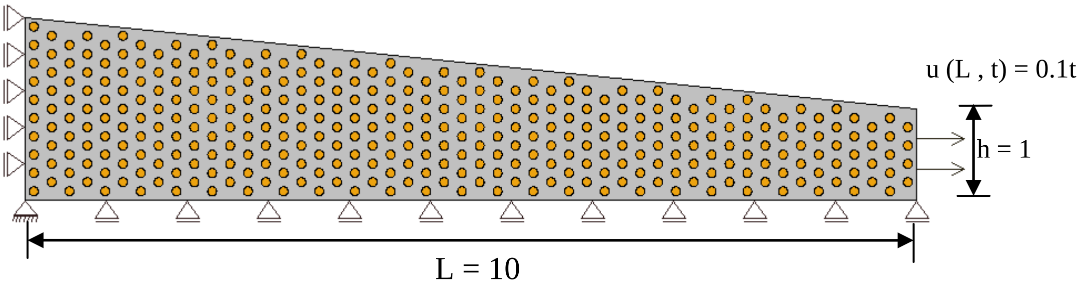

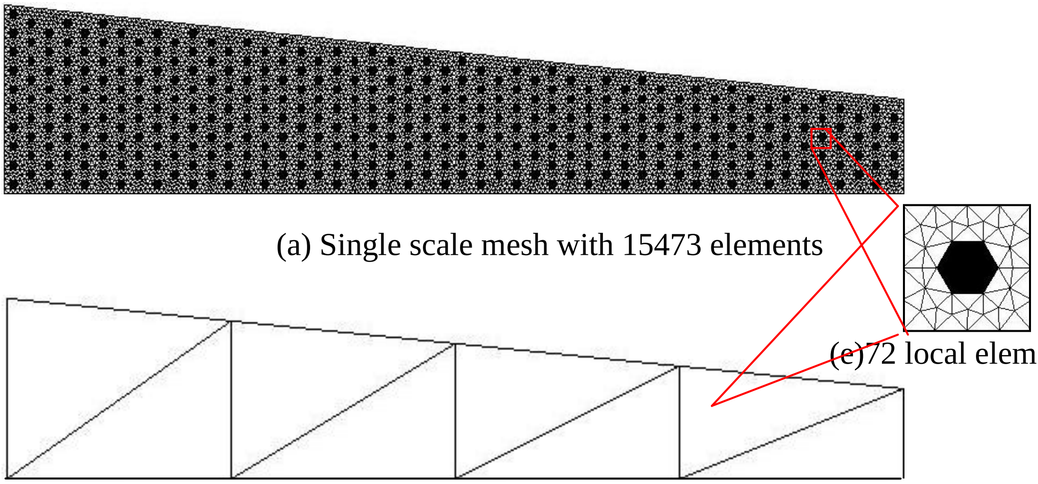

(a) Single scale mesh with 15473 elements

(e)72 local elements

(b) Global scale mesh with 8 elements

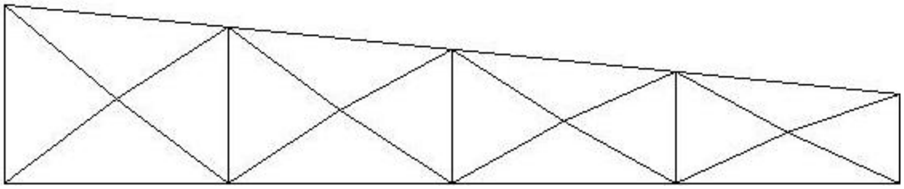

(c) Global scale mesh with 16 elements

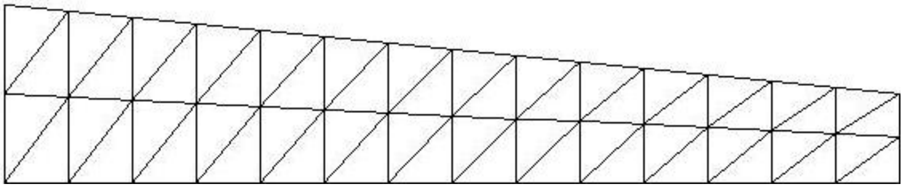

(d) Global scale mesh with 56 elements

Figure 8: Viscoelastic Tapered Bar Problem.

Simulation results from the multiscale model can be compared to the single scale simulation results and the analytic solutions. Figure 9 plots the reaction force of the tapered bar as loading time increased. Figure 10 and Figure 11 present the elemental stresses of the tapered bar for the multiscale and single scale cases without damage, respectively, considering the material heterogeneity.

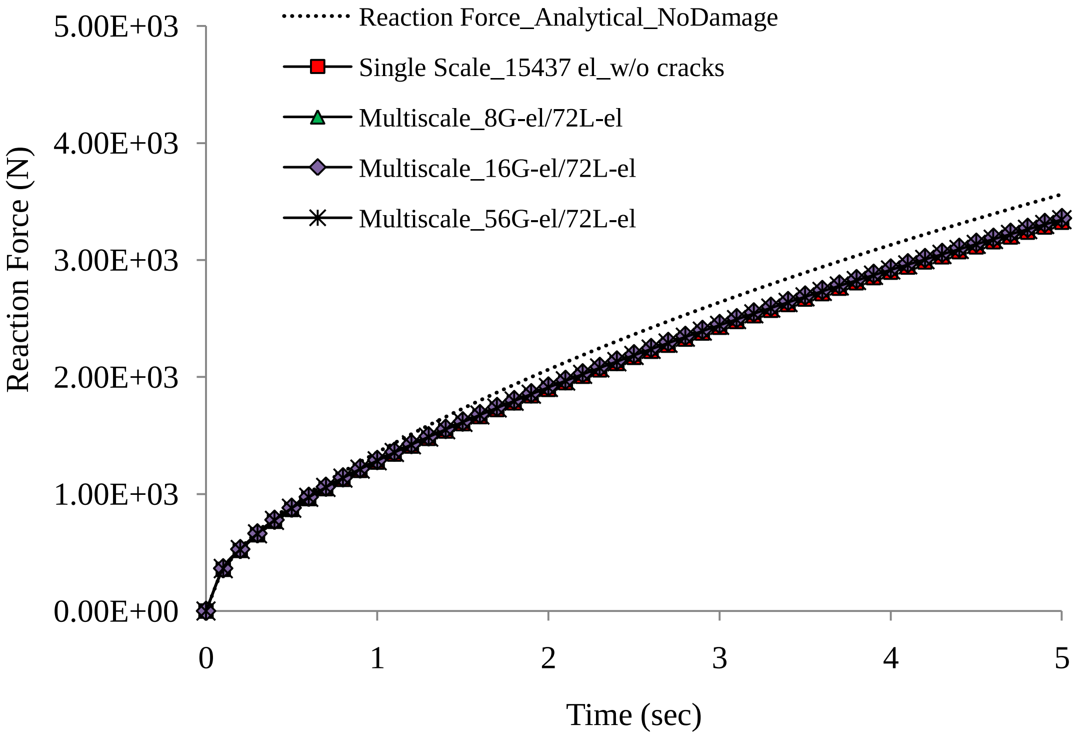

Figure 9: Tapered bar reaction force.

The figure shows that the numerical simulation results are very close to the analytical solution, with less than a 5.0% difference among their values. In fact, the multiscale results from the global scale mesh with only 8 elements are almost identical to the single scale result considering the material heterogeneity.

One thing to be noted from the simulations was the computational efficiency of the multiscale approach. The simulation time required to finish the single scale case (15,437 elements) was approximately 19 minutes, while the same level of accuracy could be obtained from the multiscale technique in only 37 seconds, i.e., the multiscale model solved the problem 31 times faster than the single scale model using an ordinary desktop computer with only one processor (2.50 GHz CPU, 4GB RAM memory, and Linux OS).

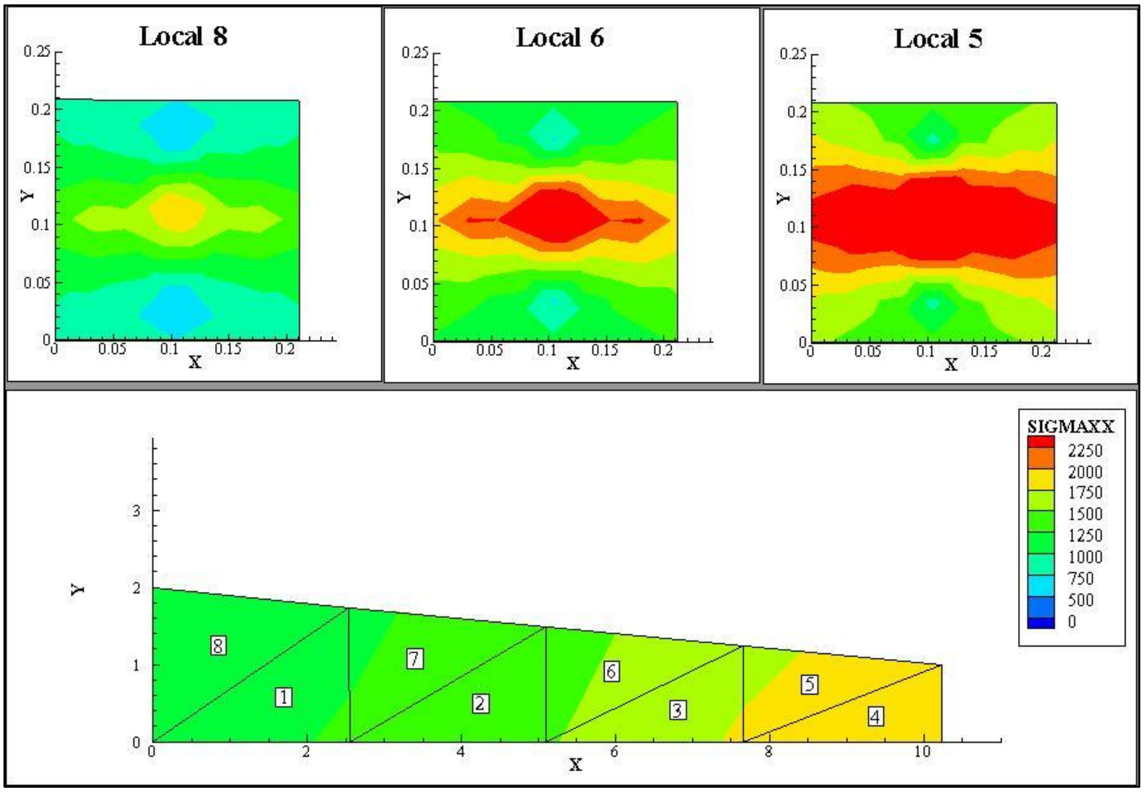

Figure 10: Longitudinal stresses contours for tapered bar multiscale simulation without damage (snapshot at 2.4 seconds).

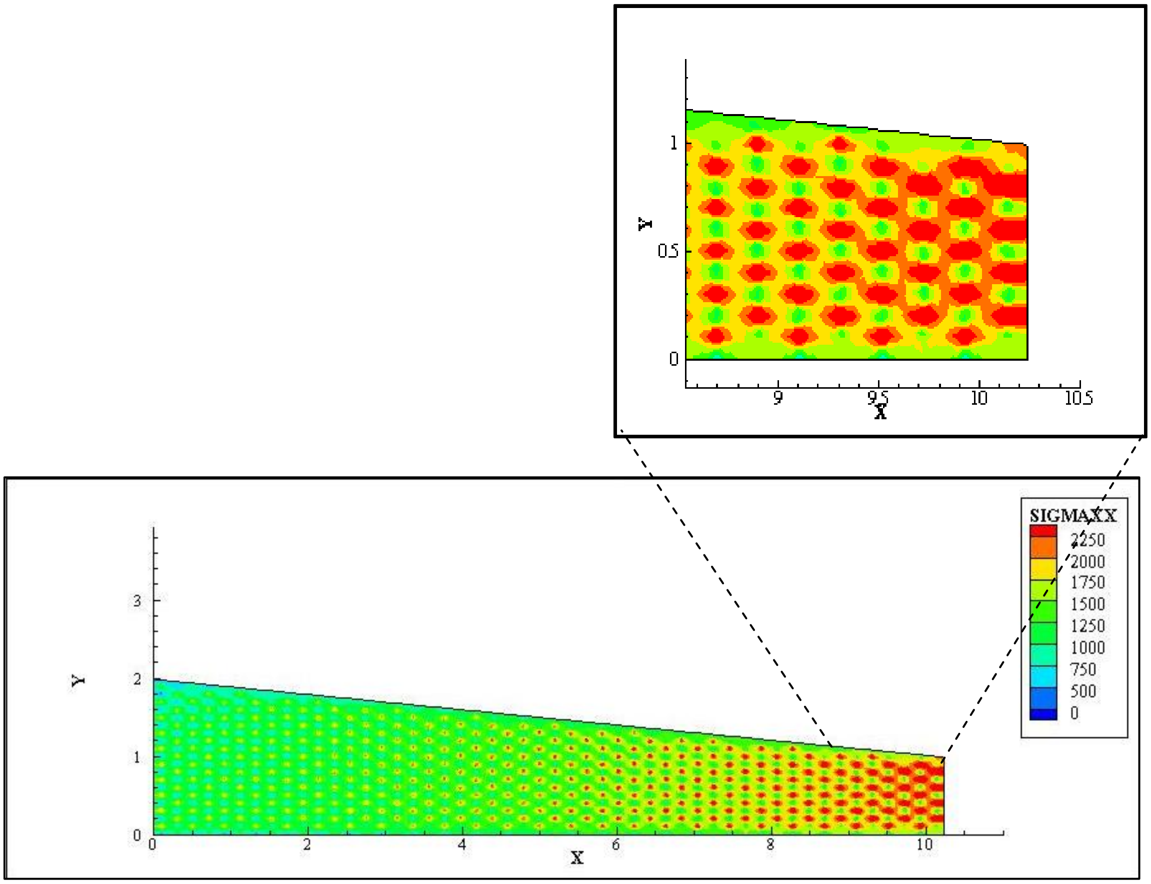

Figure 11: Longitudinal stresses contours for tapered bar single scale simulation without damage (snapshot at 2.4 seconds).

The effectiveness of the model for damage-induced problems was verified by simulating the tapered bar problem described above and comparing the single scale numerical results with the multiscale numerical results. However, different from the previous case, cohesive zone elements were allowed to be inserted into the mesh using the *AICZ* algorithm once the traction on the elements reached the cohesive zone critical traction, defined a priori as a damage parameter.

Before comparing the multiscale results with the single scale results, multiscale mesh convergence study for the tapered bar problem was performed, in which cracks were allowed to form and propagate in the local microstructure. This is necessary because in general more refined meshes are necessary for convergence of problems with damage evolution. First, the level of refinement in the local scale was kept constant (with 72 local elements), and the three global meshes (Figure 8) were used for simulations. Figure 12 plots the average longitudinal stress, σ_{11}, of the tapered bar as loading time increased.

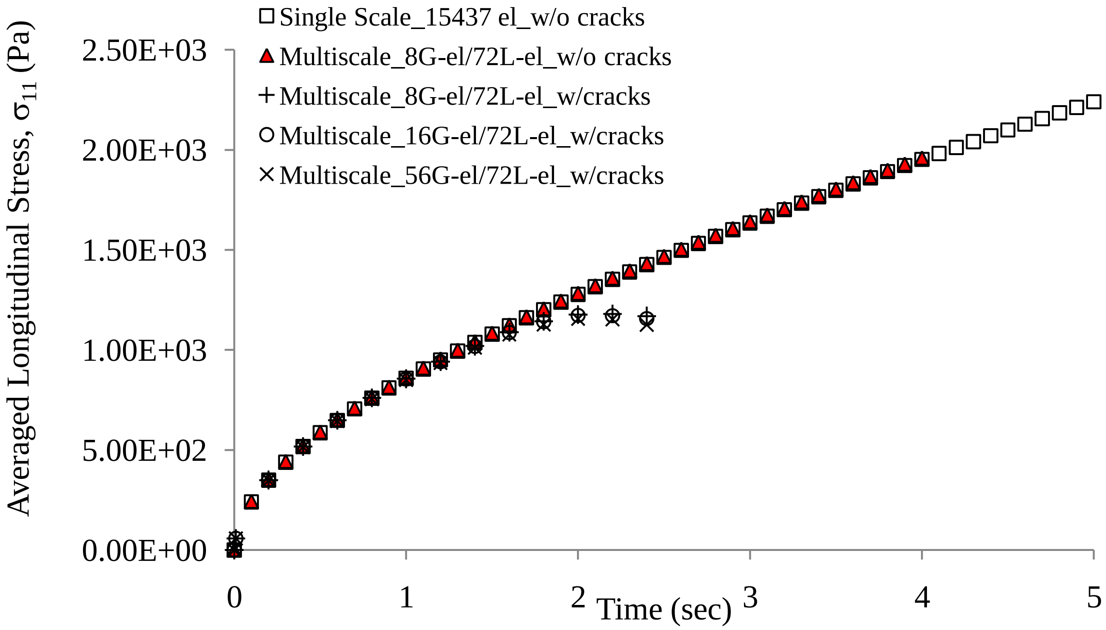

Figure 12: Global mesh convergence study for the tapered bar problem with cracks.

As can be noticed in Figure 12, the level of refinement seen in the global mesh did not affect the solution, which implied that 8 global elements were enough to obtain converged solutions for this problem. However, the level of refinement at the local scale needed to be verified. Thus, a local mesh convergence study was performed using 8 global elements, and the level of refinement in the local scale was varied by discretizing the local unit cell in 72, 190, and 624 local elements (Figure 13). Figure 14 shows the obtained results.

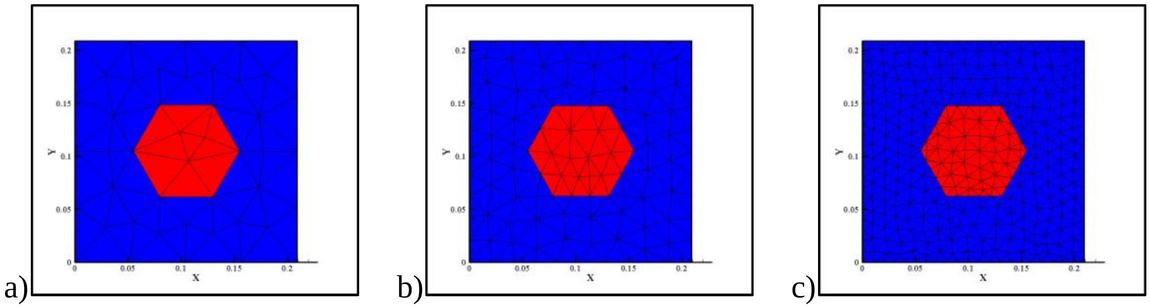

Figure 13: Local Meshes with: a) 72L-el, b)190L-el, and c) 624L-el.

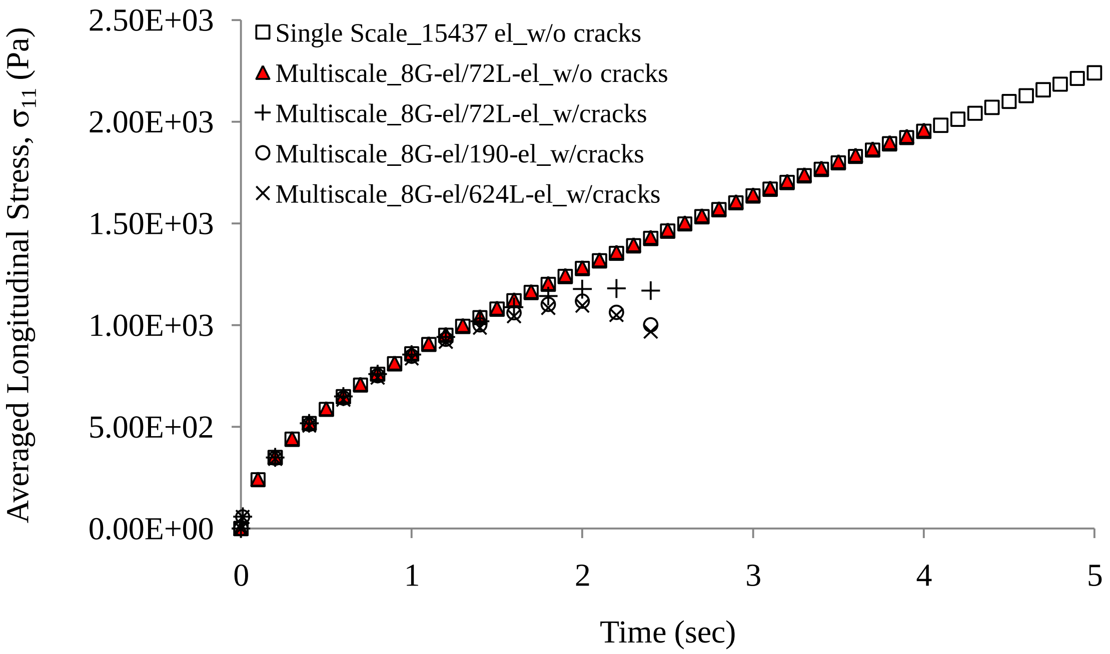

Figure 14: Local mesh convergence study for the tapered bar problem with cracks.

From Figure 14, it can be noticed that, due to the formation of cracks, the average stress σ_{11} deviated from the non-damage numerical solution curve after a certain point. Furthermore, it can be observed that the level of refinement in the local scale had a significant impact on the results. The convergence was reached using 8 global elements and 190 local elements.

To complete the multiscale analysis, a simulation using the converged global (8 elements) and local scale (190 elements) meshes and a smaller time step was performed to guarantee that the time step used in the simulations (Δt=0.01s) was appropriate.

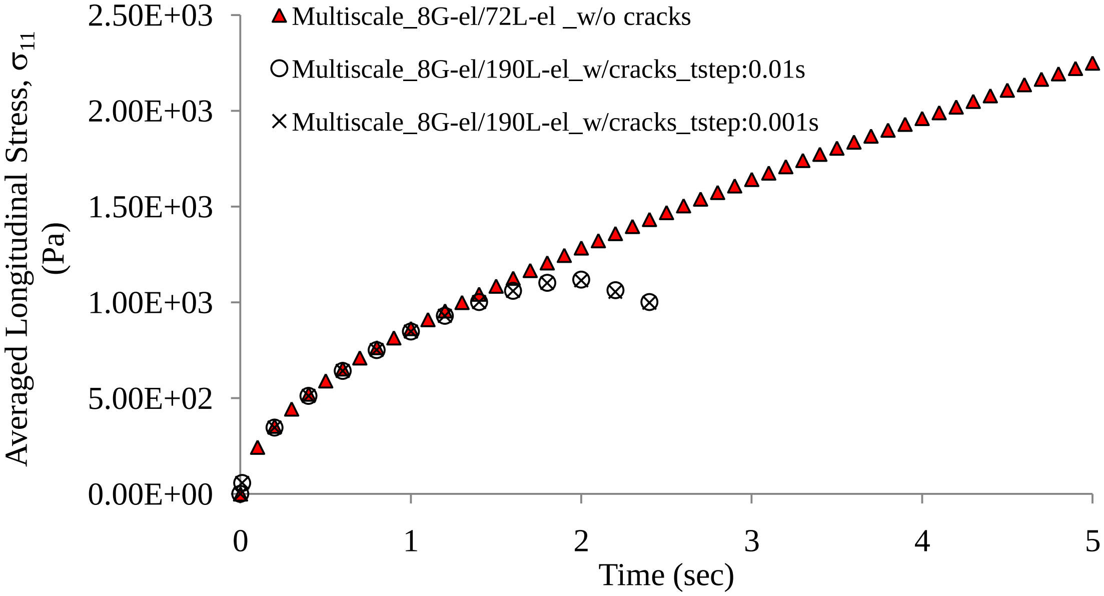

Figure 15: Time step convergence study for the tapered bar problem with cracks.

From Figure 15, it can be noticed that the time step used in the simulations was small enough to obtain converged solutions. Thus, the convergence of the multiscale solution when damage induced by cracks was added to the problem was achieved using a global mesh with 8 elements linked to a local scale unit cell with 190 local elements, using a 0.01 s time increment.

Now, to verify the efficiency of the model compared to the ones where all heterogeneities are discretized in a single scale, the converged multiscale solution was compared to the converged single scale solution. The converged single scale solution for the tapered bar problem with damage induced by cracks was obtained by repeating a mesh refinement process until a converged finite element numerical solution was obtained.

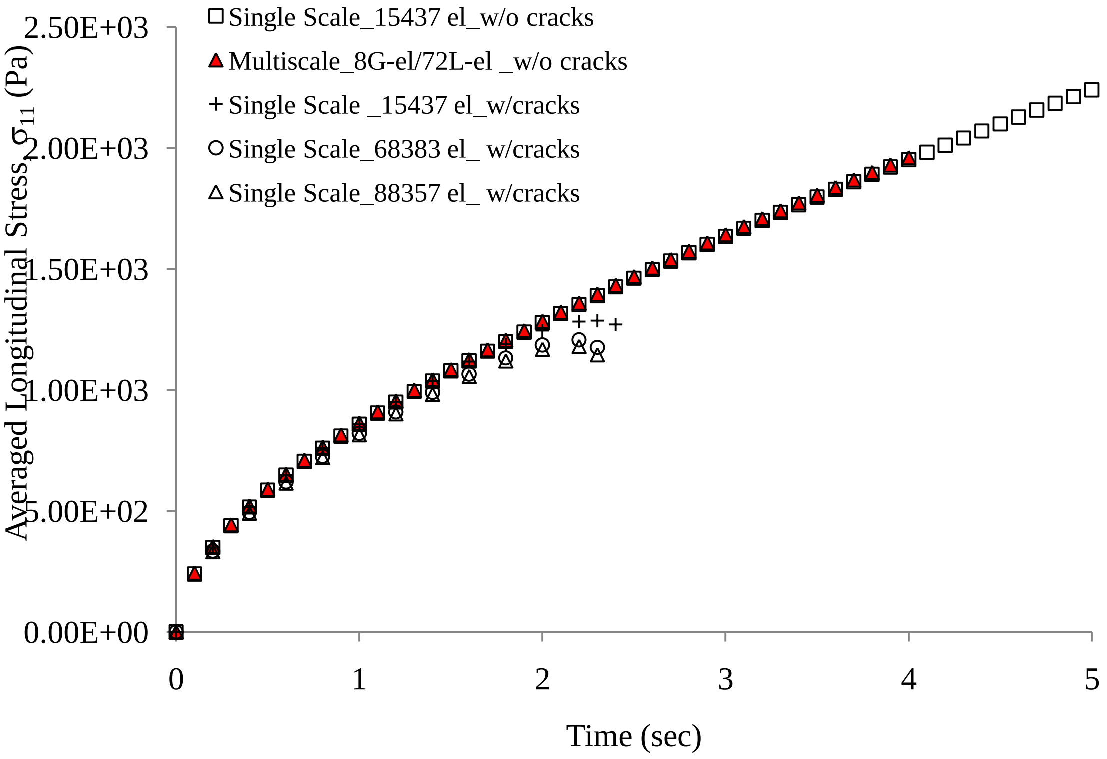

Figure 16: Single Scale mesh convergence analysis.

As illustrated in Figure 16, the single scale converged solution was obtained using 68383 finite elements. Once more, a higher level of refinement is required to solve problems when damage is induced by cracks. Finally, to verify the effectiveness of the two-way coupled multiscale model in predicting the damage-dependent behavior of composites, the converged multiscale and single scale solutions were compared. Figure 17 shows the numerical results obtained with both modeling schemes.

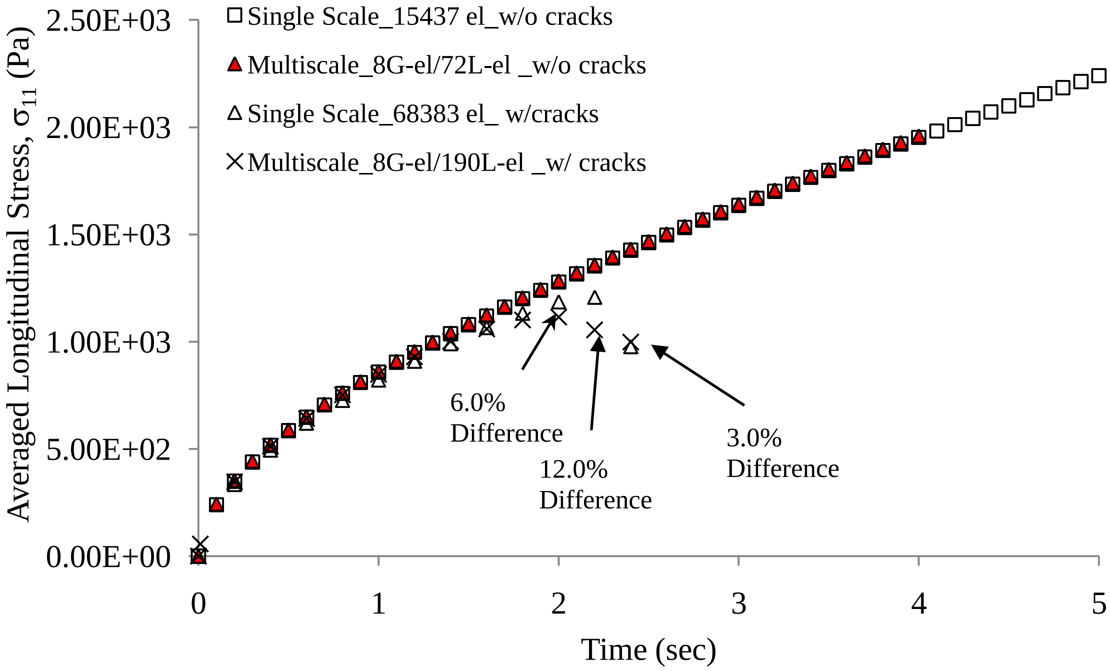

Figure 17: Multiscale code verification when damage in the form of cracks is induced to the problem.

Compared to the single scale solution (using a finite element mesh with 68383 elements), the multiscale numerical solution obtained with a mesh containing only 8 global elements and 190 local elements was considered satisfactory, where a good match between their results were obtained until the peak point (around 2 seconds). After that point, when a considerable amount of damage was induced by cracks, a macrocrack developed at the right-hand side of the bar in the single scale solution, resulting in a rapid drop of the longitudinal stresses. In the multiscale solution, on the other hand, since the damage was homogenized, a more gradual loss of strength was obtained. Figure 18 and Figure 19 present the deformed mesh and elemental longitudinal stresses of the tapered bar at the end of the simulation (2.4 seconds) for the multiscale and the reference single scale cases, respectively.

In terms of the computational time required to run this problem, the multiscale solution including cracks was obtained 4881 times faster than the single scale solution using a Dell workstation with 8 Intel Xeon processors at 3.00 GHz running under Linux Fedora 10. Clearly, this example demonstrates the higher computational efficiency of the multiscale technique when the object is highly heterogeneous. Table 2 shows a comparison regarding the computational time required to solve the tapered bar problem using single scale and multiscale models. Furthermore, the increasing on the model efficiency when the problem is solved in multiple processors (parallel programming) was analyzed.

Table 2: Computational time required for single and multiscale numerical converged solutions.

	Model	Number of elements	Number of Processors	Number of solution steps	Computational time, T (min.)	T_{SS}/T_{MS}
w/o cracks	SS	15437	1	1000	19	-
	MS	8-global/ 72-local	1	1000	0.62	31
w/ cracks	SS	68383	1	240	895	-
	MS	8 global/ 190 local	1	240	0.62	1451
			2	240	0.37	2440
			4	240	0.22	4130
			8	240	0.18	4881

*SS - Single Scale Model; MS-Multiscale Model

As illustrated in Table 2, the multiscale approach greatly reduces the computational time to solve the problem compared to the solution using a microstructure with discrete fracture modeling technique. Moreover, since the local scale meshes are not interdependent at each time step, the use of parallel computing increases the multiscale model efficiency by allowing the solution of different local meshes simultaneously by different processors, which significantly reduces the computational time. This benefit will be more noticeable in the modeling of composite materials that show a significant level of geometric complexity and material inelasticity.

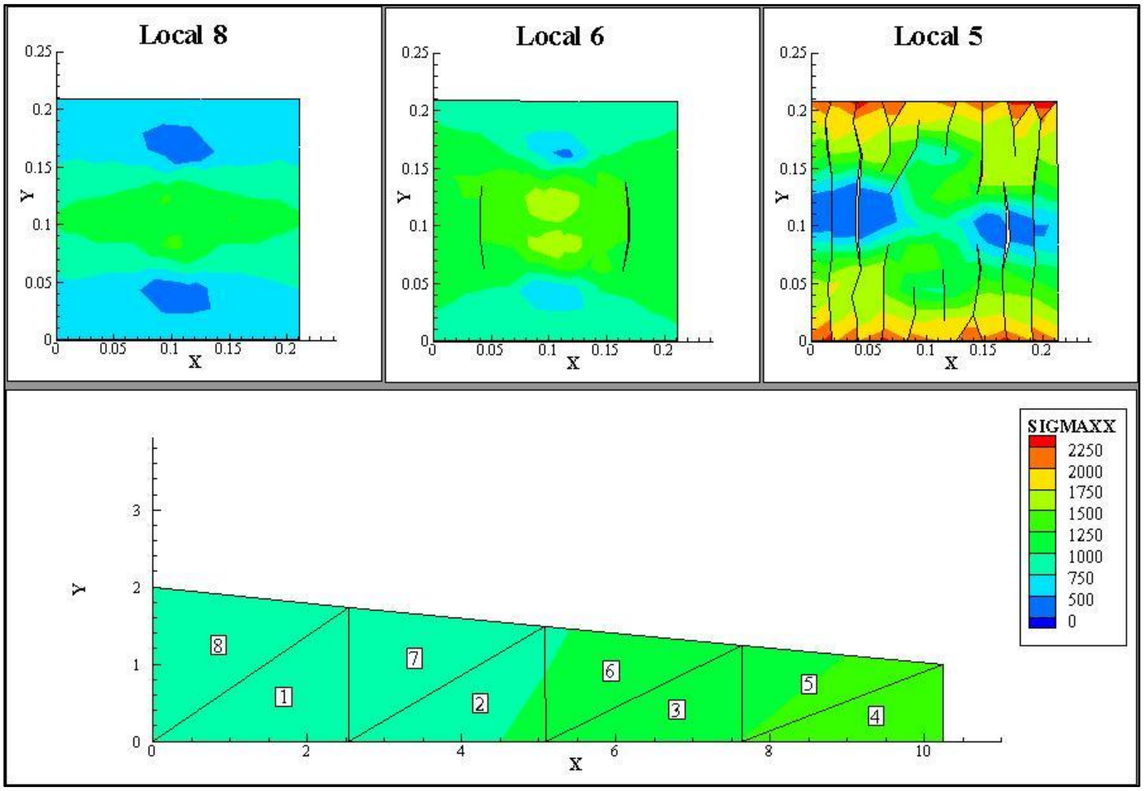

Figure 18: Longitudinal stresses contours for tapered bar multiscale simulation with damage (snapshot at 2.4 seconds).

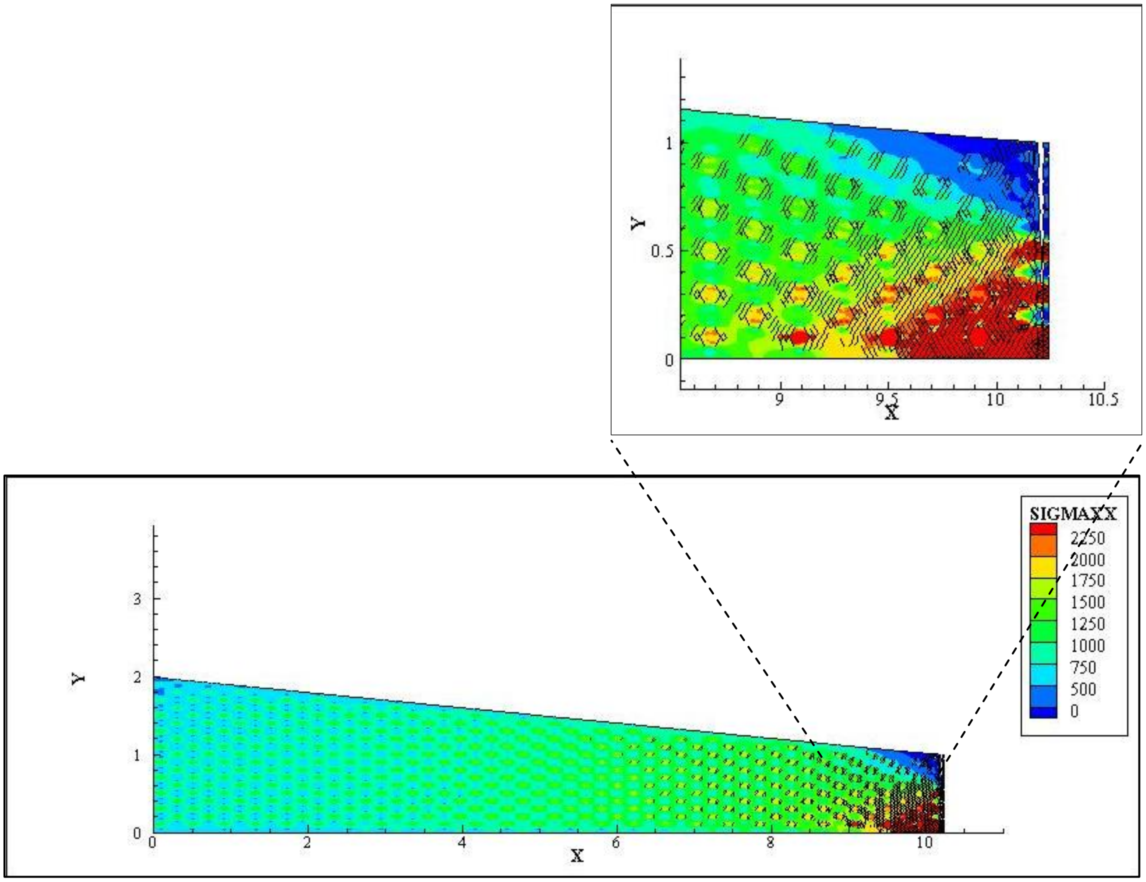

Figure 19: Longitudinal stresses contours for tapered bar single scale simulation with damage (snapshot at 2.4 seconds).

The bar obviously experienced higher stresses in regions of smaller cross-sections, and particles were under higher stresses than the matrix phase, as shown in the single scale simulation (Figure 19). The homogenized stresses obtained from the multiscaling seemed to be equivalent to the stress state of the single scale case, in which two phases (i.e., particle and matrix) clearly presented different levels of stresses.

Chapter 4

Laboratory Tests and Results

This Chapter presents the materials and procedures employed in the fabrication of bituminous composite sample, as well as the three-point bending testing conditions and the obtained experimental results. Furthermore, the required tests to obtain local scale material properties and outcomes from those tests are presented. To the end, all experimentally obtained material properties required for the numerical simulations are determined.

4.1. Bituminous Composite Mix Design

The most widely used local paving materials (aggregates and asphalt binder) were selected for fabricating laboratory samples. Because the addition of hydrated lime has been recommended for the mixtures produced in Nebraska to reduce moisture effects, it was incorporated into the mix design in this study.

Three local aggregates (two crushed gravels (such as 3ACR and 47B) and screenings) were used in the composition of the studied bituminous mixture. Figure 20 presents a gradation of aggregate blends used to produce the asphalt mixture. In addition to the bituminous mixture specimen, samples using only aggregate particles less than 0.60 mm (asphalt matrix) were fabricated to be used for small scale tests to determined component properties, as will be described in the latter sections of this chapter. The asphalt matrix gradation was calculated kept with same proportion of aggregates as they had in the blend of the bituminous mixture sample.

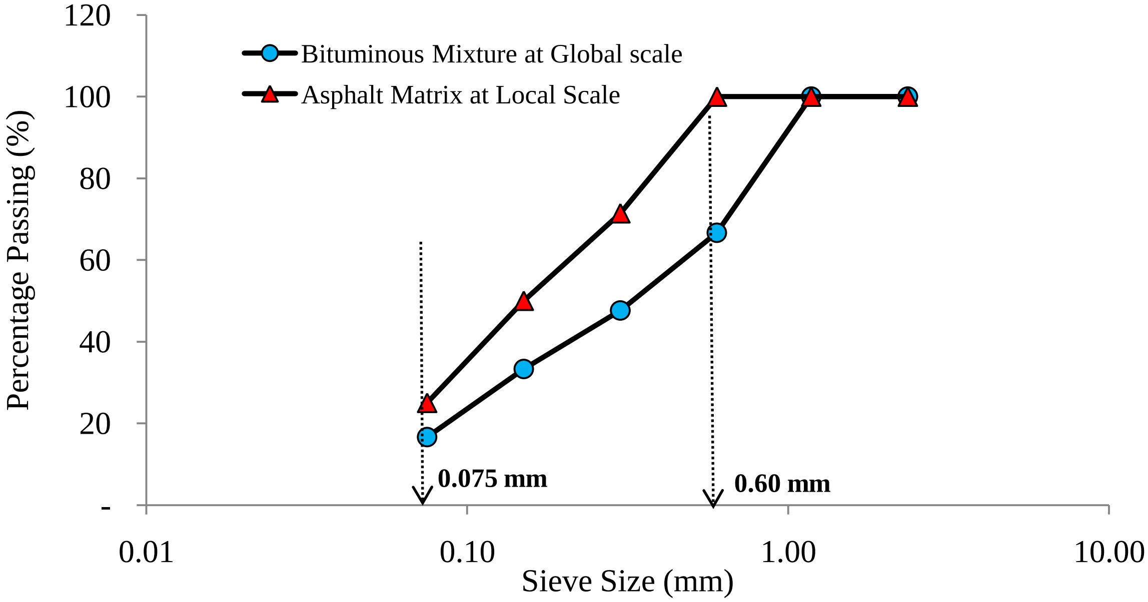

Figure 20: Gradation curves of the fine aggregate matrix and the global structure bituminous composite.

The bituminous mixture was produced by mixing aggregate particles combined with 10.30% of asphalt binder PG 68-24 and 1.5% of hydrated lime (the percentages are based on the total weight of the bituminous composite mixture). The mixture was compacted using a Superpave gyratory compactor to produce cylindrical samples that were 150 mm in diameter and 170 mm in height (Figure 21).

Cylindrical matrix samples were fabricated using aggregates smaller than 0.60 mm combined with 13.3% by the weight of the mixture of asphalt binder and 1.5% of hydrated lime. The amount of binder used for the matrix phase was calculated by taking the total amount of binder used for the bituminous composite and subtracting two quantities: i) the amount of effective binder that is used to cover the aggregate particles bigger than 0.60 mm, and ii) the amount of binder that is absorbed by the aggregate particles bigger than 0.60 mm. The percentage of asphalt binder material remained was, then, used to calculate the amount of binder in the matrix mixture.

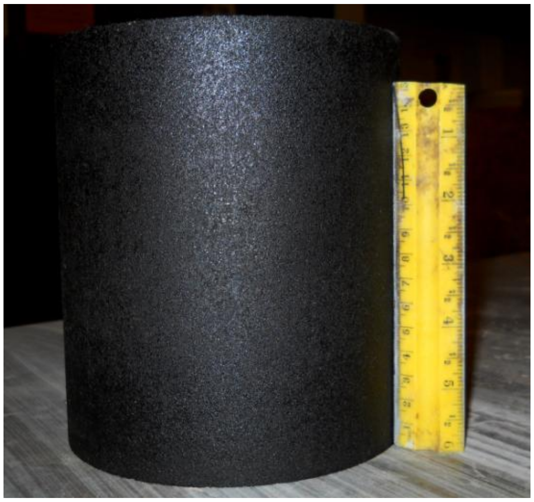

Figure 21: Superpave Gyratory compacted cylindrical specimen.

4.2. 3-Point Bending Beam Test Specimen Geometry

Several scientific papers (Wagoner *et. al*., 2005; Kim *et al*., 2009; Marasteanu *et al*., 2002; and others) selected the single-edge notched rectangular beams to study pure mode I fracture behavior of asphaltic composites. The authors chose the rectangular beam test because its configuration was rather simple and they could have the flexibility to investigate other areas such as the mix-mode fracture (offsetting the mechanical notch from the rectangular beam centerline) and the sample size effect (by changing the sample width, height and/or thickness).

Considering the reasons above mentioned, this study adopted the rectangular beam geometry. However, the specimens used herein were produced without a mechanical notch to induce some mode mixity. Mixed-mode fracture is important for the analysis of bituminous composites behavior since flexible pavements are subjected to a combination of thermal loading (tension) and wheel loading (tension and shear) (Wagoner *et. al*., 2005).

Most of the aforementioned studies used beam compactors to obtain laboratory fabricated rectangular beam specimens. Since it was not possible to compact beam specimens at the University of Nebraska (UNL) asphalt laboratory, the beam samples were extracted from gyratory compacted cylindrical samples. After a coring and cutting process, a 150-mm wide beam sample with 40-mm height and 25-mmm thickness could be obtained. Figure 22 illustrates the coring and cutting procedure used.

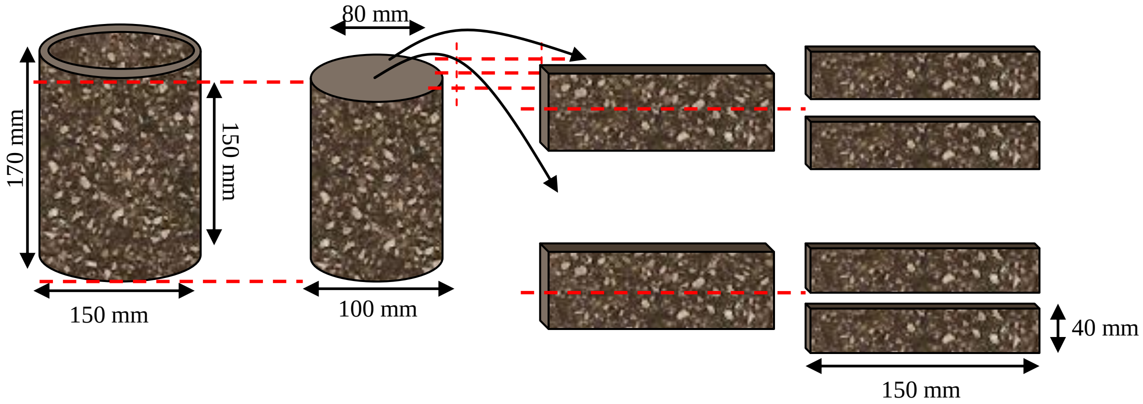

Figure 22: Illustration of beam specimen coring and cutting procedure.

4.3. 3-Point Bending Beam Test Experimental Setup and Results

The rectangular beam specimens obtained after the cutting and coring procedure were subjected to bending tests. The samples were placed inside a three-point bend fixture and loaded by a UTM 25 kN machine at a constant displacement rate (0.83mm/s) until the specimens failed completely. Figure 23 shows the experimental setup for a rectangular beam specimen.

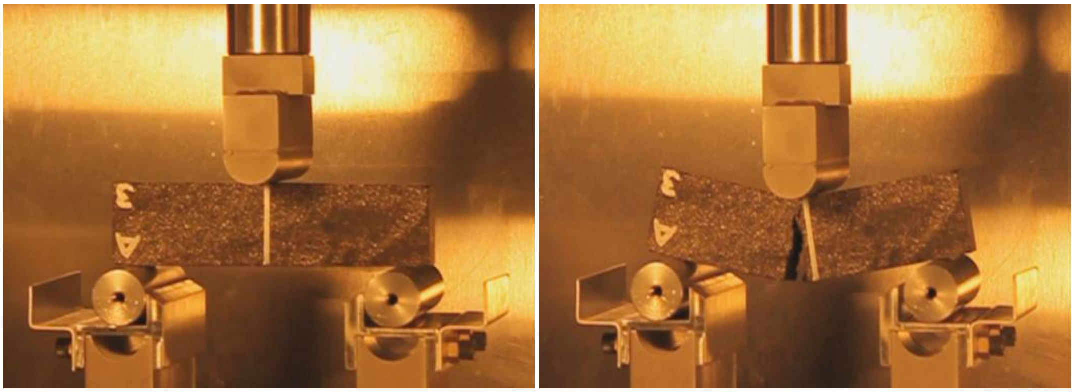

Figure 23: Experimental setup for three-point bending beam test before and after test

Three replicates were tested at 21 °C. The results were compared with numerical simulations to validate against the two-way coupled multiscale model. Figure 24 presents the experimental results obtained. A specimen (after being tested) with a macrocrack that developed at the center region is shown in Figure 25.

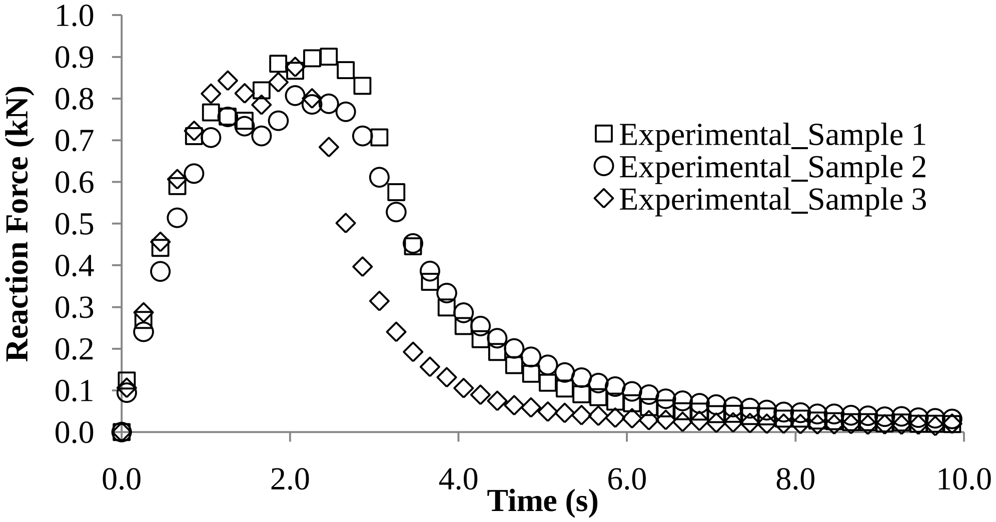

Figure 24: Experimental results from the rectangular beam bending tests.

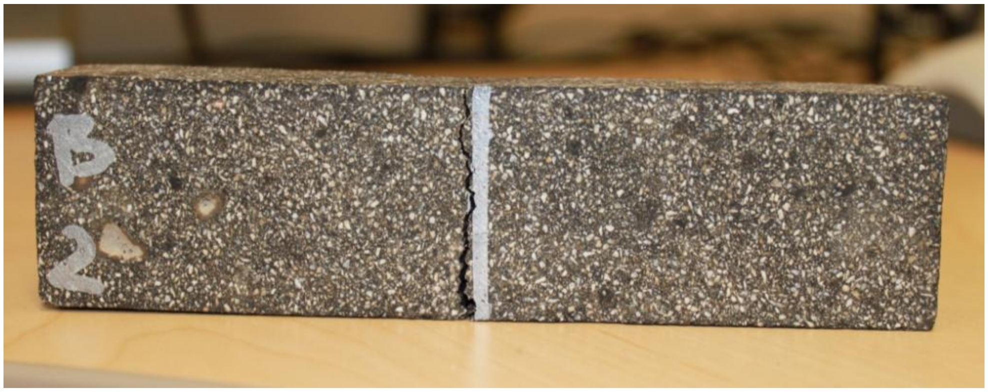

Figure 25: Beam specimen after test.

4.4. Local Scale Experimental Setup and Results

For the multiscale model simulations, a local scale heterogeneous mixture (RVE) and its mixture constituent properties need to be identified to be linked to the global scale mixture performance.

The RVE structure was determined using an image analysis technique coupled with numerical simulations, as will be discussed in the next chapter. Actual images from the bituminous composite inner structure were used for this determination. The following approach was used to acquire the images:

- First, gyratory compacted samples (150 mm in diameter and 175 mm in height) were produced and cut vertically using a diamond saw;
- Then, the vertical section was placed on a high resolution scanner from which the image was captured by the computer;

- The virgin inner structure image was then processed with sequential image analysis stages, and the final image, which only captured the center portion (100 mm by 100 mm) of the specimen, was obtained (Figure 26)

Figure 26 shows a 100 mm by 100 mm microstructure digitized to 400 by 400 quadrilateral pixels (total 160,000 pixels). This procedure resulted in a 0.25mm/pixel grid, which cannot capture aggregates finer than approximately 0.25 mm (i.e., the majority of the aggregates that pass through a No. 50 sieve, which has a 0.30 mm opening size) and air voids. This image was used for the image analysis to determine the trial RVE values.

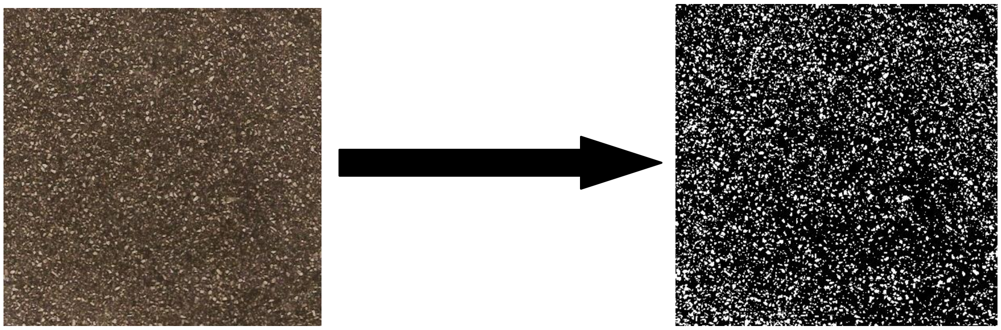

(a) virgin scanned image (b) adjusted binary image (black/white)

Figure 26: Image processing of bituminous composite microstructure.

Other steps were added in the image acquisition process to convert it into a finite element mesh. First, the aggregate boundaries needed to be identified to convert them into polylines. For that, an image treatment was required which eliminated particles less than 0.60 mm. After that, the image file was converted to a text file, which was imported to the mesh generator software used herein (*MTOOL*, 1997). In *MTOOL*, material phases were identified and, finally, a finite element mesh was generated.

Thus, for the numerical simulations, the portion of the aggregate gradation finer than 0.60 mm (eliminated during the image re-treating process) was considered in the matrix phase (asphalt matrix) in which linear-viscoelastic properties were experimentally obtained. In addition, aggregate particles larger than 0.60 mm were discretized in the local scale mesh with their linear-elastic properties experimentally determined. Furthermore, non-linear viscoelastic cohesive zones were inserted in the local mesh within the matrix phase using the *AICZ* algorithm.

A constitutive model was assumed for each phase depending on their behavior. The material parameters required as input for each material model were determined based on experimental analysis. A set of testing methods were designed and performed as follows:

- Nano-indentation tests were used to obtain the Young’s modulus of elastic aggregate particles;
- Dynamic frequency-sweep tests were used to obtain the viscoelastic properties of the asphalt matrix;
- Semi-circular bending tests were used to obtain the cohesive zone fracture properties.

In the following sections, the experimental procedures used to obtain the material properties are described.

4.4.1. Linear-Elastic Properties of Aggregate Particles

As mentioned in Chapter 3, the linear-elastic constitutive relationship, Equation (3.14), was used to model the aggregate particles.

Linear-elastic Young's modulus of aggregate particles is within the range of 10 - 80 GPa depending on the source of aggregate. However, the diverse values within this range can result in different composite responses. Aragao *et al.* (2010) performed a parametric analysis using three distinct aggregate moduli (20 GPa, 50.8 GPa, and 60.9 GPa) to compare with the dynamic modulus obtained experimentally and numerically. The third value, 60.9 GPa, was obtained after performing a series of nano-indentation tests in thin slices of asphalt concrete. The authors concluded that, depending on the aggregate modulus used, the dynamic modulus varied significantly. Laboratory and numerical results were better matched when the laboratory-obtained aggregate modulus was used in the simulations. Thus, to determine the Young's modulus for the specific aggregate used in this study, quasi-static nano-indentation tests were performed.

To perform the nano-indentation test, a hard indenter of known geometry and properties was used. The indenter geometry depended on the type of material being tested. As shown in Figure 27, a triangular indenter profile was chosen because aggregate particles have negligible creep. The indenter was pushed into the material surface in which elastic properties were to be determined at a nano-scale depth. Based on the load-unload curves obtained from the experiment, values of aggregate modulus were determined (Karki, 2010).

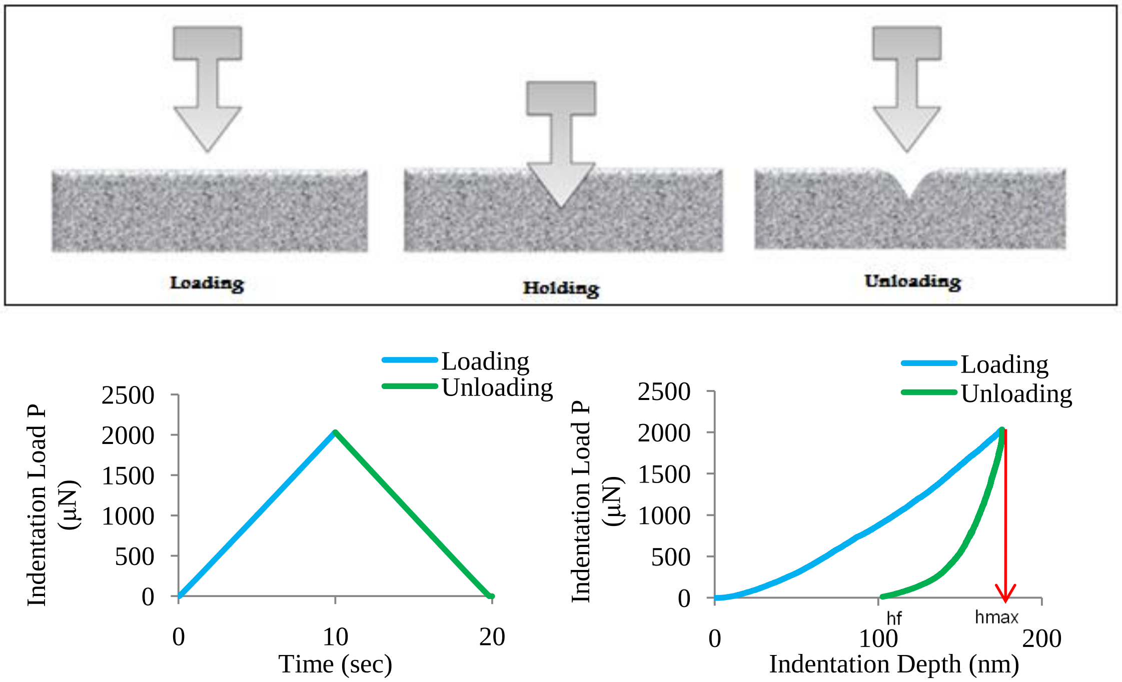

Figure 27: Visualization of loading profile and output curves (source: Karki, 2010).

Karki (2010) performed a series of nano-indentation tests for the mostly used aggregates by the UNL research team. Based on testing results, the author determined an average aggregate Young’s modulus of 60.9 ± 11.2 GPa (Figure 28), assuming a Poisson’s ratio of 0.15 obtained from literature (Barksdale, 1993).

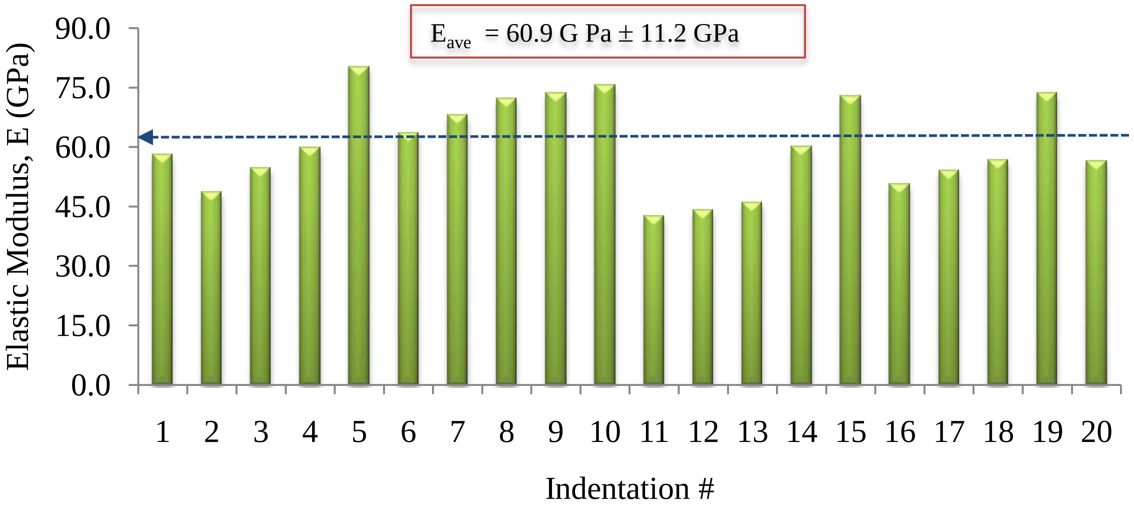

Figure 28: Elastic Modulus of aggregates in the asphalt mixture (source: Karki, 2010).

For this study, the same aggregate source was used as was used by Aragao *et al.* (2010) and described in Karki (2010). Thus, the experimentally determined Young's modulus of 60.9 GPa and the assumed Poisson's ratio of 0.15 were used in the numerical simulations performed herein.

4.4.2. Linear-Viscoelastic Properties of Matrix

Aside from the aggregates, the RVE also consisted of an asphalt matrix (asphalt binder plus aggregate particles smaller than 0.60 mm that could pass through a No. 30 sieve). The matrix phase can often be represented by a linear-viscoelastic (LVE) convolution integral, as described in Equation (3.15). Thus, the viscoelastic properties of the matrix were required to complete the model.

The viscoelastic properties of the matrix were experimentally obtained by performing dynamic frequency sweep tests. The matrix samples were then subjected to dynamic frequency sweep tests. That is, a low torsional strain of 0.0065% (the level of strain within the linear viscoelastic range) was applied to the specimens by sweeping the oscillatory frequency from 25 Hz to 0.01 Hz at three different temperatures (5 °C, 20 °C and 40 °C). In addition, the viscoelastic time-temperature superposition principle was used to obtain the master curve at a reference temperature of 21 °C (Figure 29).

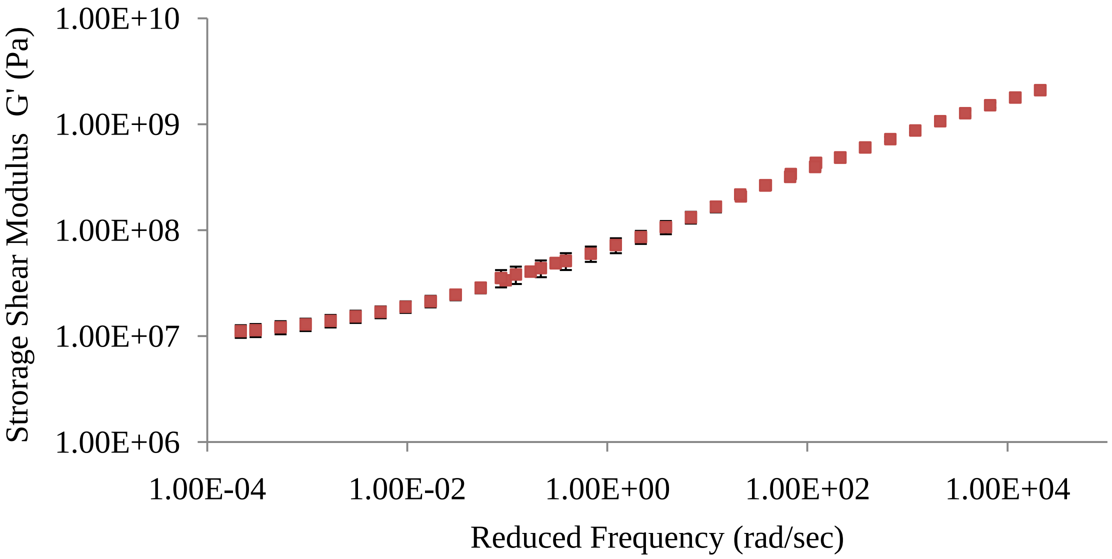

Figure 29: Master curve of Dynamic shear modulus for the asphalt matrix at 21°C.

The master curve was fitted by the following Prony series mathematical representation (Equation 4.1), which is frequently used to represent the linear-viscoelastic response in the constitutive equations because they precisely fit the experimental data (Christensen, 1982):

$$G^{'}(\omega) = G_{\infty} + \sum_{i=1}^{n} \frac{\omega^2 \tau_i^2}{\omega^2 \tau_i^2 + 1} G_i \qquad (4.\ 1)$$

where, G_{∞}, G_i, and τ_i are defined as Prony series coefficients.

Assuming a Poisson's ratio of 0.35 for linear-viscoelastic materials, which is also considered time-independent, the frequency domain master curve was converted to the time domain relaxation modulus (Equations 4.2 and 4.3), because the linear-viscoelastic constitution [Equation (3.15)] is represented as a function of the time domain stress relaxation modulus.

$$E(t) = 2G(t)(1+\nu) \qquad (4.\ 2)$$

$$E(t) = E_{\infty} + \sum_{i=1}^{n} E_i e^{-\frac{t}{\tau_i}} \qquad (4.\ 3)$$

where ν is the linear-viscoelastic Poisson's ratio, and the coefficients E_{∞} and E_i represent the relaxation modulus Prony series terms.

Table 3 shows the Prony series coefficients obtained after the fitting process and used for the numerical simulations of the asphalt matrix.

Table 3: Asphalt matrix linear-viscoelastic properties

Linear-Viscoelastic Properties (Asphalt Matrix)			
E_{inf}	1.22E+07 Pa		
ν	0.35		
E_1	3.03E+09 Pa	ρ_1	8.00E-05
E_2	1.48E+09 Pa	ρ_2	8.00E-04
E_3	1.33E+09 Pa	ρ_3	8.00E-03
E_4	4.35E+08 Pa	ρ_4	8.00E-02
E_5	1.60E+08 Pa	ρ_5	8.00E-01
E_6	5.00E+07 Pa	ρ_6	8.00E+00
E_7	1.79E+07 Pa	ρ_7	8.00E+01
E_8	3.02E+06 Pa	ρ_8	8.00E+02

4.4.3. Fracture Properties of the Cohesive Zone

The third material phase included in the composite constitution for the bituminous composite in this study was the cohesive zone. The cohesive zone is a damage zone in which cracks can potentially initiate and grow. There are many models in the literature that attempt to predict the damage evolution due to cracks, the corresponding material softening, and the eventual fracture failure of composite materials. The model selected in this study is based on the non-linear rate-dependent viscoelastic damage evolution law developed by Allen and Searcy (2001), mathematically represented by Equation (3.16). The model requires a set of fracture parameters that could not be easily obtained in the laboratory. Thus, a simple method was proposed herein to obtain those parameters. The method was divided in two steps: 1) a calibration process of a semi-circular bend fracture test to obtain mode I fracture parameters and 2) a comparison of the fracture energy obtained analytically for pure mode I and pure mode II conditions to obtain mode II fracture parameters.

The calibration process to obtain mode I fracture parameters consisted of two parts (Figure 30). First, SCB matrix samples (with only aggregate particles smaller than 0.60 mm) were subjected to pure mode I laboratory bending tests. Secondly, the pure mode I bending test was modeled using a single scale finite element model. The energy dissipation due to viscoelasticity was accounted by considering the SCB as a homogeneous linear-viscoelastic body with experimentally determined viscoelastic properties obtained for the matrix phase (Table 3). The energy dissipation due to the opening of cracks was added to the problem by using the cohesive zone model.

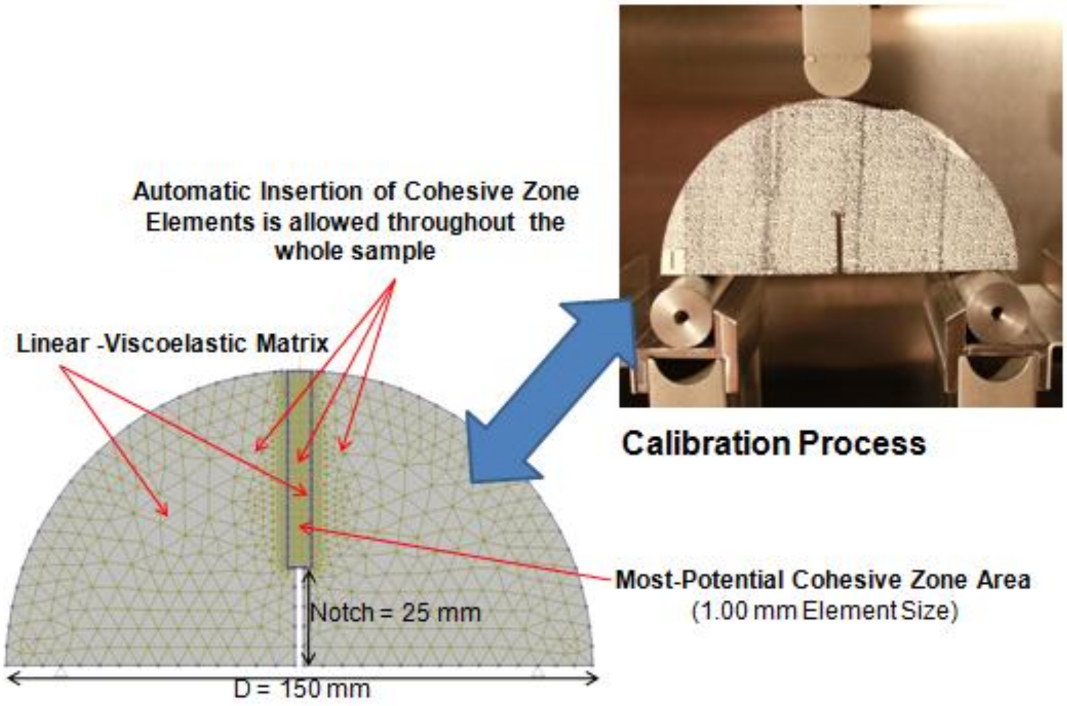

Figure 30: Calibration Process to determine mode I fracture parameters.

The semi-circular bend fracture test was originally performed to access the fracture behavior of rocks (Chong and Kuruppu, 1984). Recently, this testing procedure has been used to investigate the fracture mechanisms in bituminous materials (Aragão *et al.* 2010, Li and Marasteanu, 2010) due its simplicity. This procedure allows a large number of semi-circular bend (SCB) replicate samples to be obtained from one single cylindrical sample fabricated in a laboratory after coring and cutting, which reduces the time required for sample fabrication. In addition, the test can be easily performed by placing the sample on two bottom supports.

Thus, this testing configuration was adopted herein to calibrate the mode I fracture parameters required for the traction-displacement model of the cohesive zone. Figure 31 shows the SCB test set-up.

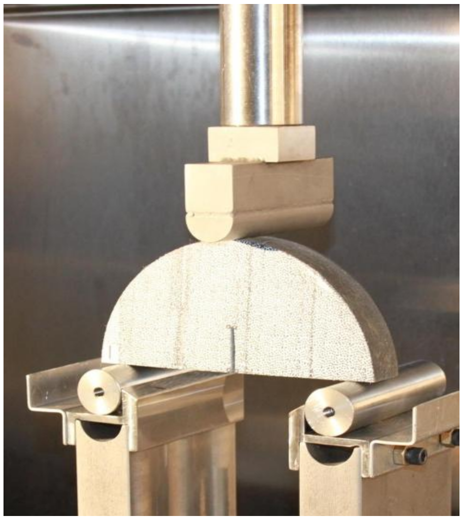

Figure 31: Semi-circular bend (SCB) test set-up.

As shown in the figure, the SCB specimen was a semi-circle with a radius of 75 mm containing a 25 mm long edge notch. This research used this test configuration to indirectly determine the fracture parameters associated with the normal opening of the cohesive zone (mode I) throughout the calibration process. The specimen was obtained using the following steps. 1) Superpave gyratory samples with a diameter of 150 mm and a height of 110 mm were compacted; 2) the samples were cut into 25 mm thick slices; 3) each slice was cut into two identical semicircles; and 4) a 25 mm notch was made using a 2 mm blade along the axis of symmetry. Figure 32 illustrates the overall sample fabrication procedure.

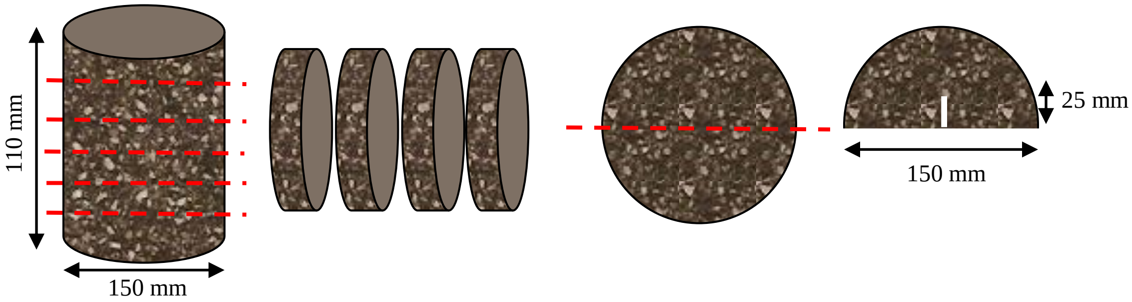

Figure 32: Illustration of SCB specimen coring and cutting procedure.

Two samples were tested and their results were compared with the numerical solution (Figure 33). The samples were placed inside a universal tester machine (UTM 25kN) and loaded up to failure at 0.83 mm/s at 21°C.

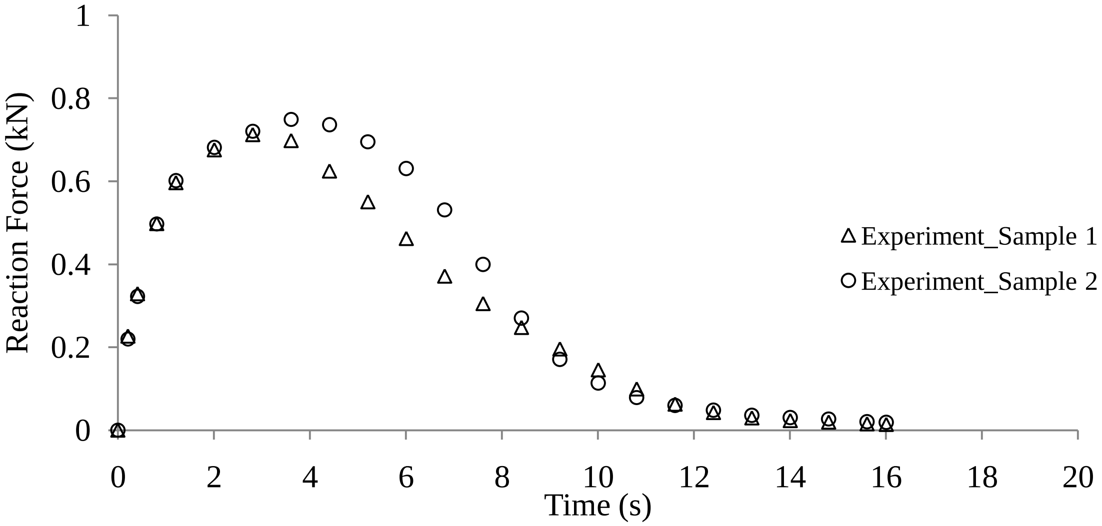

Figure 33: Laboratory results for SCB bending tests.

To determine the mode I cohesive zone fracture parameters, a trial-and-error calibration process was used by varying the parameters until a good match between the curves for the experimental and numerical reaction force versus time was obtained. Since the level of refinement plays an important role in numerical analysis, especially when damage is involved, two cases varying the element size in the center region were simulated.

Figure 34 shows the best match found after the calibration process was performed. Figure 35 presents the longitudinal stress contour at two selected loading stages.

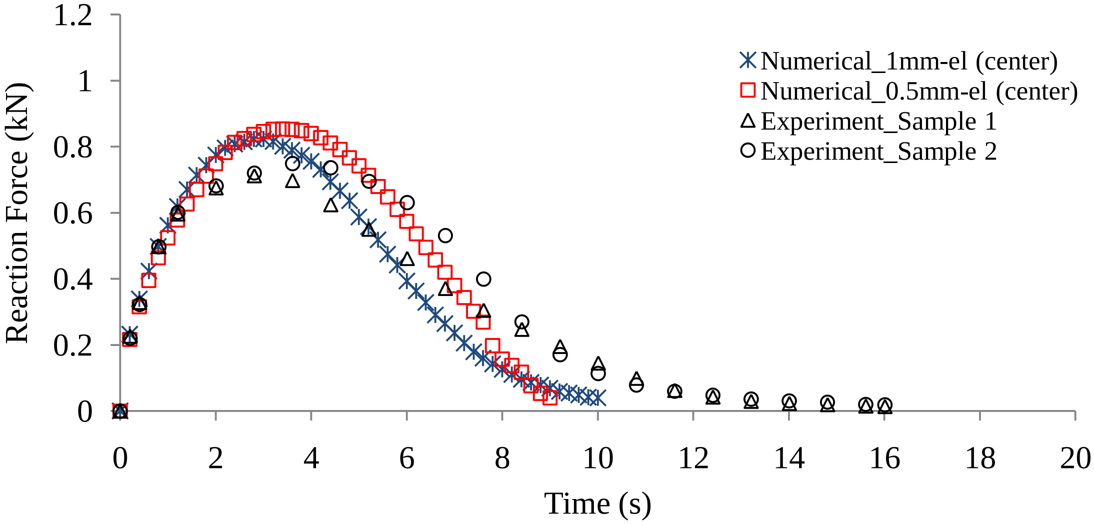

Figure 34: Mode I fracture parameter's calibration.

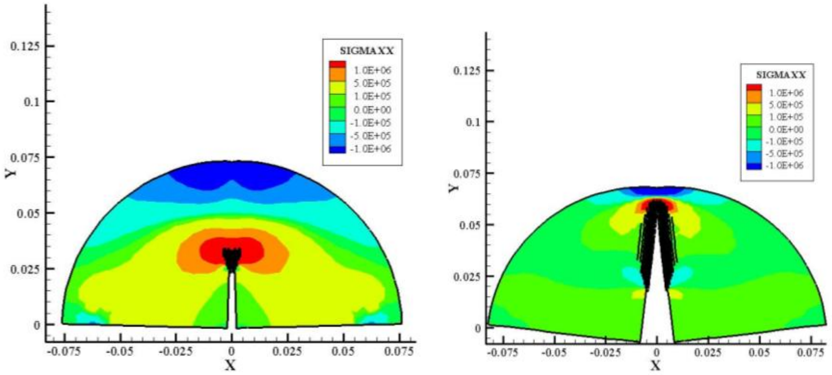

(a) t=2.6 s (peak load)

(b) t=8.0 s (failure)

Figure 35: SCB simulation snapshots at different loading times.

As illustrated in Figure 34, numerical and experimental results are matching well. Regarding the mesh refinement, the magnitude of the peak force and the shape of the curve did not change significantly considering the two levels of refinement used. A small difference in the softening curve could be observed between the two numerical results, but they are within the experimental bias. Thus, one could obtain the mode I fracture parameters.

Finally, one needs to obtain mode II fracture parameters. Ban *et al.* (2011) performed a series of semi-circular bending tests varying the supporting condition to examine the fracture behavior of bituminous composites. The authors performed 3-point bending tests at a constant displacement rate of 0.17mm/s on SCB samples with an inclined notch at 21°C. Depending on the distance of the supports, they observed different fracture behavior of the sample, i.e., pure mode I, mode mixity and pure mode II fracture. They concluded that, considering their testing conditions, the fracture energy required to a complete rupture of a sample in pure mode II was approximately three times the fracture energy required to break a sample in pure mode I. Also, the magnitude of the peak force obtained in pure mode II was about three times the one obtained in pure mode I testing conditions.

Based on their observations, mode II parameters were obtained for the present study. Thus, using Equation 3.16, mode II parameters were determined by varying the magnitude of δ_s^* and σ_s^f until the fracture energy (the area under the curve *traction vs. cohesive displacements*) and the maximum traction for a pure mode II fracture were found to be approximately three times the ones required for pure mode I fracture, as shown in Figure 36.

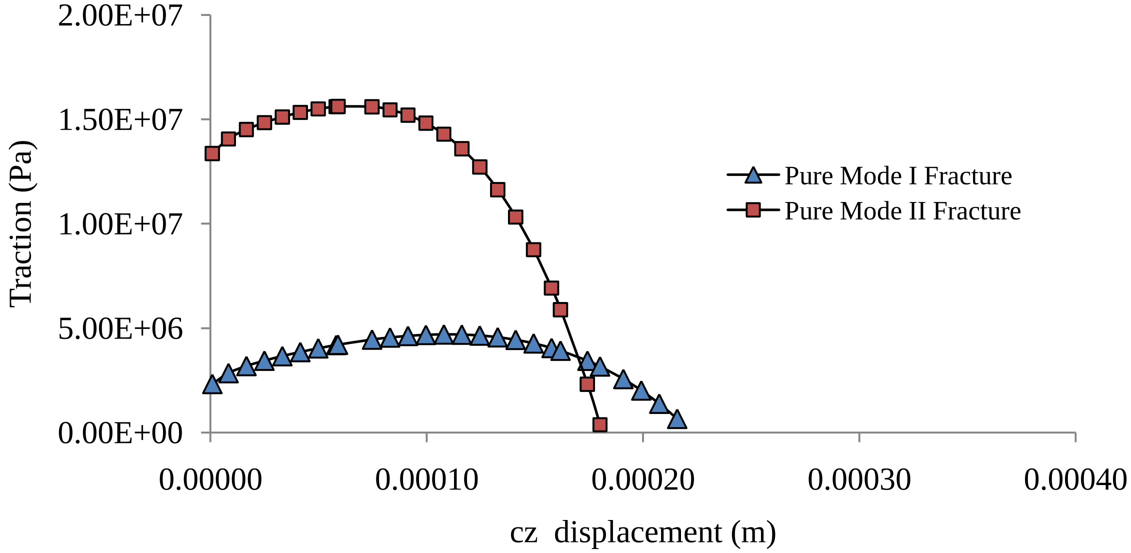

Figure 36: Traction vs. cohesive zone displacement curves for both pure mode I and pure mode II fracture process.

As noticed in Figure 36, the fracture energy and maximum traction in pure mode I were approximately three times the ones in pure mode II. Table 4 summarizes the fracture damage parameters obtained with the methodology employed herein.

Table 4: Fracture damage parameters for cohesive zone model simulations.

Fracture-Damage Parameters (Cohesive Zone)	
δ_n^*, δ_s^*	20 mm, 15 mm
σ_n^f, σ_s^f	2.2E+06 Pa, 1.37E+07 Pa
A	1.00E+06
m	2.5

**Viscoelastic relaxation modulus is the same as that given for the asphalt matrix*

Chapter 5

Representative Volume Element - RVE

An RVE is defined as the smallest but sufficiently large volume element that can represent the effective properties of the large-scale composite. Thus, the mechanical analysis of a large heterogeneous asphalt composite can be reasonably converted into the mechanical analysis of much smaller heterogeneous mixtures, since the selected smaller sample (RVE) is sufficient to reflect the overall statistically homogeneous behavior of the large-scale bituminous mixture. RVEs have significant benefits, since they can be the objects of measurement in laboratory tests.

Another clear benefit of defining RVEs is related to the mechanistic modeling of bituminous composites. One of approaches currently receiving increasing attention from the asphalt mechanics community is computational micromechanics modeling. This approach is probably the best way to account for the effects of individual mixture constituents and their interactions on the overall behavior of asphalt mixtures with regard to heterogeneity, anisotropy, nonlinear inelasticity, and even damage growth. To perform micromechanics modeling, appropriate RVEs must be identified, because a micromechanics model requires the effective properties of a heterogeneous bulk mixture obtained by a homogenization process dealing with a heterogeneous RVE. The beauty of micromechanics is therefore highlighted through the concept of RVEs.

In spite of the significance and potential benefits of RVEs, thus far, there have not been many attempts to determine appropriate RVE dimensions in asphalt mixtures. Traditional RVE conditions are specified in ASTM D-3497 (2003) which defines proper dimensions of specimens with two primary requirements: 1) the ratio of specimen diameter (D) to maximum aggregate size should be 4:1, and 2) the minimum ratio of specimen height (H) to specimen diameter (D) should be 2:1. For a better understanding of RVEs in asphalt concrete mixtures, several studies have been conducted by researchers (Weissman *et al.*, 1999; Harvey *et al.*, 2000; Witczak *et al.*, 2000; Chehab *et al.*, 2000; Romero and Masad, 2001; Wen and Kim, 2002; Kim and Wen, 2002; Wagoner and Buttlar, 2007). Table 5 briefly summarizes each study with its research methods and key findings. As is evident from the table, most studies were based on experimental approaches by repeating mechanical tests with different specimen dimensions.

A common observation from these studies is that the RVE size of asphalt mixtures is clearly dependent on the maximum aggregate size in the mixtures, and a larger RVE is necessary when the test involves damage. Stiffness characteristics of mixtures without damage can be identified from a smaller RVE, because the spatial heterogeneity of the mixtures is mostly due to aggregate structure which does not likely change during the test. However, performance tests, which are associated with damage, need a larger RVE, since they are subjected to the additional mixture heterogeneities such as cracks, localized yielding, and possibly aggregate movements.

Table 5: Summary of Some Studies to Better Understand Asphalt Concrete RVEs

Literature	**Research Method**	**Significant Findings**
Weissman *et al.* (1999)	Finite Element Simulations, Laboratory Tests (restricted triaxial test, RSST-CH[1])	Restricted triaxial test: 125 mm D and 350 mm H, RSST-CH: length-to-height ratio at least 3.
Harvey *et al.* (2000)	Laboratory Test (RSST-CH)	The sizes of specimens are not sufficiently large to evaluate specimen shape.
Witczak *et al.* (2000)	Laboratory Tests (uniaxial compression test, constant height shear test)	Uniaxial compression test: 70 mm D with a minimum H/D ratio of 1.5 for undamaged tests and 100 mm D by 150 mm H is adequate for mixtures with damage, Constant height shear test: mechanical responses were dependent on specimen size; RVE could not be defined.
Chehab *et al.* (2000)	Laboratory Tests (uniaxial tensile tests with and without damage)	75 mm D and 150 mm H meets RVE requirements for mixtures with maximum aggregate sizes up to 19 mm, 100 mm D and 150 mm H geometry is more appropriate for larger-size aggregate mixes.
Romero and Masad (2001)	Laboratory Tests (image analysis, Superpave shear tester)	For an Superpave shear tester specimen (150 mm D and 50 mm H), the nominal maximum aggregate size of the mixture should be smaller than 25 mm.
Wen and Kim (2002) Kim and Wen (2002)	Laboratory Tests (DIC[2] for IDT[3] specimens), 3-D Finite Element Simulations	The 50 mm gauge length on a 100 mm diameter IDT specimen is adequate for creep and strength tests at intermediate temperature.
Wagoner and Buttlar (2007)	Laboratory Test (disk-shaped compact tension test)	Specimen size affects fracture energy, which is typically observed from quasi-brittle materials.

Note. RSST-CH[1]: repeated simple shear test at constant height, DIC[2]: digital image correlation, IDT[3]: indirect tensile test.

As is well demonstrated in the study (Romero and Masad, 2001), the use of the image analysis technique for the asphalt concrete inner structure may be a sound alternative to the costly laboratory performance tests for an identification of the RVE particularly for the cases without damage, because the microstructure image analysis can provide actual information of geometric heterogeneity of the mixture. For the cases with significant damage, the use of a digital image correlation (DIC) technique can be recommended, since DIC can capture real-time and continuous variations in three-dimensional deformation and strain of mixture components with high-resolution cameras (Seo *et al.*, 2002; Seo *et al.*,2004; Birgison *et al.*, 2007).

5.1. Requirement of RVE: Statistical Homogeneity

One of primary requirements for an appropriate RVE is statistical homogeneity: in other words, the averaged characteristics (mechanical or geometrical) in an RVE should be statistically homogeneous so that the bulk sample characteristics and the RVE characteristics are the same. In the case of complex particulate composites such as asphalt concrete mixtures where aggregate particles in various shapes and sizes are dispersed randomly in the asphalt binder, the identification of an appropriate RVE is not trivial due to the significant geometric complexity of the mixture.

To perform the two-way coupled multiscale modeling, a local scale RVE is required. Thus, one of the objectives of this research is to identify a proper RVE dimension of a bituminous composite. As demonstrated by Kim *et al.* (2009), the use of image analysis technique coupled with numerical simulations can be a potentially efficient approach to define the RVE of asphalt mixtures with much less time and efforts.

In this study, geometric analyses of aggregate particles and finite element numerical simulations of effective property of bituminous specimens were performed and compared to each other to reach general findings.

5.2. Image Analysis of Asphalt Mixture Geometrical Characteristics

To investigate the geometrical characteristics of heterogeneous bituminous mixture samples, mixture RVEs were sought through the image analysis technique. Various geometrical factors such as area fraction, gradation, orientation, and the spatial distribution of aggregate particles in the mixtures were considered altogether using two-dimensional actual images of the studied bituminous mixture inner structures produced by digital image processing. Thus, one could define, based on geometrical averaged characteristics, the minimum sample size of an asphalt specimen in order to represent the asphalt mixture overall behavior.

Small subsections (referred to as trial representative volume elements: TRVEs in this study) with increasing sizes were obtained using the image described in the earlier chapter (Figure 26 b). The adjusted binary image of the bituminous specimen was divided into only two distinct phases: white aggregate particles and a black asphalt matrix phase (that is a composite of asphalt binder, fine aggregates passing through sieve No. 50, mineral fillers, and entrained air voids).

The RVE size was identified by comparing the mixture characteristics obtained from several TRVE sections. Various mixture characteristics obtained from each TRVE were plotted against the TRVE size. Then, the geometrical size at which all the mixture characteristics were not significantly dependent on the TRVE size, indicating convergence, was determined as the appropriate RVE size, as illustrated in Figure 37.

As mentioned earlier, various geometrical factors were considered. All geometrical analyses for each digital image (TRVE) of each mixture were accomplished by using an image analysis software, *ImageTool* (University of Texas, 1997). The volume fraction (or area fraction in the case of two-dimensional objects such as the one herein) of aggregates in each TRVE was first monitored, since the area fraction is a primary variable associated with RVE in classical micromechanics (Hashin, 1983; Romero and Masad, 2001).

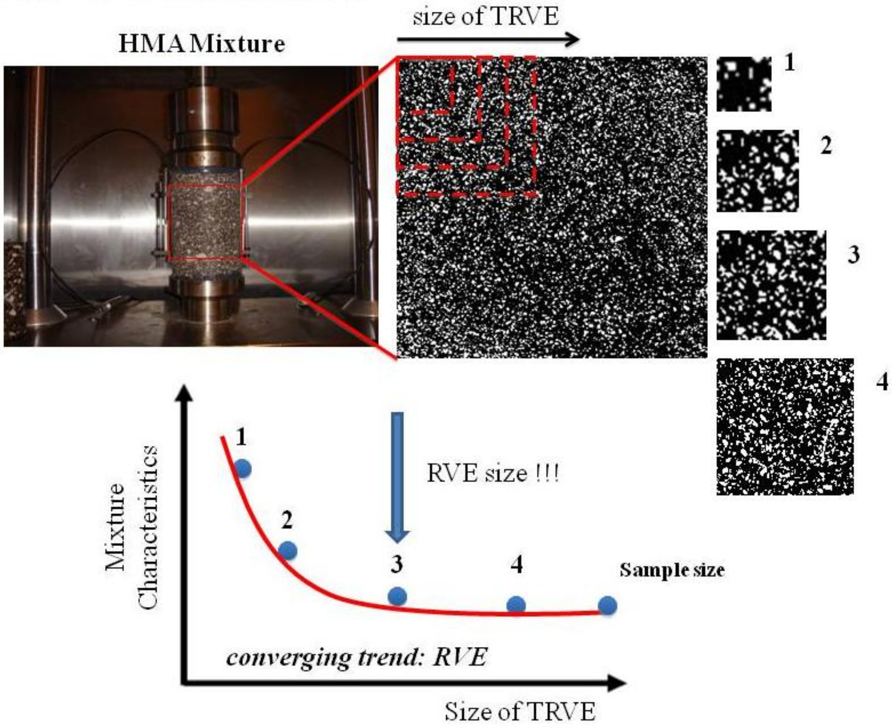

Figure 37: Conceptual process for determining RVE geometry.

Although the area fraction clearly provides important geometric characteristics of an asphalt mixture, it is not sufficient to identify the RVEs, because it cannot account for the size distribution of the aggregate particles in the mixture. Thus, there is a need to investigate the aggregate size distribution in a mixture in order to monitor the existence of any concentration of specific particle sizes. In an attempt to account for the particle size distribution properly, the percentage of each particle size in the image was accounted. The percentages of each particle size obtained from the image analysis of each TRVE were plotted against the TRVE size. This process attempted to quantify the gradation characteristics as a number for more efficient comparison among TRVE sections. As the TRVE size increases, the gradation variation between subsequent TRVE sections will be smaller, indicating that the TRVE is closer to the RVE.

After the area fractions and the gradation characteristics were studied, each TRVE was sub-divided into four quadrants, as illustrated in Figure 38, to calculate the total number of particles in each sub-quadrant. This was conducted as a parallel step to the assessment of the gradation characteristics (particle size distribution) since spatial inhomogeneity could still have existed, even if the TRVE satisfied both the area fraction and gradation criteria. In order to completely satisfy the condition for spatial homogeneity, the aggregate particles must be well dispersed in the mixture, i.e., all quadrants must show a similar number of particles and approximately the same mean area. This implied that aggregates of different sizes must be equally and randomly distributed in the whole sample. The coefficients of variation (ratio of the standard deviation to the mean value in the quadrants) in each TRVE were calculated and compared.

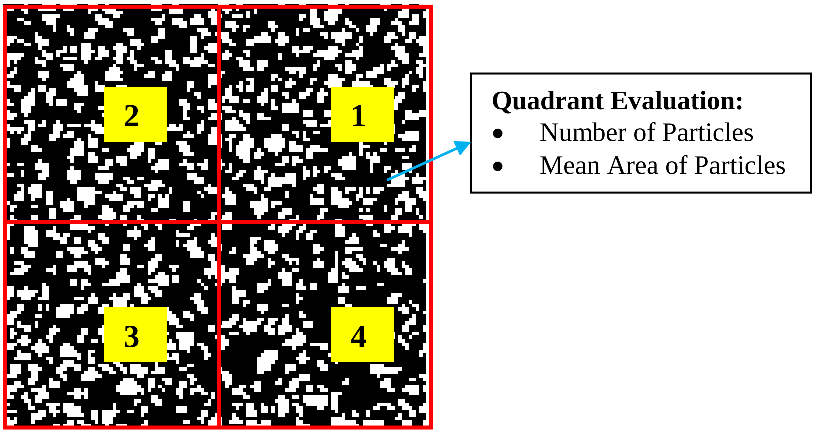

Quadrant Evaluation:
- Number of Particles
- Mean Area of Particles

Figure 38: Aggregate distribution analysis on the quadrants.

Another important geometrical factor to be considered is the aggregate orientation, which is determined by measuring the angle between the major axis of an aggregate and a horizontal line on the scanned image. To quantify the aggregate orientation, the vector magnitude (Δ) was calculated using Equation 4.1. The vector magnitude has been proved in numerous studies to be a useful indicator to quantify the directional measurements of aggregates (Masad *et al.*, 1999; Muhunthan *et al.*, 2000). The value of the vector magnitude varies from 0 to 100%: a value closer to 0% indicates that the aggregates are more randomly oriented.

$$\Delta = \frac{100}{n}\sqrt{\left[\sum \sin(2\theta_i)\right]^2 + \left[\sum \cos(2\theta_i)\right]^2} \tag{4. 4}$$

where n refers to the total number of particles and θ_i represents the minor angle of orientation of each particle .

5.3. Finite Element Simulation of an Asphalt Mixture Effective Property

Effective material properties of selected TRVE sizes were obtained and compared to check if the effective material properties observed from the potential RVE were representative with respect to the bulk bituminous mixture specimen. In this study, the effective property considered was the linear viscoelastic relaxation modulus. The choice of relaxation modulus as a parameter of interest could be explained by its relevance in the multiscale models. The stiffness tensor is a key quantity that is homogenized at the local scale and transferred back to the global scale.

To accomplish that, finite element meshes of each TRVE were constructed, and the relaxation modulus testing was simulated by imposing the boundary conditions on each selected TRVE, as illustrated in Figure 39.

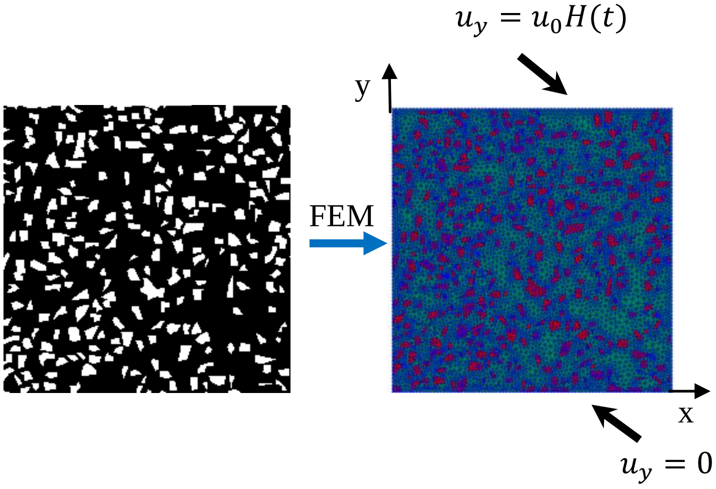

Figure 39: A TRVE and its finite element mesh including boundary conditions.

The material properties of each mixture component (elastic properties of aggregates and viscoelastic properties of matrix phase) used for the RVE study numerical simulations were the ones determined in the previous chapter. State variables (stress and strain) produced from the simulation were then averaged for homogenization, and the homogenized moduli among the TRVE sections were compared to validate the RVE defined from the geometrical estimation.

5.4. Analysis Results

Five specimens were used for this study. A total of seven TRVE sections (window sizes ranging from 2.5 mm to 100 mm) were generated and compared for each mixture. Analysis results considering all five specimens in the form of mean values of each geometric factor and its standard deviation, which is represented by an error bar, to the mean with increasing TRVE sizes were plotted.

The first factor analyzed was the aggregate area fraction. As can be seen in the Figure 40, the variation in the aggregate area fraction of all mixtures was not significantly different as the TRVE window size was larger than 15 mm. Based on this observation, if the area fraction was the only factor considered to judge the RVE size, the RVE could be defined at a window size of around 15 mm; this however, may not be true for the other factors considered.

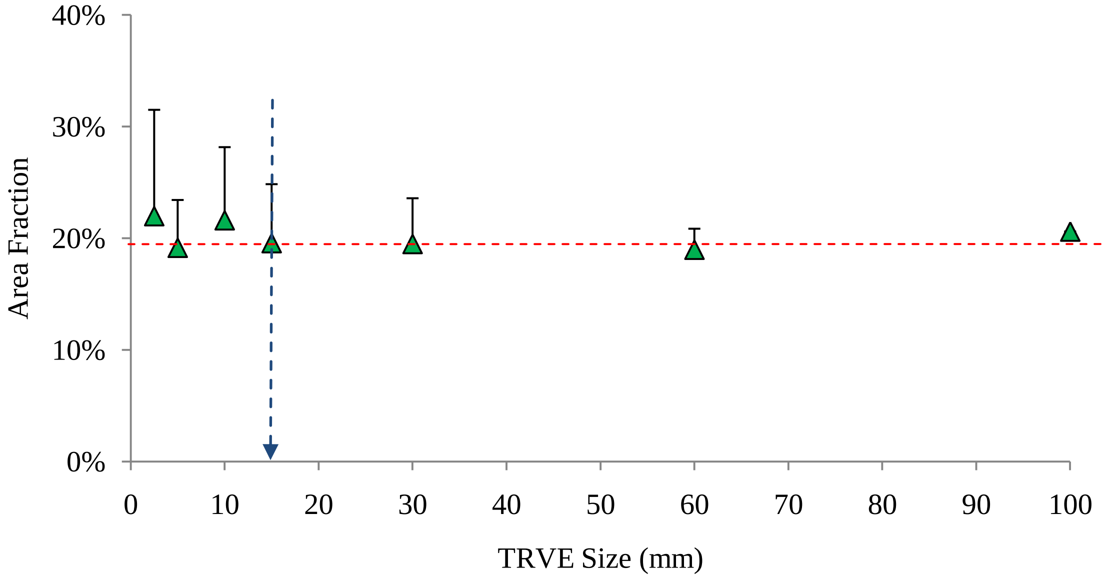

Figure 40: Aggregate area fraction vs. TRVE window size.

A similar plot is shown in Figure 41 for the gradation characteristics. The percentage of each particle size representing the aggregate gradation characteristics was calculated for each TRVE and then plotted in the figure with increasing TRVE sizes. Note that the scan used to digitalize the specimens sections could not capture particle sizes smaller than 0.25 mm. Thus, the minimum sieve size captured was the sieve no. 50. Clearly, with a larger TRVE size, the gradation variation between subsequent TRVE sections tends to decrease, indicating that the TRVE approaches the RVE. The RVE could be defined at around or even less than a 15 mm window size.

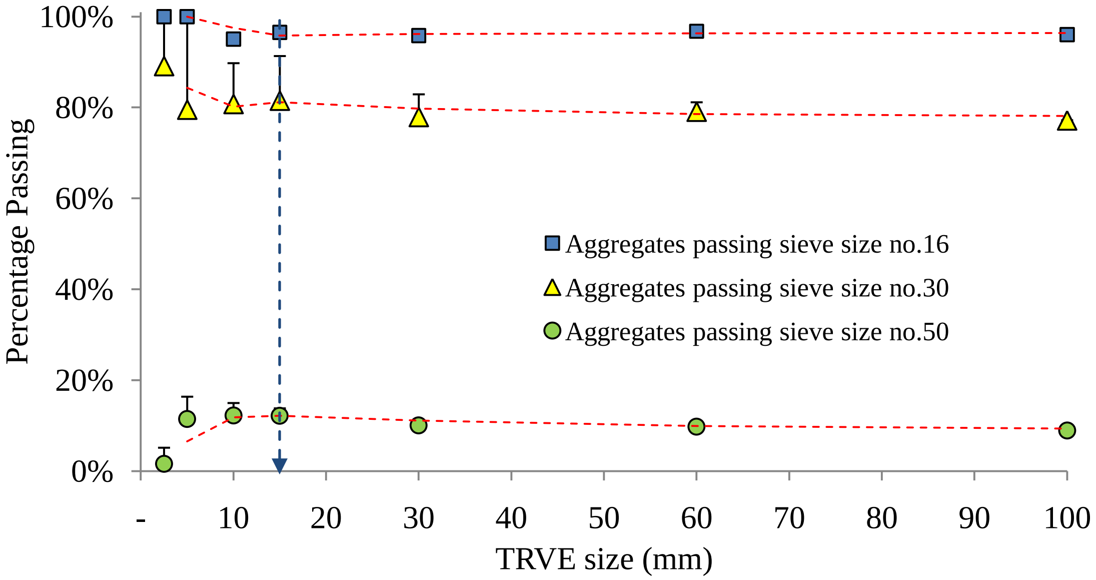

Figure 41: Percentage of particles in each sieve size vs. TRVE window size.

Figure 42 presents the coefficients of variation among quadrants in each TRVE as the window size of TRVE varies. As mentioned earlier, two factors (i.e., the number of aggregate particles and the mean area of aggregates) in each quadrant were obtained and the coefficients of variation of these factors among quadrants were calculated. If the coefficient of variation is close to zero, the difference among quadrants is negligible. As a parallel step to the assessment of the gradation characteristics, this analysis is useful to monitor any potential existence of spatial inhomogeneity due to poor particle distribution.

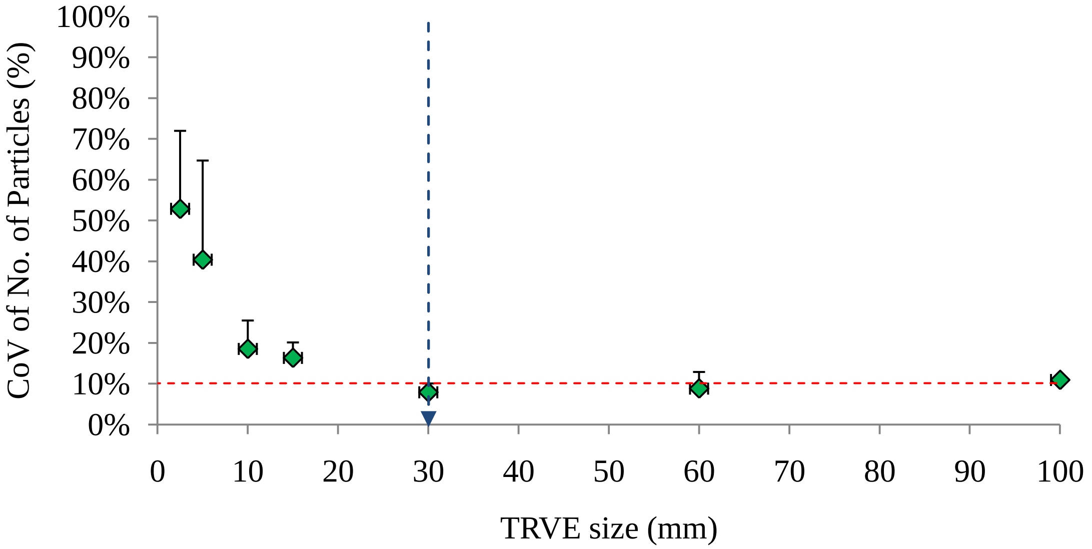

(a) the number of aggregate particles

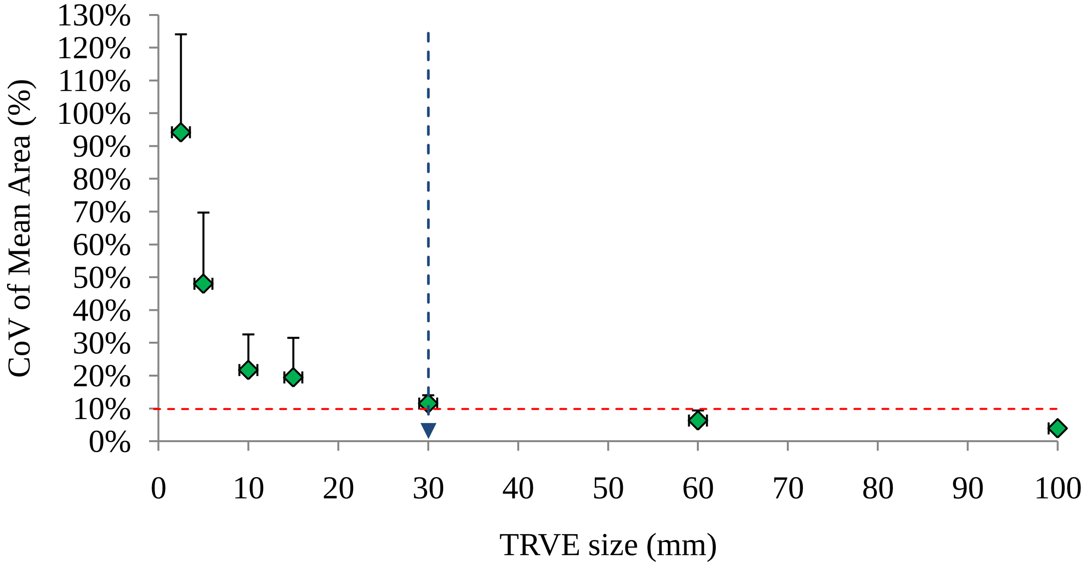

(b) mean area of aggregate particles

Figure 42: Coefficient of Variation on the quadrants considering: a) Number of Particles, and b) Average Particle Area.

As can be noticed from Figure 42, the larger was the TRVE, the less was the variation in the number of particles and the mean aggregate area among quadrants. If a coefficient of variation of 10% is arbitrarily taken as the limit to establish the RVE, a TRVE of 30 mm could be considered as the RVE in terms of both the number of particles and the mean area of the aggregates.

As for the other geometrical factors, the vector magnitude, used to characterize aggregate orientation, showed converging trends as the TRVE size increased, as demonstrated in Figure 43. Based on this criterion, a TRVE of 15 mm could be defined as the RVE for the studied bituminous mixture.

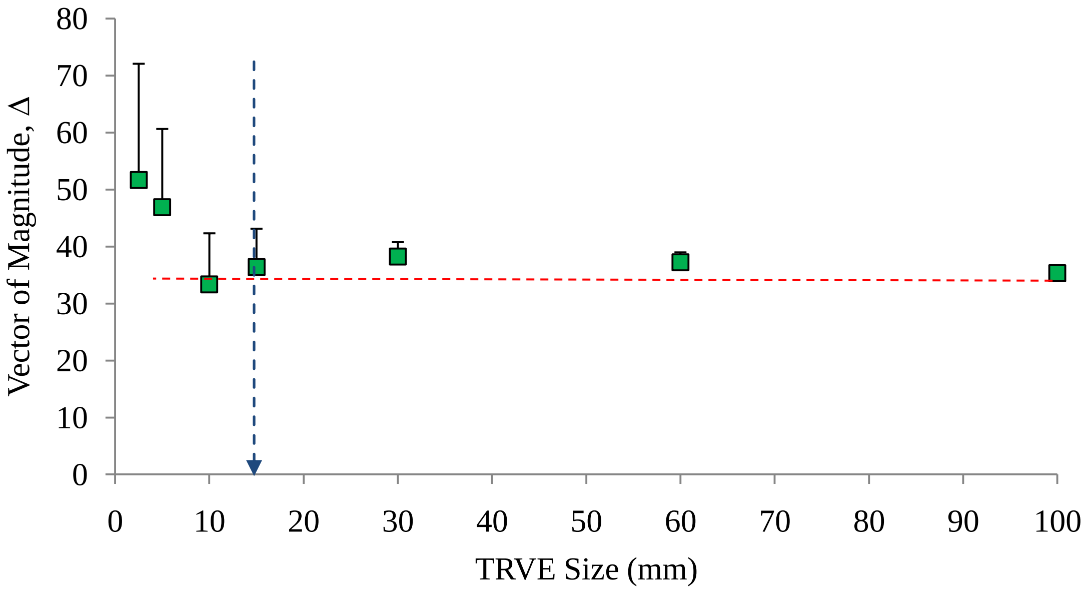

Figure 43: Vector magnitude vs. TRVE window size.

Based on the results of the analysis based on various geometrical factors, it can be inferred that the RVE size of the studied bituminous mixture ranged from 15 mm to 30 mm window size, depending on the geometrical factor analyzed.

Finite element simulations of relaxation modulus test for three TRVE sizes (10 mm, 15 mm, and 30 mm) were performed. Although the geometrical analysis showed that the RVE for the studied mixture would be in the range of 15 mm to 30 mm, the 10 mm TRVE size was also added to the analysis. This decision was taken based on the fact that even though convergence of mixture characteristics was found for TRVE size equal or greater than 15 mm, the difference on the analysis results from the converged value to the 10 mm TRVE size might not be significant, being 10 mm TRVE size still acceptable with certain level of accuracy.

The three selected TRVE images for the numerical analysis were converted to a finite element mesh. Finite element simulations of the relaxation modulus were performed. The homogenized relaxation modulus was obtained by dividing the averaged value of stresses (simulation outputs) by the averaged value of strains (simulation input). Figure 44 shows the three TRVE meshes used for the simulations.

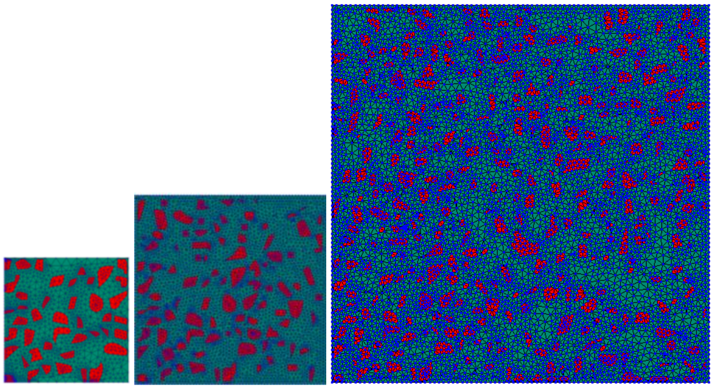

Figure 44: Finite element meshes for TRVE size 10 mm (3274 elements), 15 mm (8372 elements), and 30 mm (16026 elements).

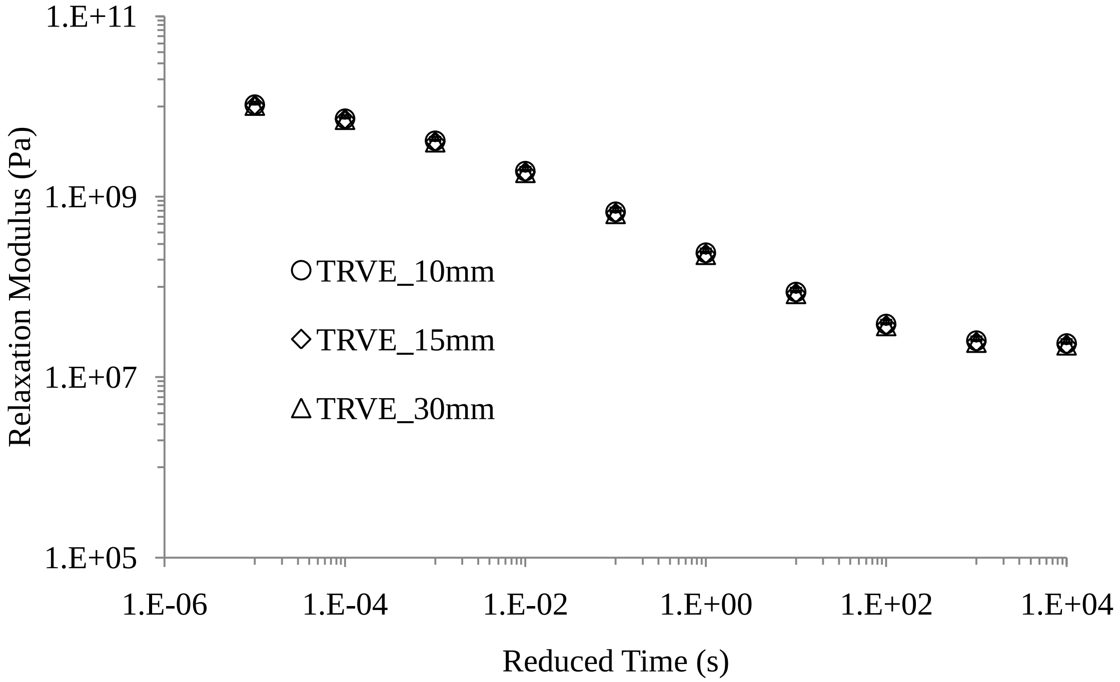

Figure 45: Averaged percent differences among subsequent TRVE sections.

Clearly, the relaxation moduli of the three selected TRVE sizes were not significantly different. In fact, the difference between the relaxation modulus of the TRVE of 10mm and the TRVE of 30mm (RVE based on geometric analysis) were only 2%. Regarding the level of refinement, the finite element mesh required to discretize all heterogeneities in the TRVE of 30mm was around five times the one required to discretize the heterogeneities in the TRVE of 10mm. That would vastly increase the computational time in the multiscale simulations. Thus, the TRVE with 10 mm length size was selected as the RVE microstructure for the model validation.

Chapter 6

Validation-Calibration of the Multiscale Model

In reality, asphalt roadways are subjected to wheel loads, which results on compressive stresses on the pavement structure surface and tensile stresses at the bottom of the asphaltic layer. Subsequently, high tensile strains could be developed and initiate crack at the bottom of the asphalt layer, where the tensile stress is the highest, to the top of the asphalt layer (this type of crack is called the bottom-up crack).

To better assess this phenomenon, the simply supported bending test was conducted to validate and calibrate the two-way coupled model due to its attractive loading mode along the sample, i.e., compression on the top and tension at the bottom of the specimen. Moreover, the bending test setup was easily implemented with the testing machines and supporting tools available at the UNL asphalt laboratory. Three-point bending tests of bituminous composite specimens were performed at 21 °C, and test results were compared to simulation results from multiscale modeling. Figure 46 shows the overall methodology employed to validate the model used herein.

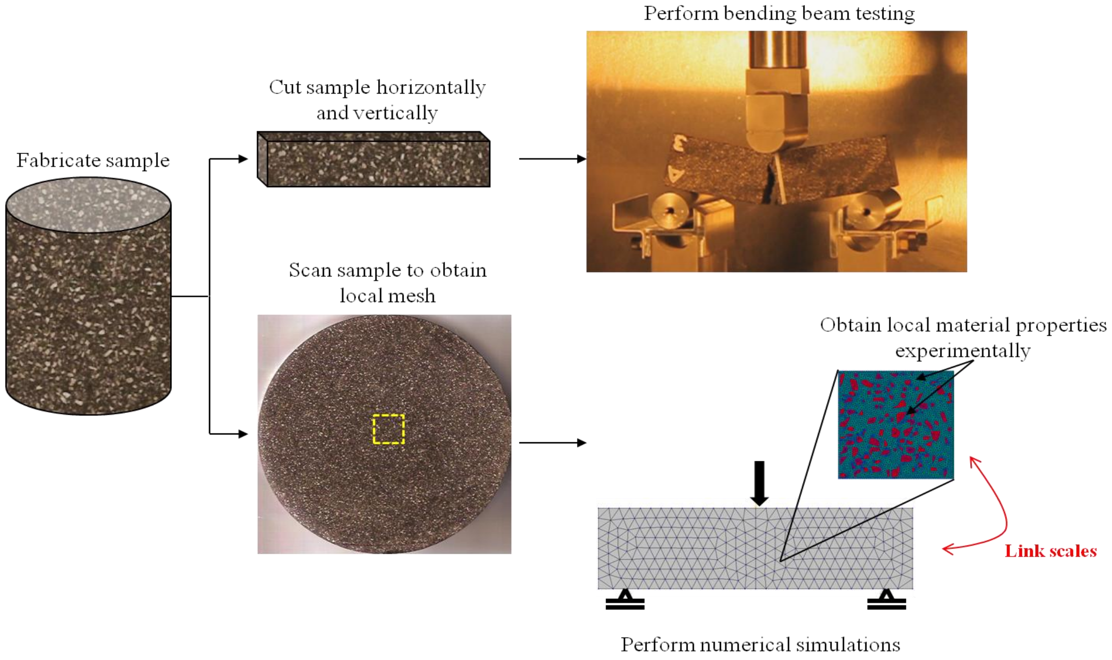

Figure 46: Research methodology employed for the model validation.

6.2. Local Scale Mesh Convergence Study

Prior to performing multiscale simulations, a mesh convergence study was performed to ensure that the level of refinement in the local mesh resulted in converged solutions. The RVE studies performed in Chapter 5 used digital images from an actual bituminous sample produced with the same mixture proportions as those used for the rectangular beam samples.

Thus, for the local scale mesh convergence study, the selected 10 × 10 mm RVE structure was discretized. As shown in Figure 47, local finite element meshes with triangular elements were produced with sizes varying from 0.5 mm to 0.175 mm. An arbitrary constant displacement rate of 0.05 mm/s was applied at the top of the RVE, and the vertical displacements at the bottom were fixed. The particles were assumed to be linear-elastic, and the surrounding matrix was assumed to be linear-viscoelastic.

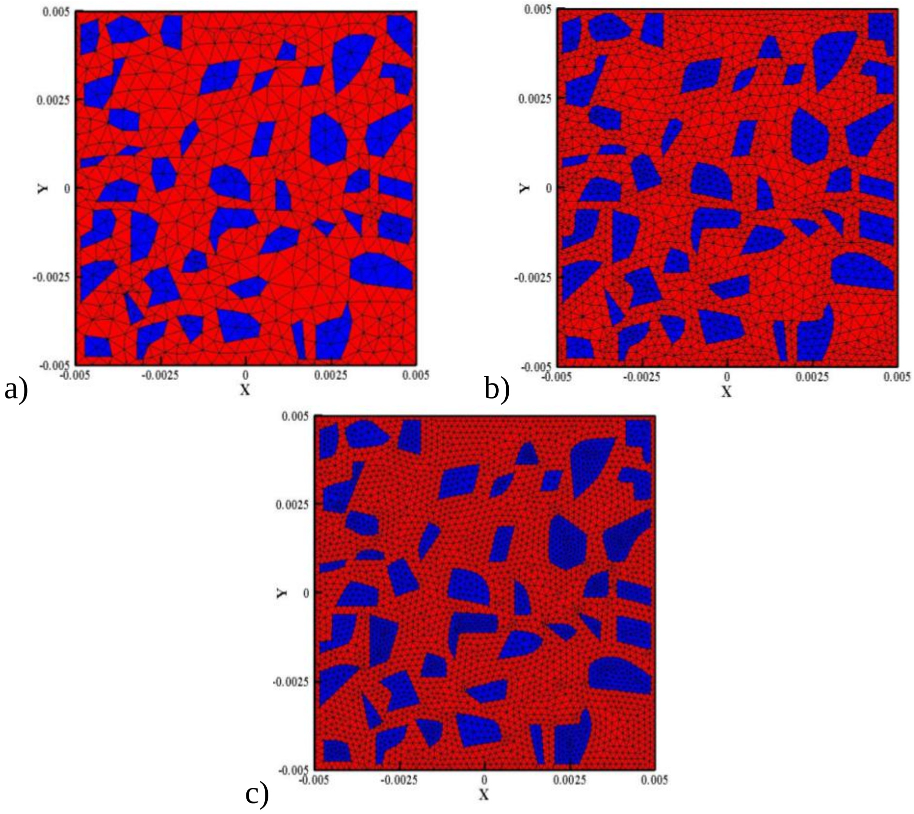

a) b) c)

Figure 47: Finite element meshes used for the local mesh convergence study: a) RVE-1 (1252 elements), b) RVE-2 (3890 elements), c) RVE-3 (7572 elements)

The mesh convergence study was performed for two distinct cases: i) no damage due to cracks was allowed, i.e., the automatic insertion of cohesive zone was turned off during the simulations, and ii) damage due to cracks was added to the problem by allowing cohesive zone elements to be inserted in the mesh as required. Figure 48 shows the average vertical stresses history in the RVE for the different trial meshes for both cases.

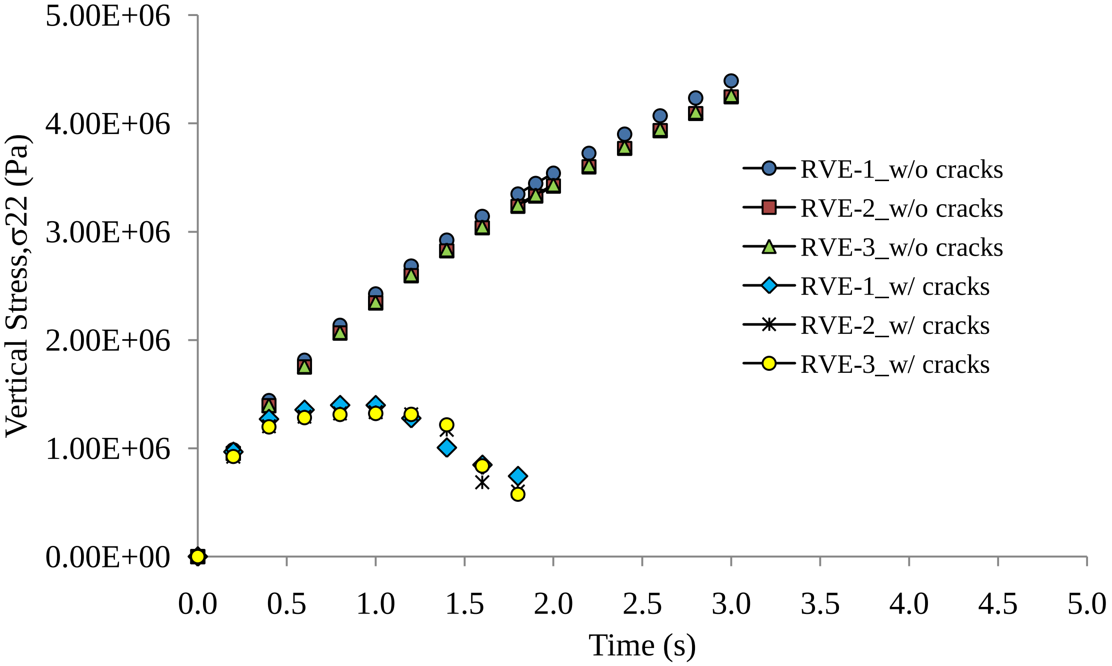

Figure 48: Simulation results for the RVE mesh convergence study.

For a better comparison between the results, the stresses were normalized with respect to the vertical stresses obtained using the finer mesh (Figure 47 c). Figure 49 shows the normalized vertical stresses (at any time) as a function of number of elements for the case where damage due to cracks was not considered. In the case where damage was induced by cracks, the results for the RVE-1 and RVE-2 compared to the reference case (RVE-3) became bigger as the loading time increased, as can be seen in Figure 50.

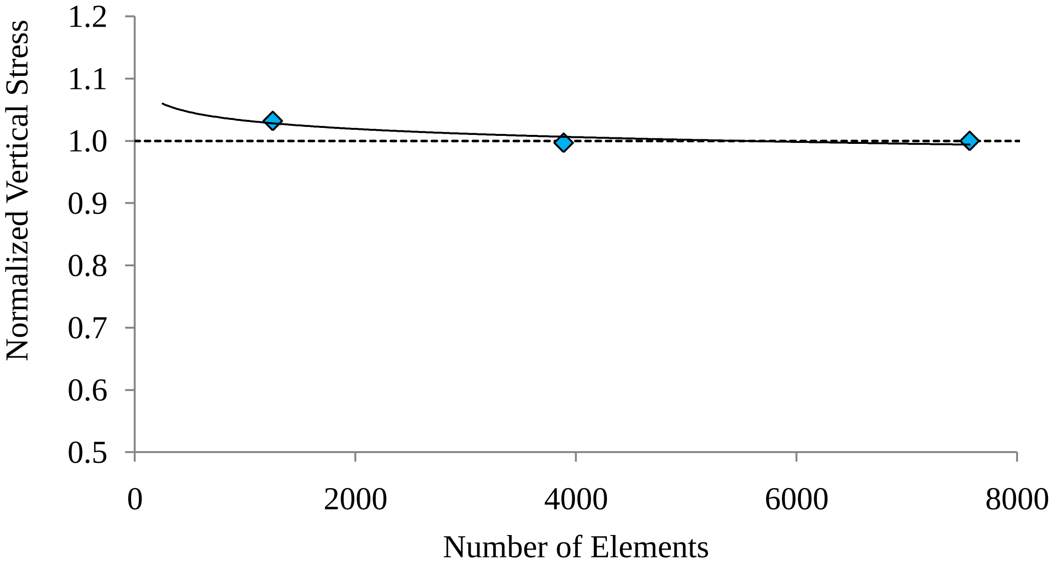

Figure 49: RVE mesh convergence analysis w/o cracks.

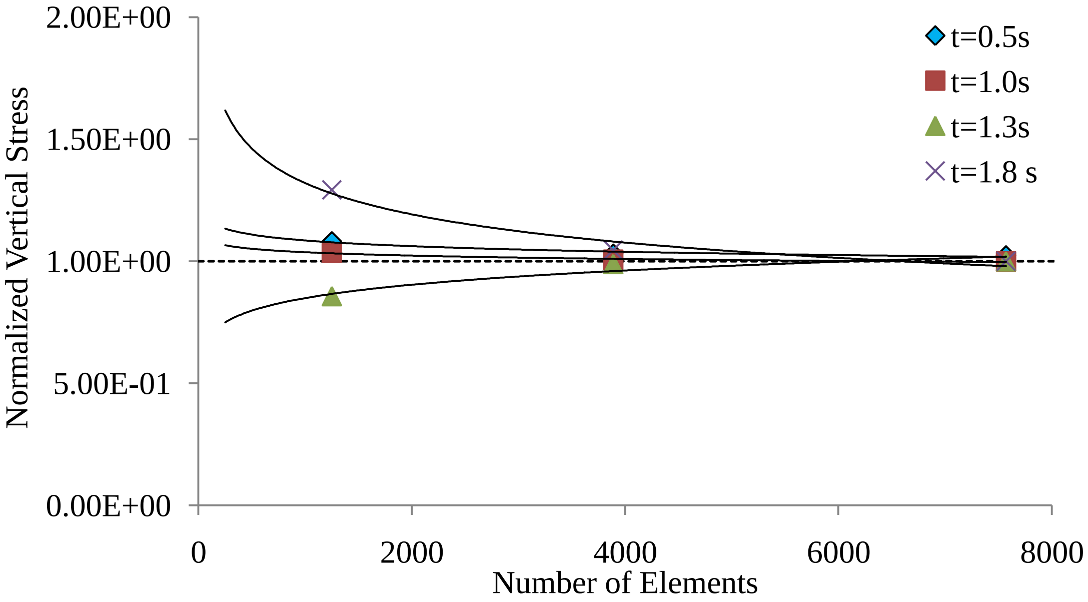

Figure 50: RVE mesh convergence analysis w/ cracks.

Based on the results, a slight difference in the stress values was observed as the level of refinement decreased. For simulations without cracks, the differences in the vertical stress values for RVE-1 and RVE-2 with respect to the finer mesh (RVE-3) were 3.0% and less than 1.0%, respectively. Even though the convergence was reached for RVE-2, the error obtained using RVE-1 was still acceptable for the purpose of this study. Thus, RVE-1 was selected for the multiscale simulations without damage due to cracks to save computational time.

For the simulations with cracks (Figure 50), the results of each studied RVE mesh were not considerably different up to 1.2 seconds, at which no cracks were formed. After this point, the difference between the results of RVE-1 and RVE-2 with respect to RVE-3 became more significant and reached 29% at 1.8 seconds. Using the RVE-2, the difference in the results compared to the finer RVE was reduced to 5%. Since the computational time using a finer RVE (e.g. RVE-3) would be impractical, RVE-2 was selected for the multiscale simulations with damage. Table 6 shows the required time to solve each RVE mesh in Dell workstation using a single Intel Xeon processor at 3.00 GHz running under Linux Fedora 10. Vertical stresses contour plots at 1.8 seconds are shown in Figure 51.

Table 6: Different RVE simulations and computational time

	Mesh	Number of elements	Number of solution steps	Computational time (hour)
w/o cracks	RVE-1	1252	500	0.02
	RVE-2	3890	500	0.08
	RVE-3	7572	500	0.14
w/ cracks	RVE-1	1252	304	0.54
	RVE-2	3890	304	16.02
	RVE-3	7572	304	44.22

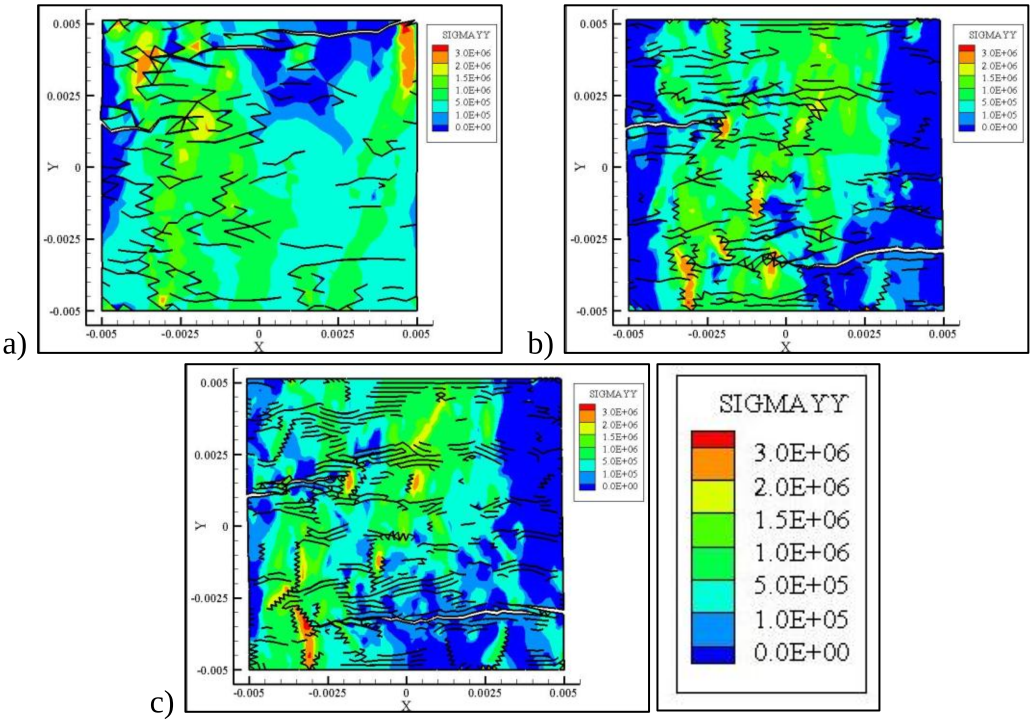

Figure 51: Snapshots at 1.8 seconds for: a) RVE-1, b) RVE-2, c) RVE-3

It can be seen in Figure 51 that the level of refinement in the microstructure affected significantly the crack initiation and propagation in the composite. Even though the averaged stresses were not greatly different, as shown in Figure 48, the crack path found for RVE-1 was completely different from the other two cases.

6.3. Two-way Coupled Multiscale Simulations

The multiscale simulations were accomplished by linking the local scale RVE (10.0 mm × 10.0 mm square), which was modeled with elastic aggregates and viscoelastic bituminous matrix subjected to fracture, to the global scale bending beam performance. Consequently, the global scale bending performance was modeled as a damage-induced, non-linear viscoelastic continuum by a two-way coupling strategy. For the modeling, the load configuration was simulated in the same manner as the test setup. Figure 52 illustrates the overall conditions (load, geometry and boundary conditions) assumed in the multiscale modeling of the bending problems.

The modeling of the three-point bending test was divided in two steps: i) Multiscale simulations without cracks, and ii) Multiscale simulations w/ cracks. Since damage induced by cracks were not considered in the global scale structure, a multiscale mesh convergence study without considering damage at any length scale of analysis was performed to determine the global mesh refinement. Subsequently, using the converged global mesh, a two-way coupled multiscale analysis with damage was performed. The local meshes used in both simulations were the ones determined in the section 6.2 of this Chapter.

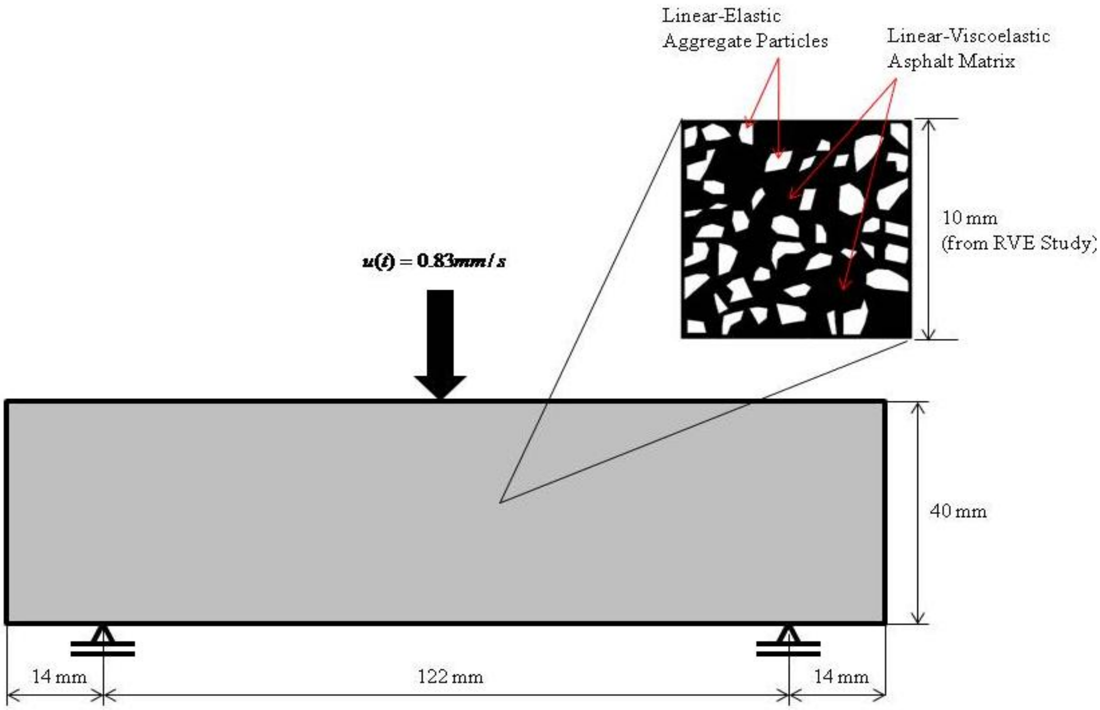

Figure 52: Overall conditions applied in the two-way coupled multiscale modeling of the bending tests.

6.3.1. Global Scale Mesh Convergence Study

The global finite element mesh was determined by performing multiscale simulations without damage. Different global meshes were linked to the local scale RVE (Figure 47a) until the finite element numerical solution converged to an analytical solution. A set of homogeneous global scale meshes in a different level of mesh refinement (10mm to 2.5mm triangular elements as presented in Figure 53) was evaluated. Figure 54 shows the normalized force with respect to the finer mesh (3928 global elements).

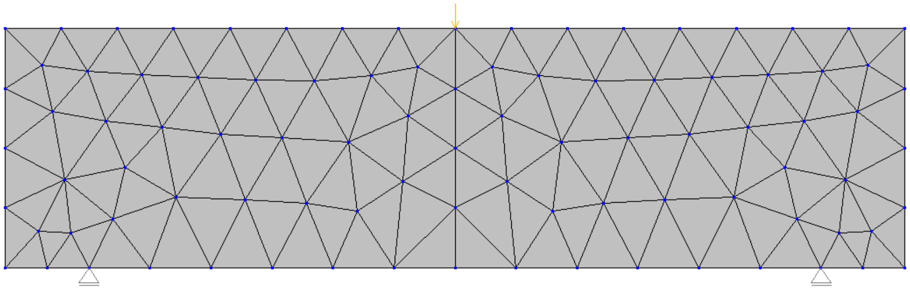

(a) Global 10mm-el size - 144 global elements

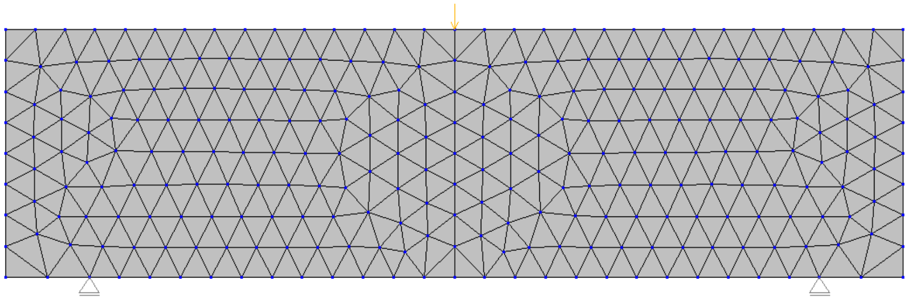

(b) Global 5mm-el size - 466 global elements

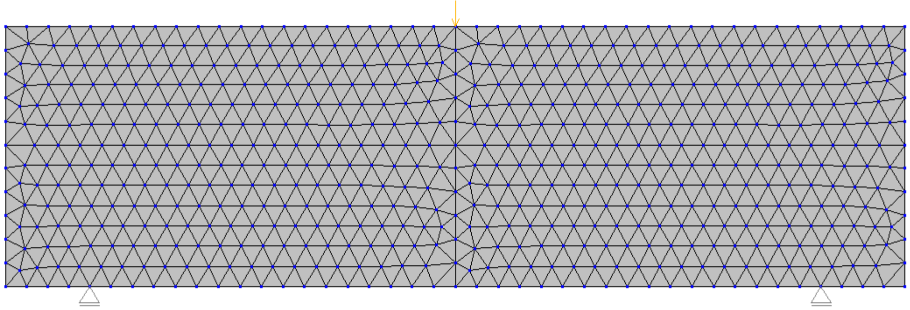

(c) Global 3.5mm-el size - 1088 global elements

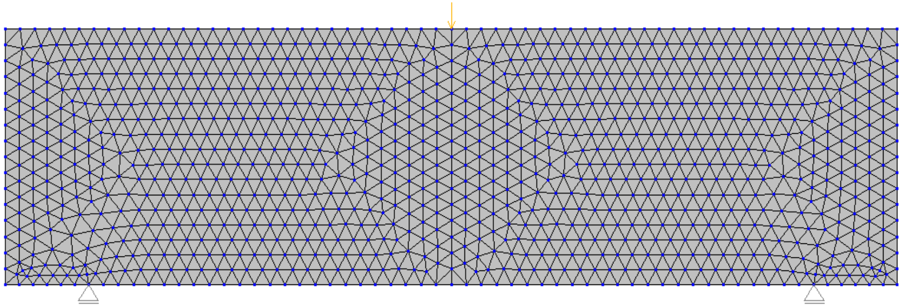

(d) Global 2.5mm-el size - 1998 global elements

Figure 53: Global mesh convergence study for rectangular bending beam problem.

The analytical solution for this problem is given by:

$$P\left(\frac{L}{2}, t\right) = \frac{48\bar{E}I}{L^3}\dot{u} \tag{6. 1}$$

$$\bar{E}(t) = E_\infty^c t - \sum\left(\eta_i^c e^{-\frac{E_i^c}{\eta_i^c}t}\right) + \sum \eta_i^c \tag{6. 2}$$

where P is the reaction force due to the applied displacement rate, L is the beam width, I is the inertial moment, $\dot{u}$ is the applied displacement increment, and $\bar{E}(t)$ is the composite relaxation modulus, which is given in a prony series representation. The prony series coefficients for $\bar{E}(t)$ were obtained by simulating a relaxation test on the heterogeneous RVE.

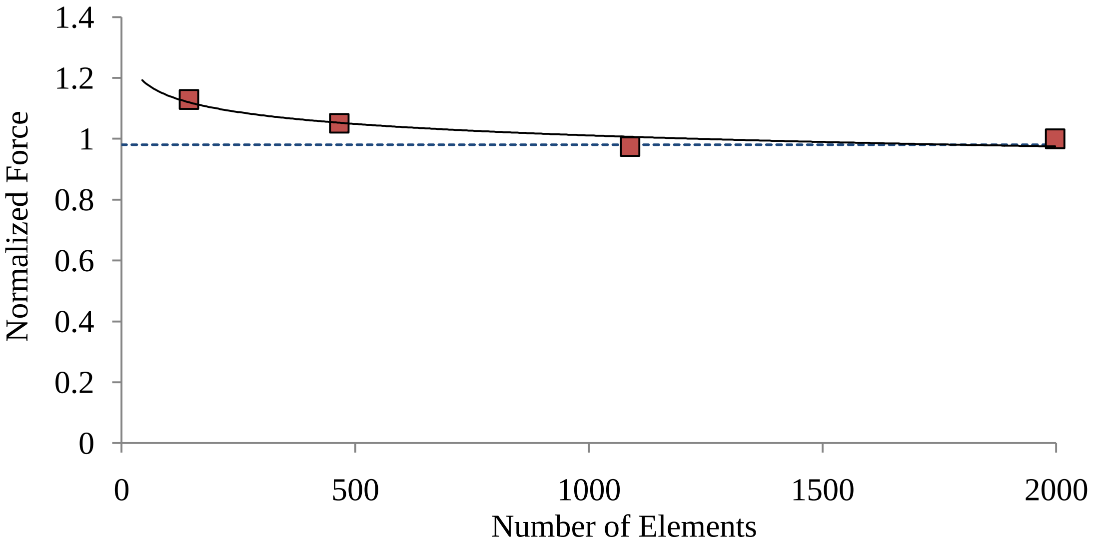

Figure 54: Global scale mesh convergence study for the rectangular beam bending problem.

A convergence trend was observed. However, it should be mentioned that the computation time varied tremendously depending on the number of global elements considered in the two-way coupled analysis. The computation time to solve the multiscale problem (with no damage involved at this point) for the global meshes using 10 mm, 5 mm, 3.5 mm and 2.5 mm triangular elements was 2 hours, 7 hours, 14 hours, and 23 hours, respectively, using 8 Intel Xeon processors from a Dell workstation (3.00 GHz CPU, and Linux OS) . Thus, a balance between the level of accuracy desired and the computational time spent should be well thought-out when defining the finite mesh density. To proceed with the model validation with damage involved, the mesh using 5 mm global triangular elements [Figure 53 (b)] was selected. A comparison of the numerical (without damage at this point), analytical, and experimental results is shown in Figure 55.

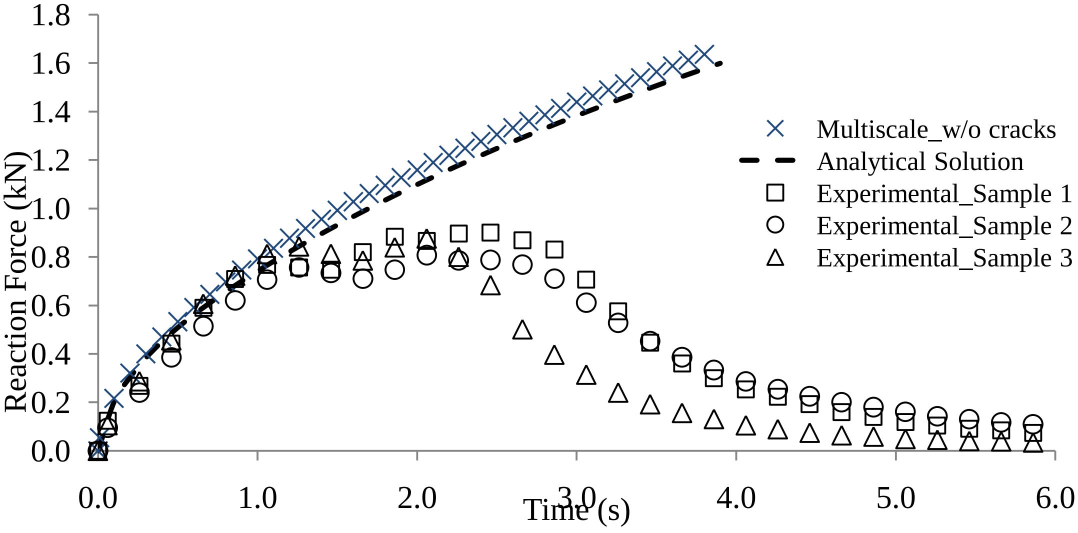

Figure 55: Comparisons among analytical, numerical and experimental results of 3-point bending beam test.

Simulation results showed good agreement with analytical solutions, which once more verified the two-way coupled multiscale model used herein. Because the material heterogeneity was accounted for in the simulation but not for the closed-form solution, a small deviation from the analytical solution was expected, as shown in the figure. Furthermore, the numerical results seemed to follow the experimental curve nicely up to 1.2 seconds, with some energy being dissipated due to the material viscoelasticity. After that point, due to damage, the experimental results curvature started to deviate from numerical results. Thus, at this point, one can say that the model can satisfactorily capture the composite response when damage is not induced.

Aside from the efficiency of the multiscale model, another benefit is the possibility to visualize the small-scale phenomena. Figure 56 shows a snapshot of the deformed mesh and elemental longitudinal stresses at 3.2 seconds for the multiscale simulation without damage due to cracks.

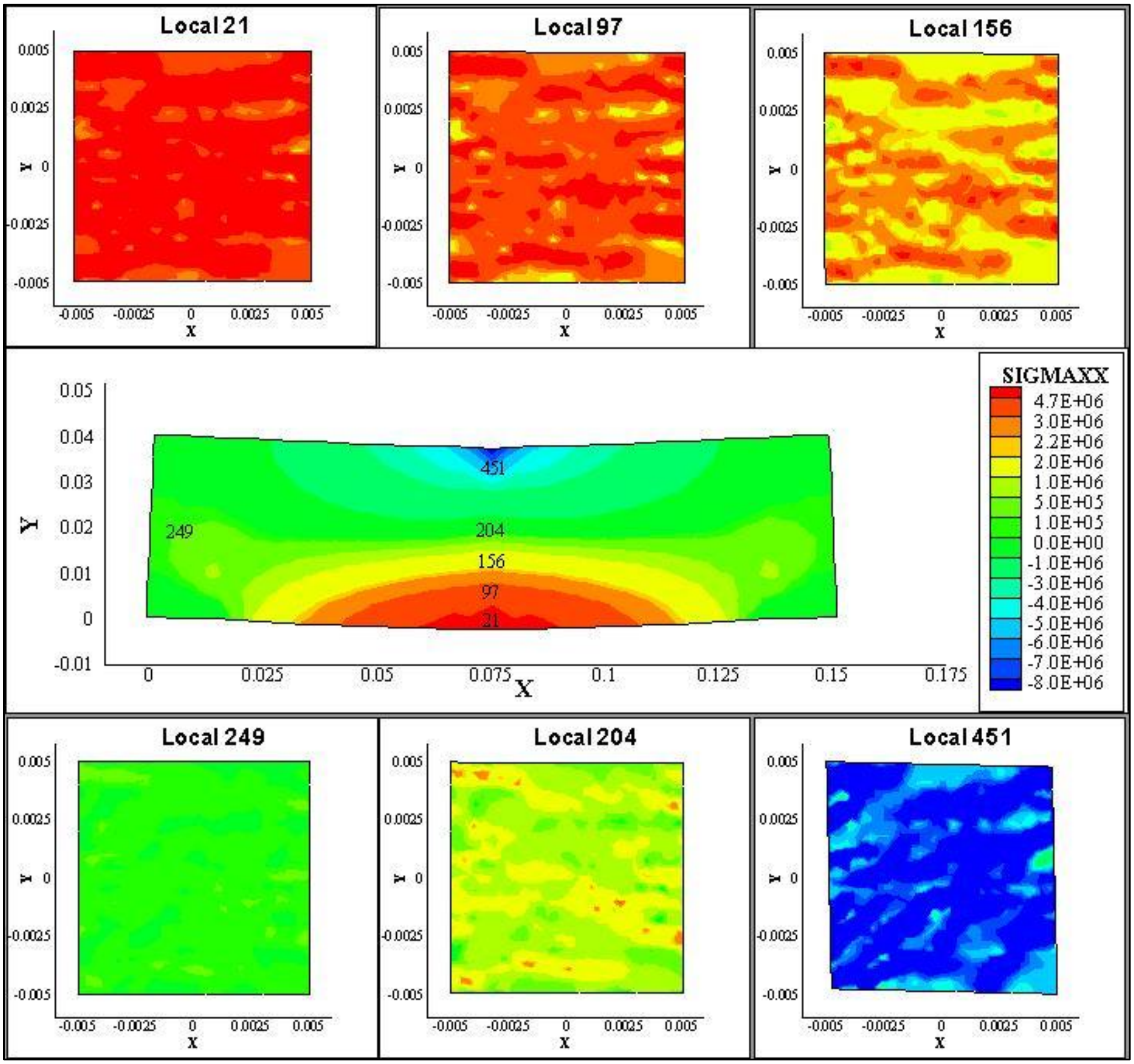

Figure 56: Snapshots Multiscale w/o cracks at 3.2 seconds.

Note that the physics of the problem was captured by the model, as seen by the different stress responses in the selected microstructures. The microstructure linked to the global element 21 (Local 21) showed the highest tensile stress compared to the other elements. This result was expected because higher tensile strains developed at the bottom of the beam based on experimental observations. Similarly, higher compressive stresses were observed in the local microstructure linked to the global element 451.

6.3.2. Validation of Rectangular Beam Bending Test with Damage

The complexity of the problem increased when damage was included in the analysis. To investigate the initiation and propagation of cracks in bituminous composites, it was necessary to include a damage evolution law in the model. As mentioned earlier, the rate-dependent viscoelastic traction-displacement damage model developed by Allen and Searcy (2001) was used. Figure 57 shows a comparison among numerical simulations with and without damage along with experimental results.

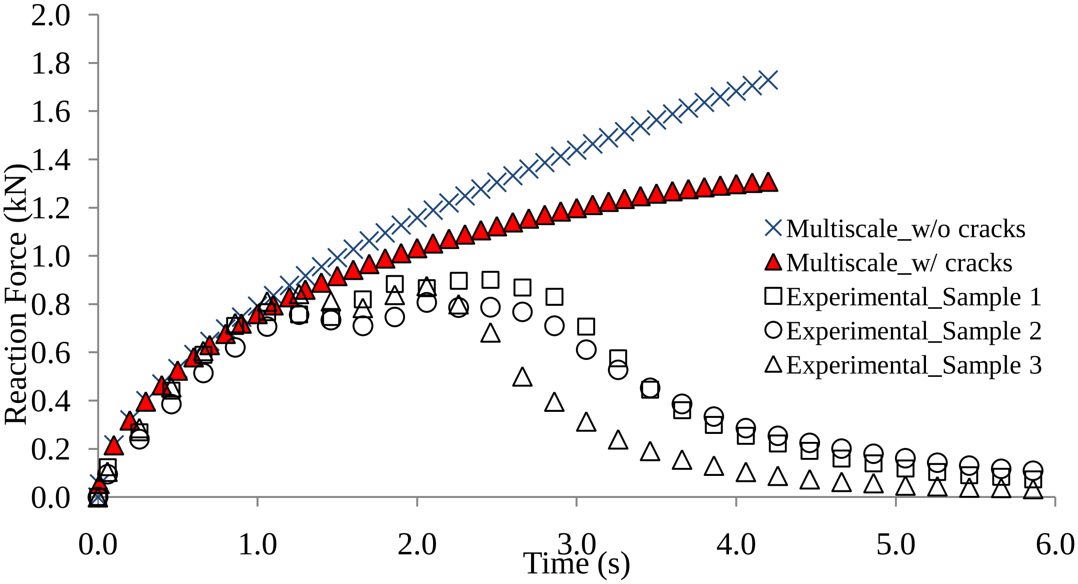

Figure 57: Two-way coupled multiscale simulations with and without damage-induced by cracks and comparisons with experimental results

As can be seen in Figure 57, the initial slope from numerical simulations matched well with the experimental results, which demonstrates that, along with the appropriate constitutive model, the linear-viscoelastic matrix and linear-elastic aggregate material properties used were well determined. Moreover, due to the formation of cohesive zones followed by cracks, it can be noticed in that the average stress deviates from the non-damage (linear viscoelastic) curve. However, the rate of damage propagation seemed to be underestimated, as can be noticed by the simulation with cracks, where the curve is dropping only after 4 seconds. A calibration of damage parameters related to rate of damage propagation is required in order to obtain numerical results closer to the experimental ones. Before performing the calibration of damage parameters, a more detailed analysis of the obtained results was done.

Six local structures were selected for the analysis. They were named according with the global element they were linked. The deformed mesh and elemental stress at both global and local scale structures at selected loading times can be visualized in Figure 58-Figure 62. The global elements selected for local analysis are marked in the global structure snapshots.

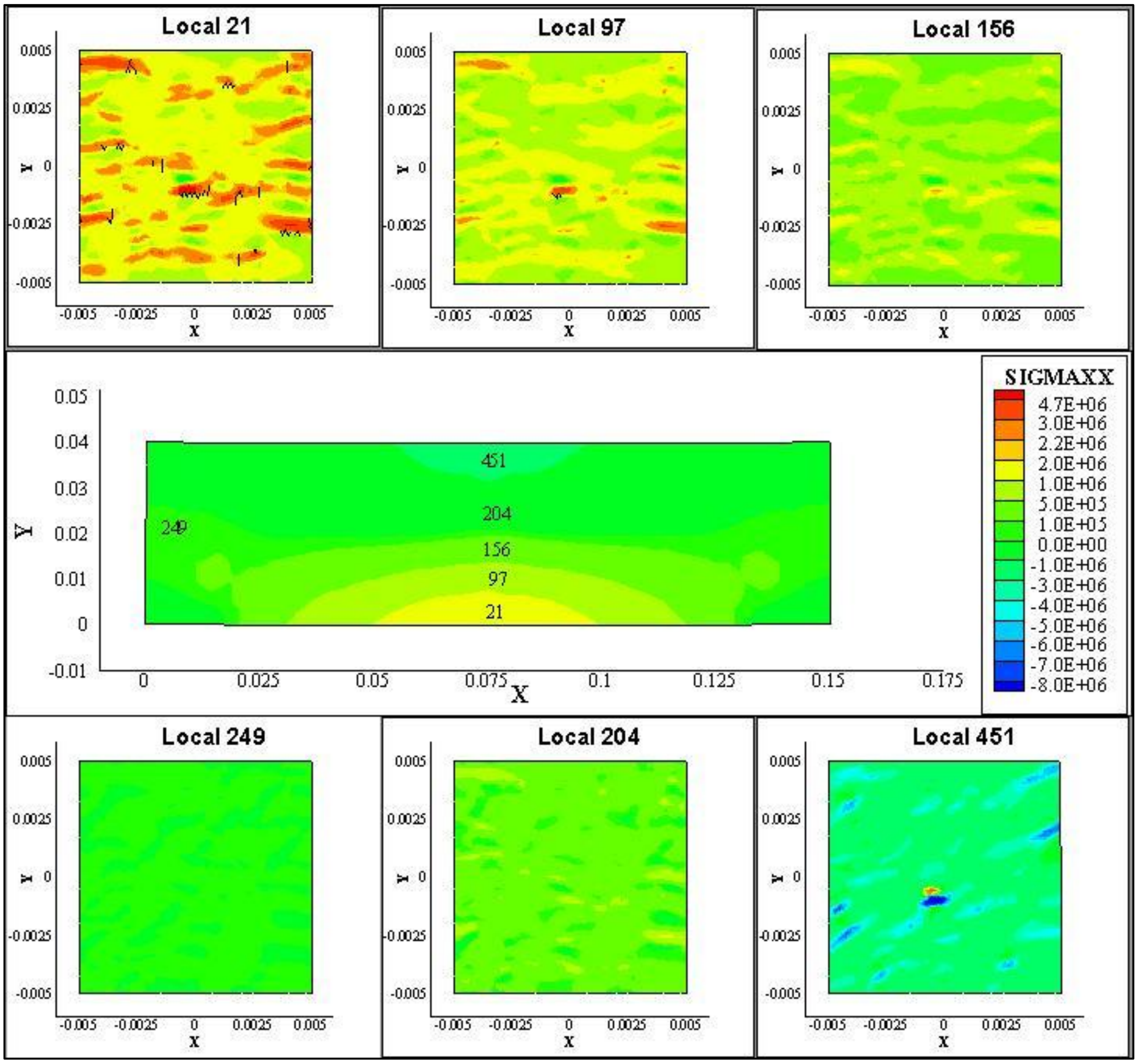

Figure 58: Multiscale simulation with damage-induced - Snapshot at 0.3 seconds.

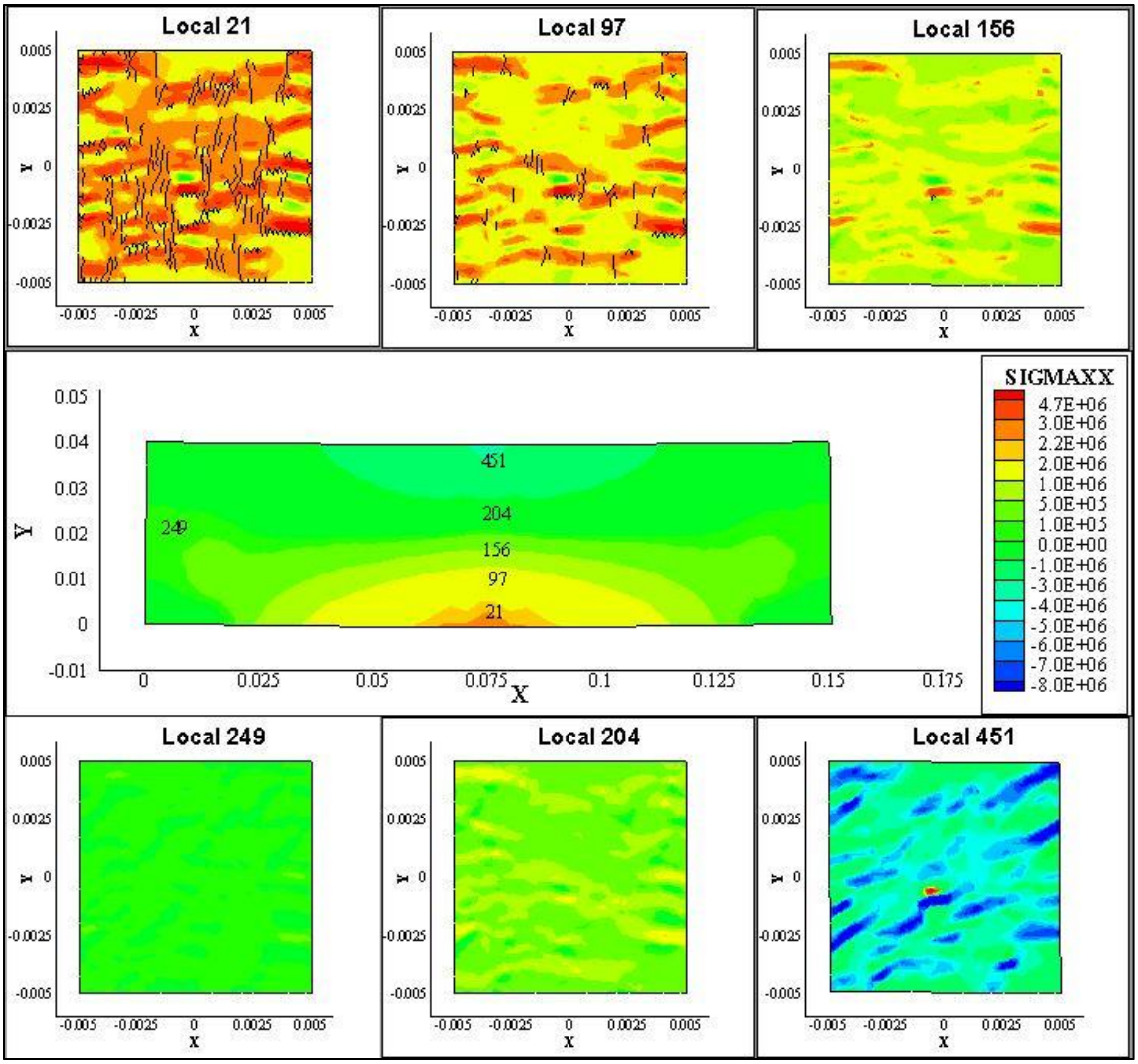

Figure 59: Multiscale simulation with damage-induced - Snapshot at 0.8seconds.

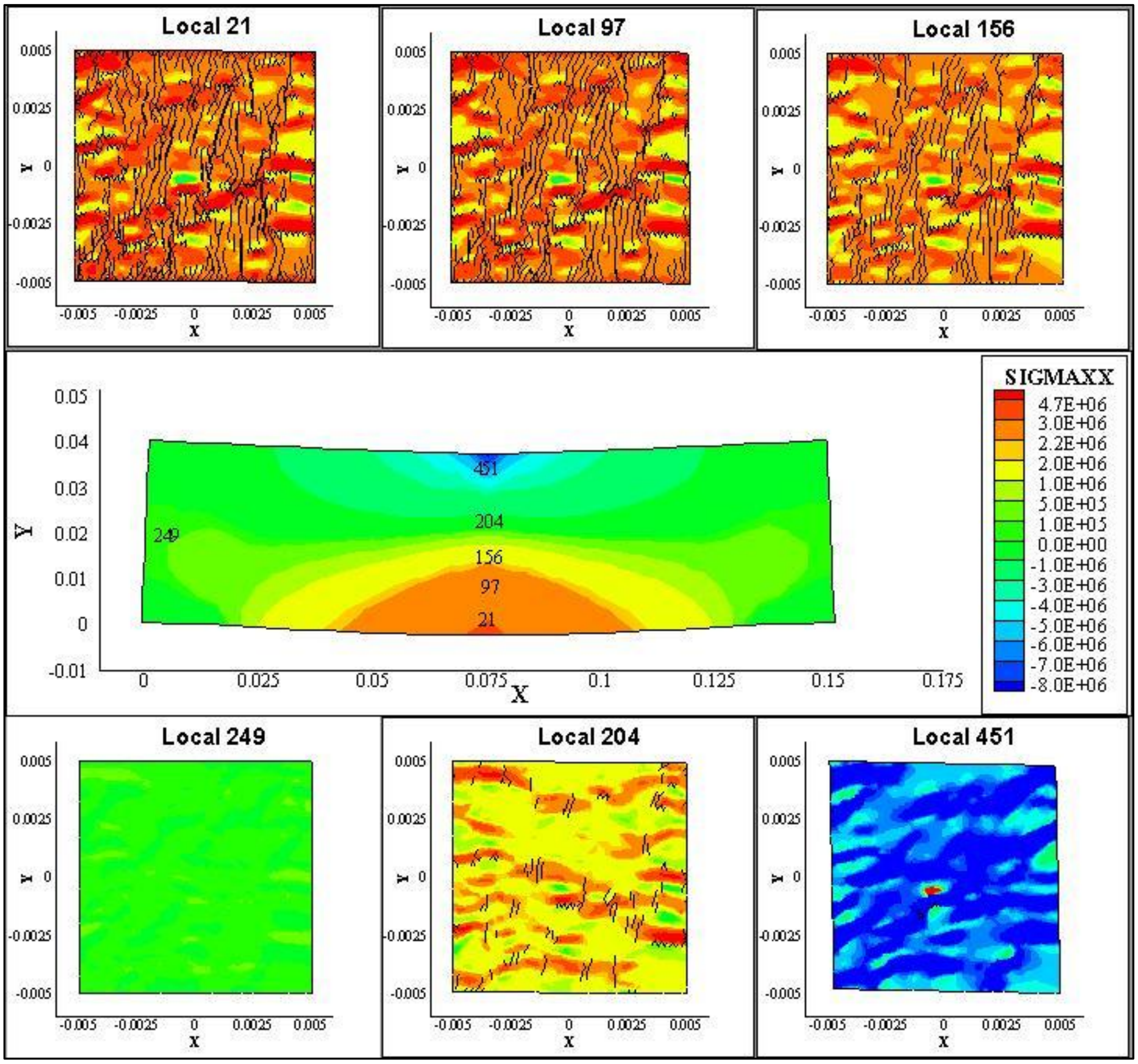

Figure 60: Multiscale simulation with damage-induced - Snapshot at 3.2seconds.

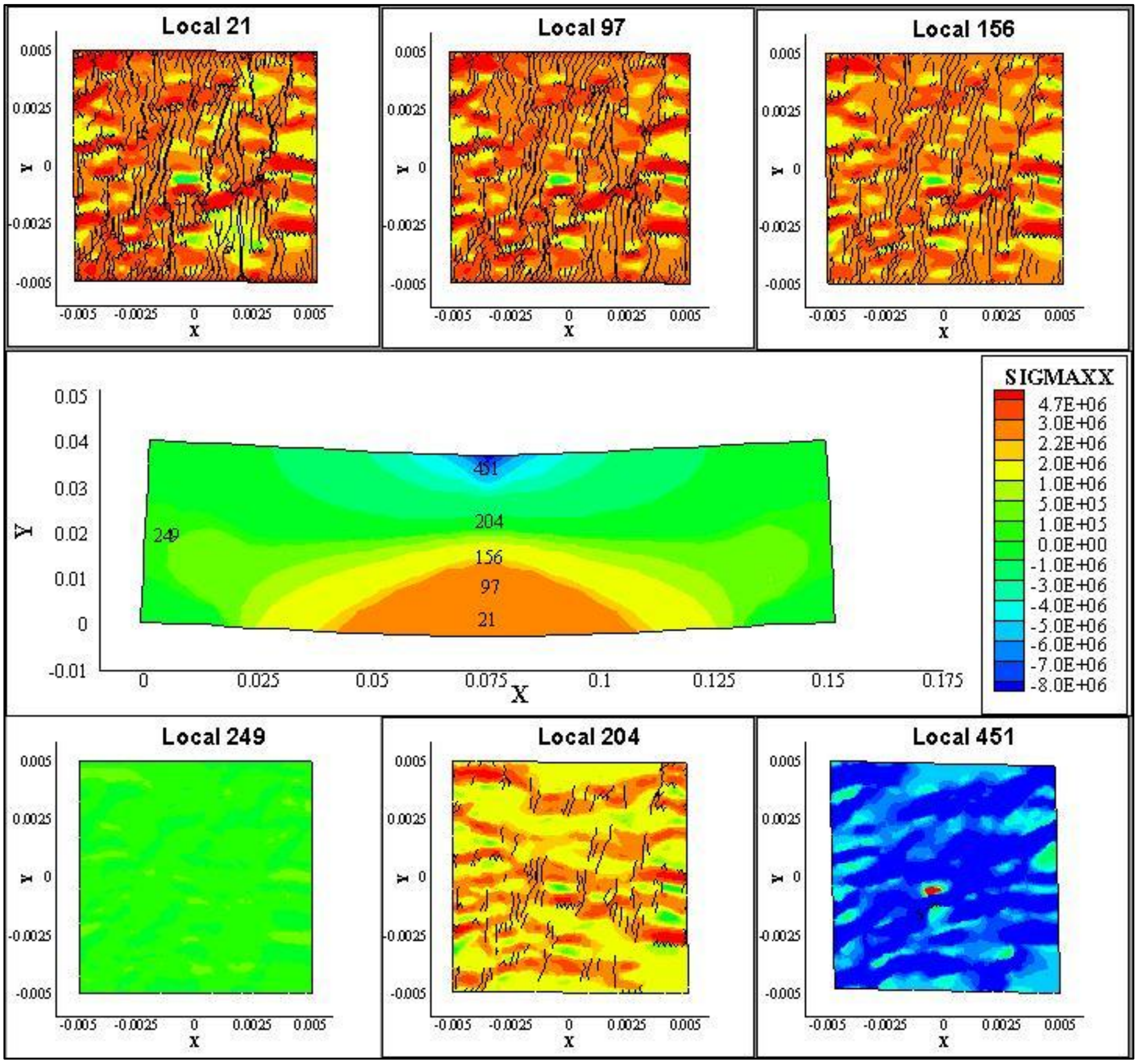

Figure 61: Multiscale simulation with damage-induced - Snapshot at 3.63 seconds.

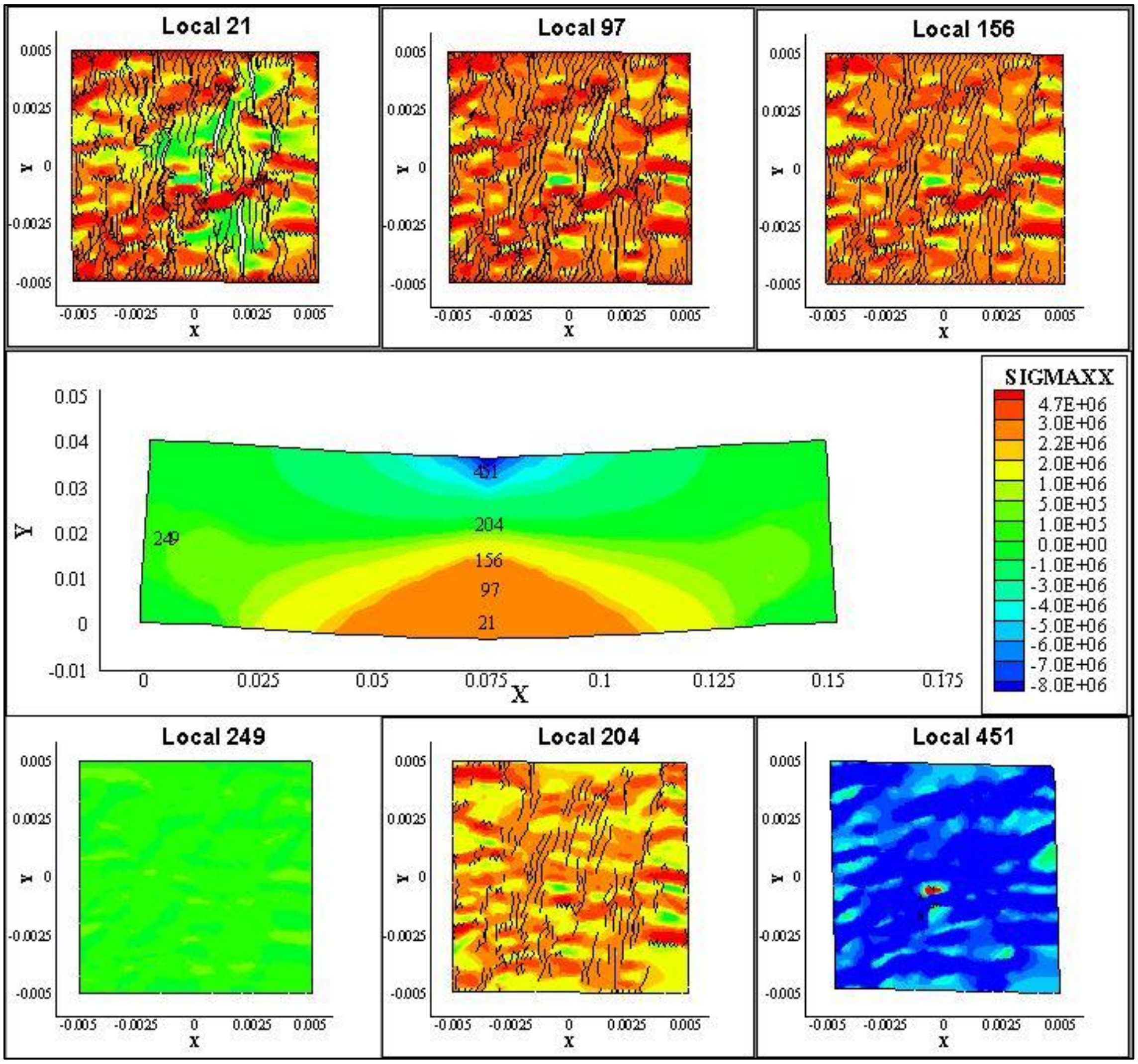

Figure 62: Multiscale simulation with damage-induced - Snapshot at 4.2 seconds.

Initially, at 0.3 seconds (Figure 58), the first cohesive zone elements (represented by the black lines in the local scale figures) were inserted in the Local-21, the microstructure linked to the global element that experiences higher strains. Also, some compressive stresses are developed at Local-451, the microstructure linked to the global element located in the region where the load was applied.

At 0.8 seconds (Figure 59), the number of cohesive zone elements became more significant at Local-21. Furthermore, the damage at this time propagated to other global elements, as shown in the Local-97 snapshot.

Then, at 3.2 second (Figure 60), the level of damage in the microstructure linked to the global elements from the region of higher stresses was notably pronounced and cohesive elements began to connect to each other, indicating possible formation of microcracks. In the case of the Local-249, which was far away from the loading zone, no significant damage was involved in the microstructure, as can be seen from the figure.

At 3.63 seconds (Figure 61), new surfaces were created (due to microcracks) which caused the stress concentration at the local microstructures to vanish, as visualized in Local-21. It is important to mention that statistical inhomogeneity could be introduced by the formation of cracks because they produce discontinuities in the field variables (Souza, 2009). At this point, the precision of the model starts to decrease.

At 4.2 seconds (Figure 62), a macrocrack was formed. Once the localization phenomena occurred (macrocrack formation), statistical homogeneity at the local scale and the subsequent accuracy of the model could no longer be guaranteed. From the computational point of view, simulations can be still performed after localization, and the user should decide to continue or stop the simulation. However, the user should be aware that, even though the physical trend can be still observed, the numerical results may be inaccurate (Souza, 2009). A recent study (Souza and Allen, 2011) has improved the multiscale model used herein to account for the transition of a cloud of microcracks into a macro-crack in the global scale finite element mesh, using advanced techniques such as the eXtended Finite Element Method (X-FEM). However, this is beyond the scope of the present study.

Figure 63 shows the elemental longitudinal stresses of the deformed global structures for the cases with and without damage induced by cracks.

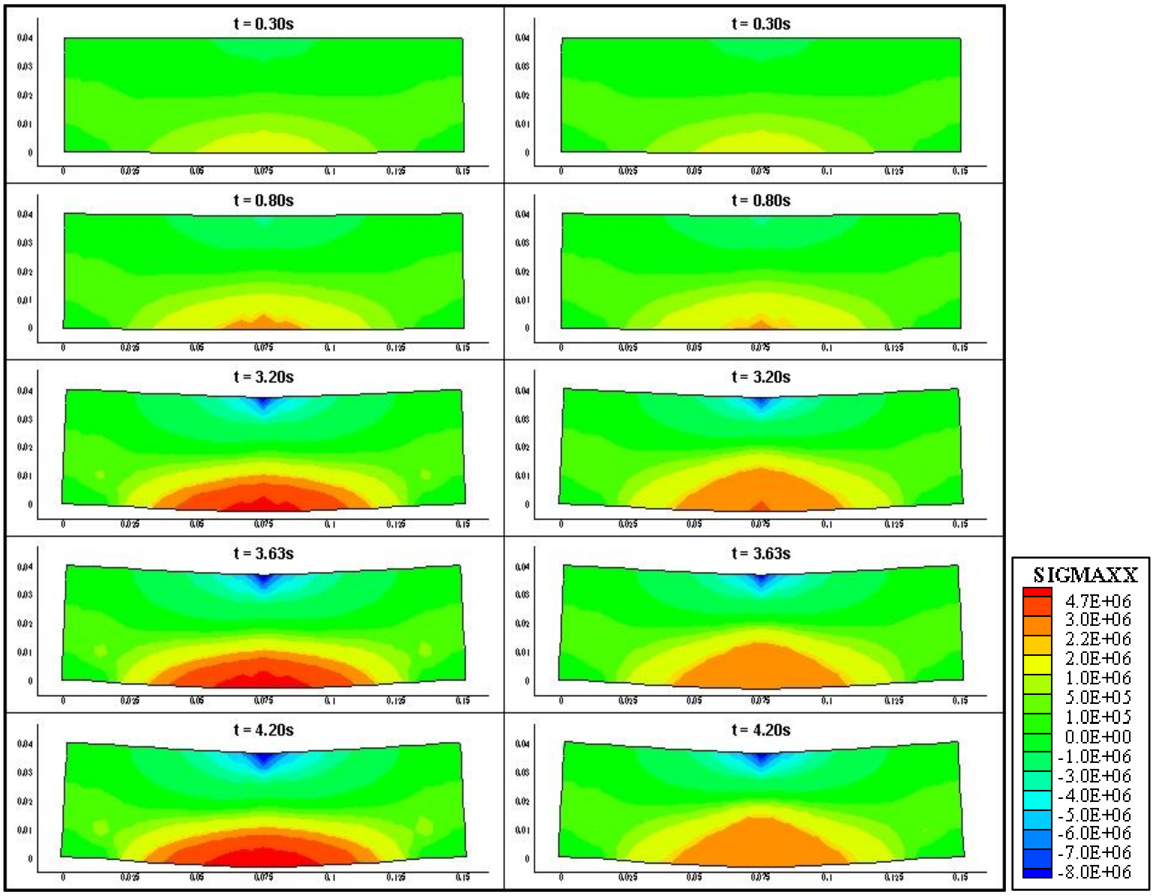

Figure 63: Deformed global beam structures at selected loading times without cracks (left side) and with cracks (right side).

A significant conclusion could be drawn based on the deformed meshes shown in Figure 63. That is, as cohesive zone elements (which eventually became cracks) evolved the stress concentrations on the center of the beam decreased as a result of stiffness degradation. Since the global stiffness was updated for every solution step at each global element, as cracks were initiated and grown in the microstructures, damage-induced anisotropy in the bituminous composite was more pronounced. Therefore, the stiffness update is an important characteristic of two-way coupled multiscale model. Figure 64 and Figure 65 show the overall global scale homogenized tangent constitutive tensor history, C_{ijkl}, obtained by averaging the tangent constitutive tensor of all global elements.

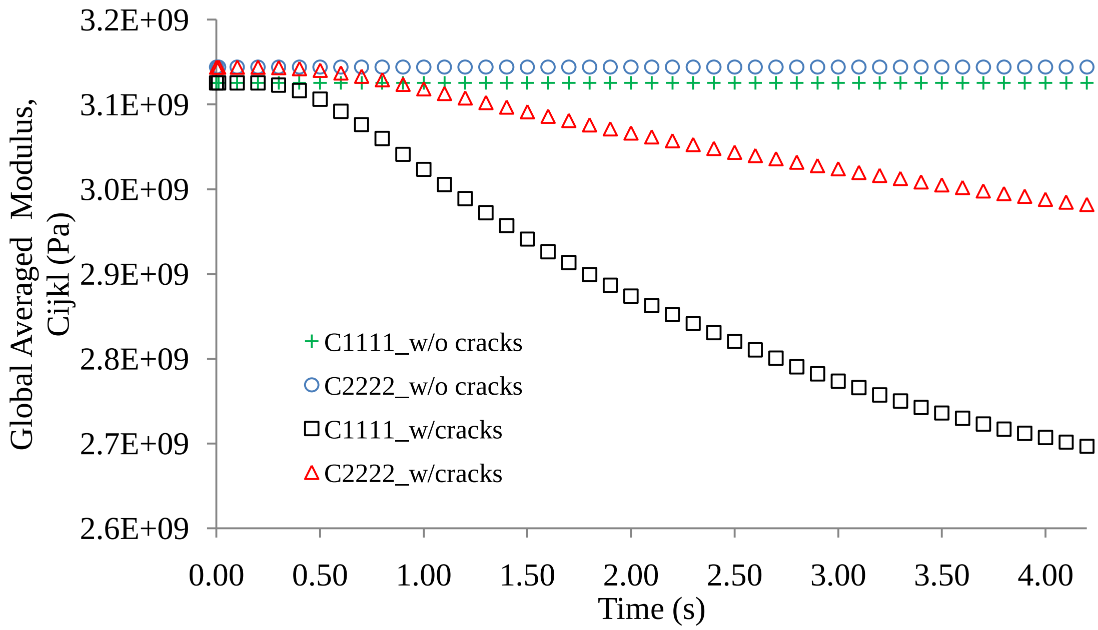

Figure 64: Beam averaged global components $\boldsymbol{C}_{1111}$ and $\boldsymbol{C}_{2222}$ of homogenized constitutive tensor as a function of time.

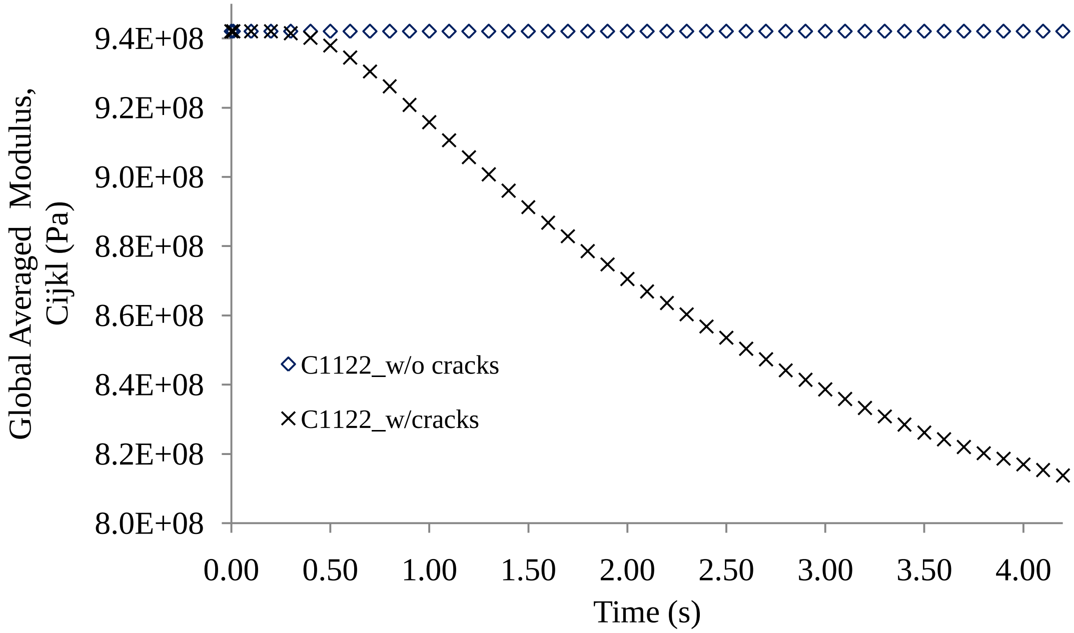

Figure 65: Beam averaged global components $\boldsymbol{C_{1122}}$ of homogenized constitutive tensor as a function of time.

As seen in Figure 64 and Figure 65, the total stiffness of the global beam was reduced. The values of C_{1111}, C_{2222}, and C_{1122}, decreased by 13.7%, 5.2%, and 13.6%, respectively, from their original value at the final captured loading time.

The loss of stiffness at different spatial coordinates along the beam could also be observed. For that, the longitudinal stiffness modulus was plotted as a function of the x coordinate at the bottom of the beam (y=0m), as shown in (Figure 66), and as a function of the y coordinate at the center of the beam (x=0.075m), as shown in Figure 67.

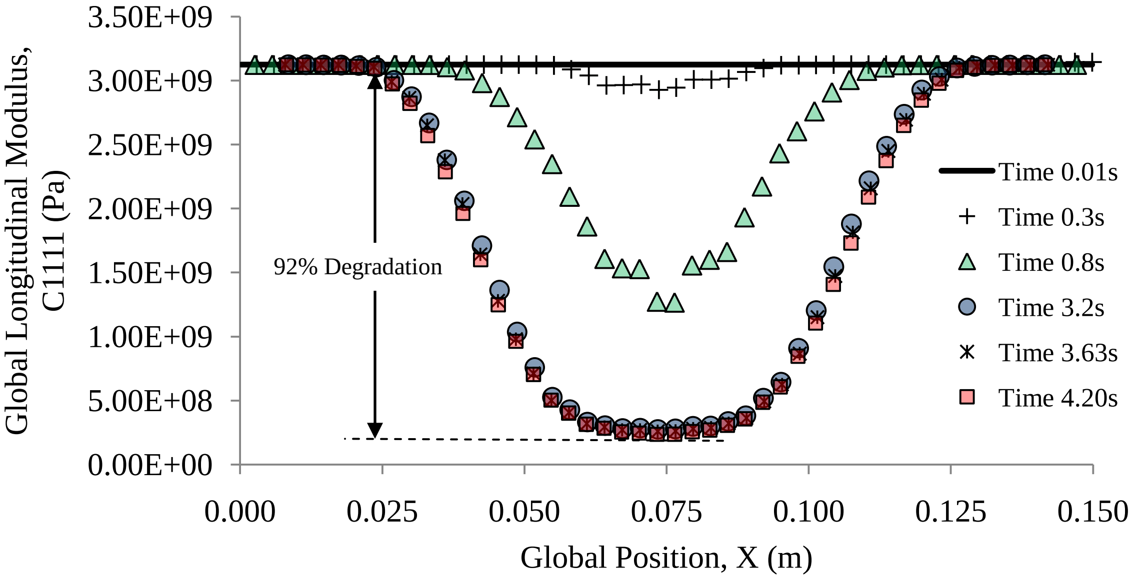

Figure 66: Global longitudinal modulus degradation (due to cracks) at the bottom of the beam as a function of the x position.

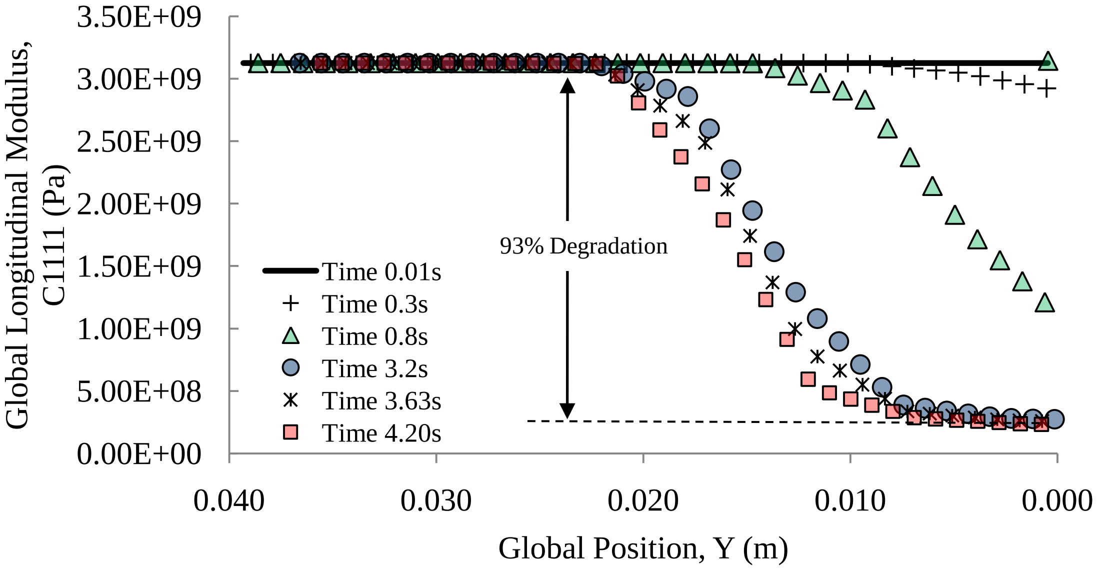

Figure 67: Global longitudinal modulus degradation (due to cracks) at the center of the beam as a function of the y position.

As illustrated in the figures, the longitudinal stiffness modulus (C_{1111}) was drastically reduced at the center of the beam, where it was subjected to higher longitudinal stresses. Clearly, the amount of accumulated damage at the local microstructures affected the global structure performance.

Figure 68 compares the longitudinal stresses in the simulations with and without damage for the local microstructure linked to the global element 21.

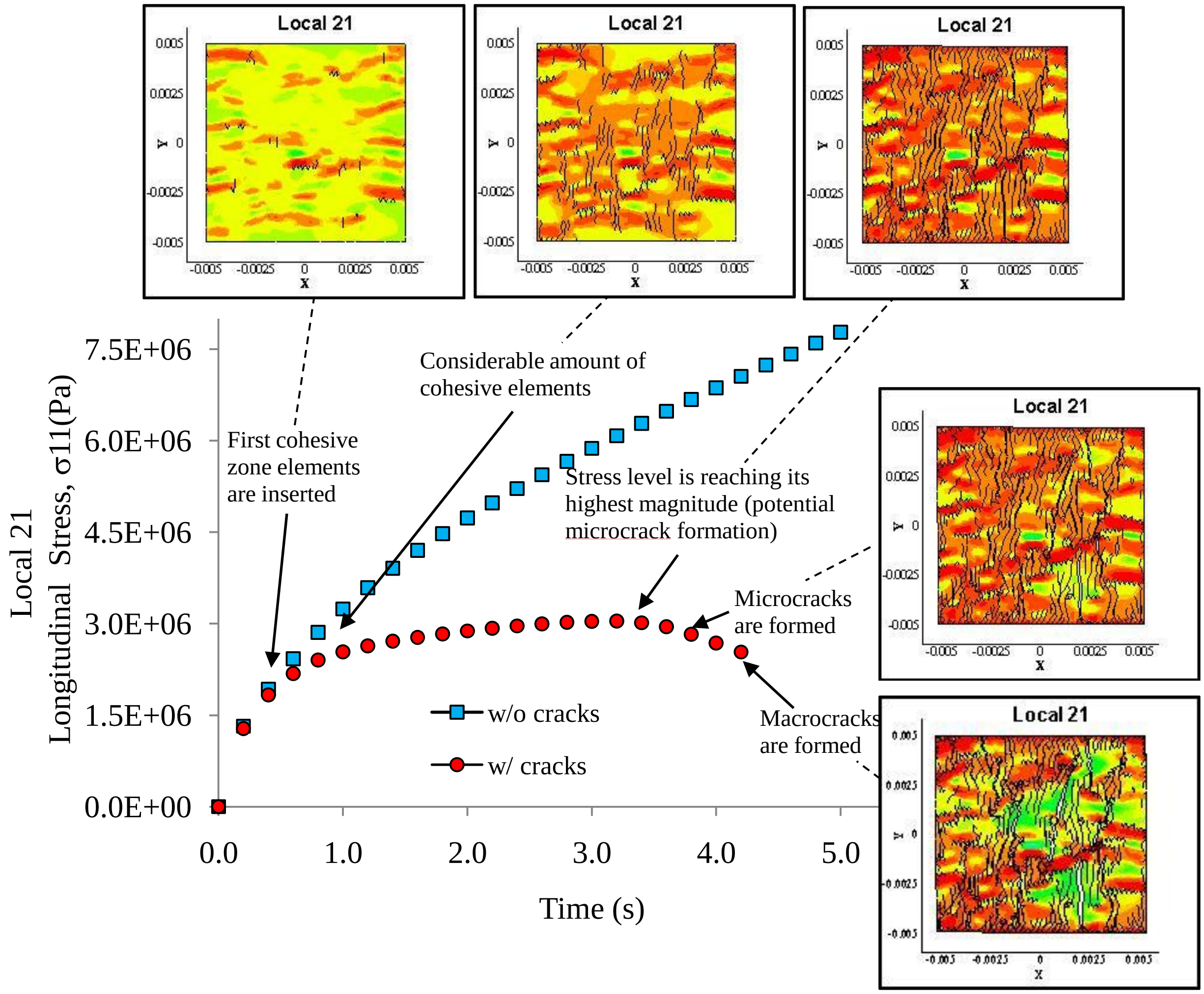

Figure 68: Longitudinal stresses for the local structure linked to the global element no. 21.

Key stages related to formation and propagation of cracks during the loading period were evaluated using the two-way coupled multiscale technique, as presented in Figure 68. The insertion of cohesive zone elements, which was eventually converted to a crack, reduced the stresses on the sample compared to the case with no damage. With the unique model capability to visualize the smaller length scales, crack evolution could be analyzed in a more detail manner, leading to better predictions of failure of the bituminous composites.

6.3.3. Calibration of Rectangular Beam Bending Test with Damage

From the model validation, valuable information could be obtained regarding the physical phenomena occurring in the bituminous sample subjected to bending. The model was able to capture different local scale responses depending on the spatial position of the microstructure, and key stages during the loading time could be identified. However, the numerical results did not match very well with the experimental data after 1.5 seconds, when the reaction force obtained experimentally started to gradually decrease due to significant damage. Therefore, a calibration of the parameters associated to damage was required to obtain better predictions of the overall composite response.

In the phenomenological damage law (Equation 3.18) used herein, the two parameters associated with the damage evolution function were A and m. Since the damage parameter m significantly changes the damage evolution rate, its value was reduced in 72%, resulting in a faster degradation of the composite. All other material characteristics were kept the same as the ones used in the validation showed in Figure 57. The calibration results are shown in Figure 69 along with numerical results without cracks and experimental results.

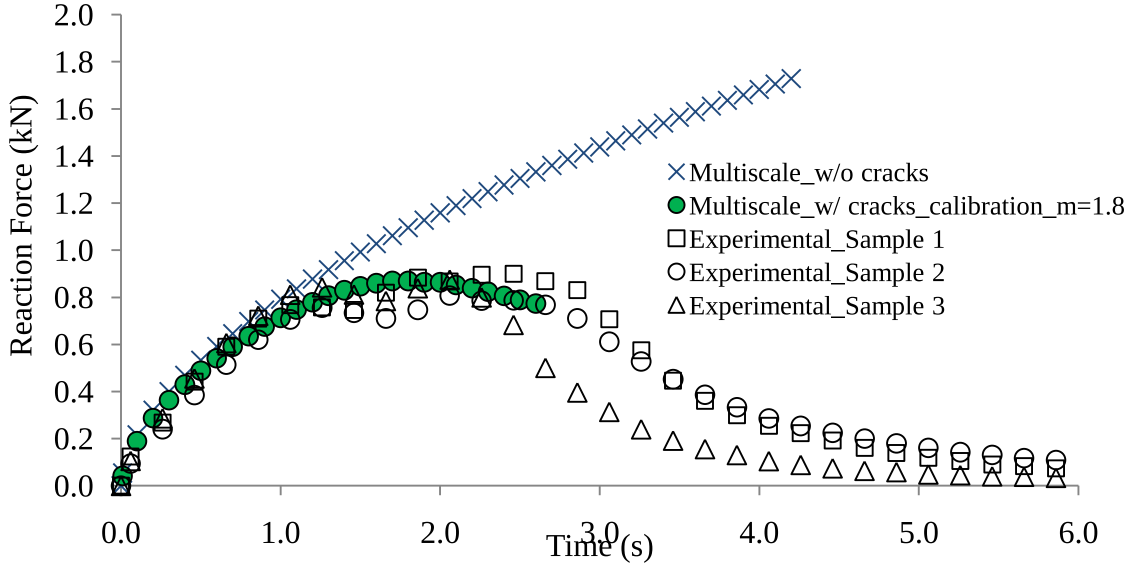

Figure 69: Calibration results for numerical simulation with cracks.

As seen in Figure 69, by increasing the rate of damage propagation, the numerical results obtained using the two-way coupled multiscale showed a better prediction of the damage-dependent behavior of the bituminous composite specimen used herein. The deformed mesh and elemental stress at both global and local scale structures at 2 seconds (peak load) and 2.5 seconds (after peak dropping point) can be visualized in Figure 70 and Figure 71.

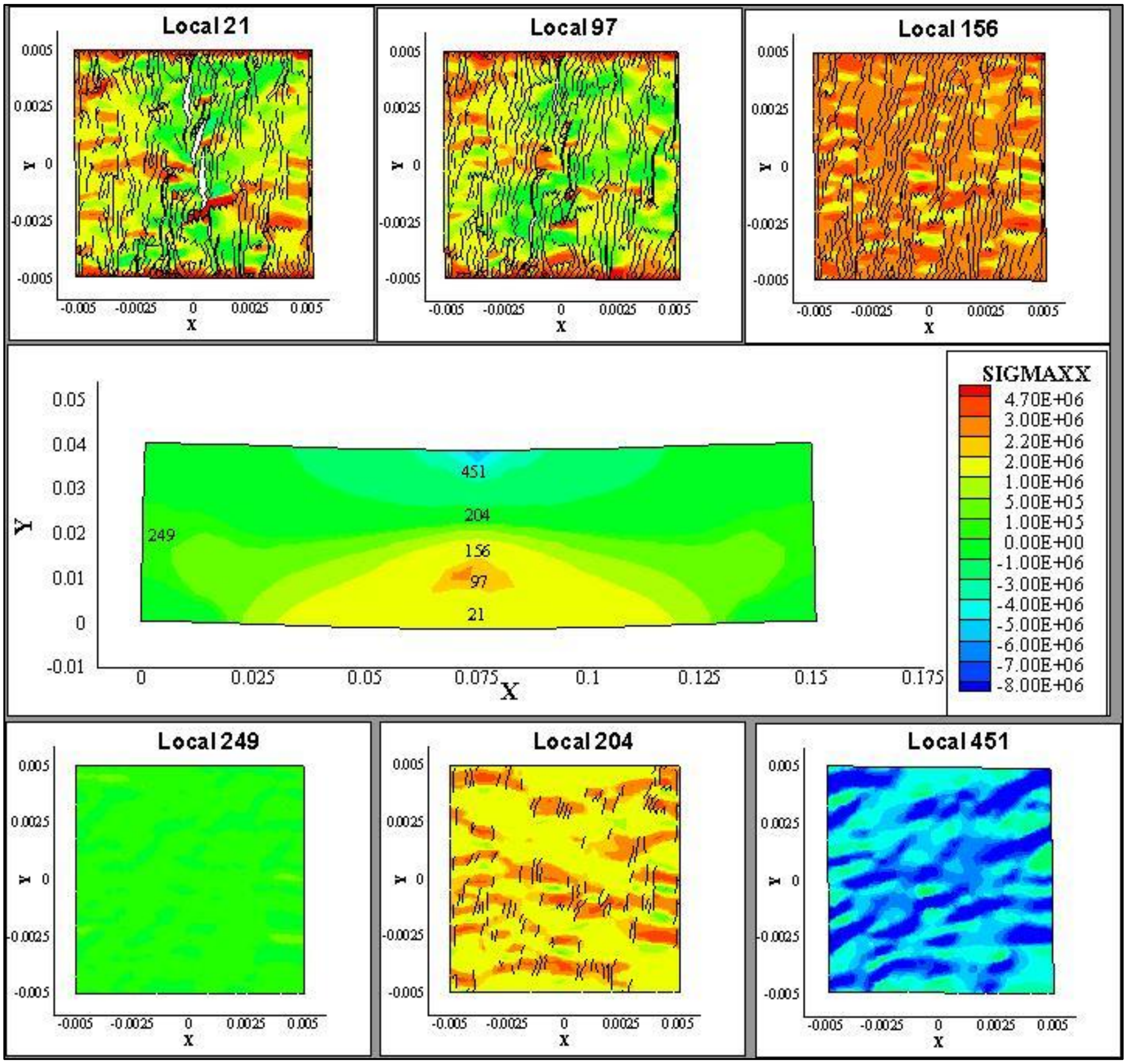

Figure 70: Multiscale calibration results with damage-induced - Snapshot at 2 seconds.

From the snapshots, it can be noticed by the stresses contours that microcracks are formed at 2 seconds at Local-21 (cohesive zone tractions vanish, as shown by the zero stress green contours zones).

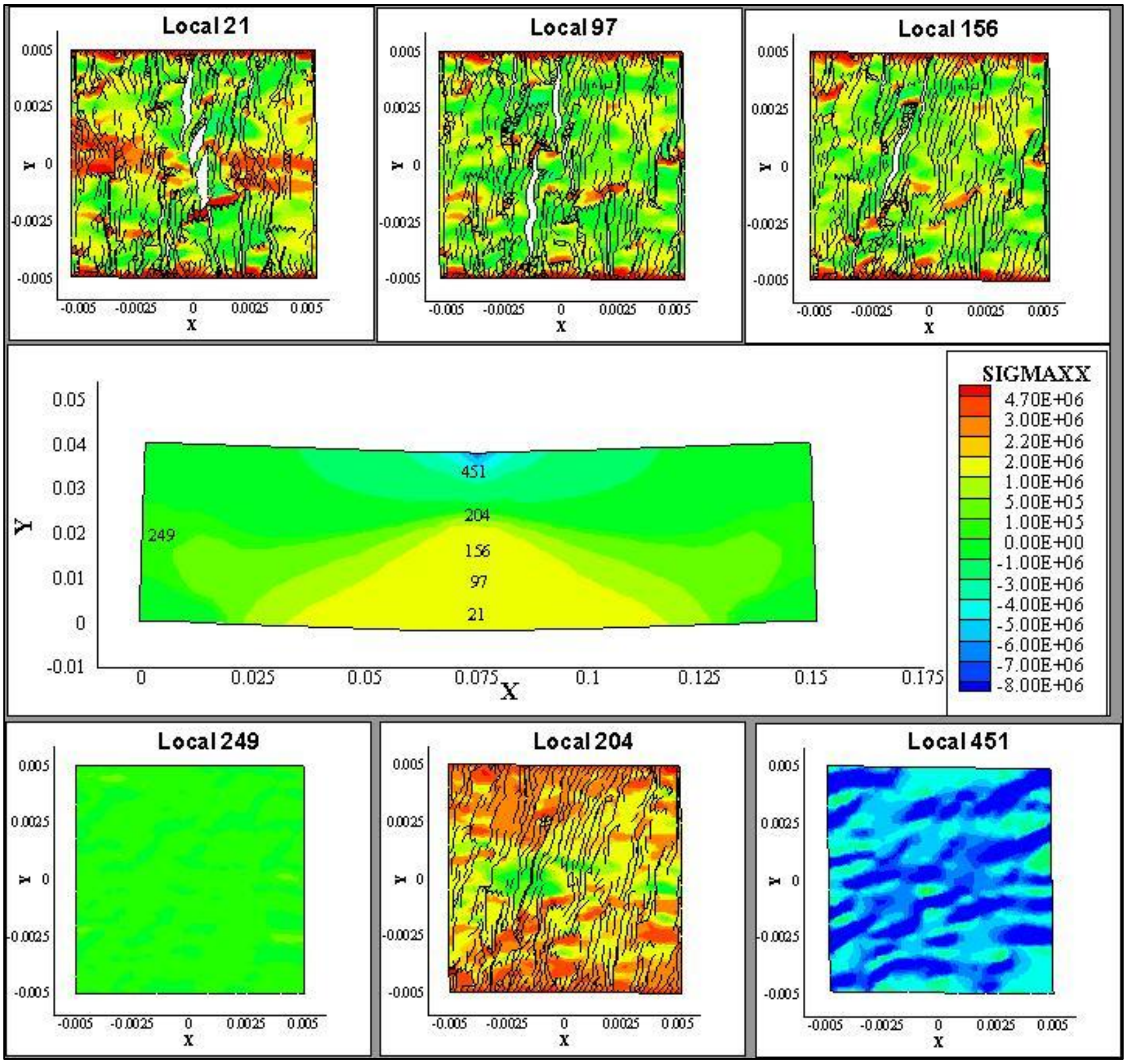

Figure 71: Multiscale calibration results with damage-induced - Snapshot at 2.5 seconds.

At 2.5 seconds, the bearing capacity of the global elements located at the center region is almost gone, and macrocracks are visible in the contour plots. After that point, the accuracy of the model is not guaranteed anymore and, therefore, the simulation was manually aborted.

Chapter 7

Parametric Analysis of the Model

The bituminous composite mix design process involved the selection of proper material sources and combinations. A wide range of parameters, such as material properties, volume fraction, and/or particle gradation, can be varied to study the impact of those changes on the overall composite performance. Different from continuum damage models, the use of a micromechanical model allows us to change important design variables without the need to perform new sets of experiments. To demonstrate that, this chapter details the parametric analysis of the two-way coupled multiscale model that was previously proposed.

To keep the same local RVE structure that was determined in the previous chapters, no changes were made regarding the RVE geometric constitution (the volume fraction, the particle size distribution and orientation). Thus, the bituminous composite material properties were selected for the parametric analysis. Because damage in bituminous composites initiates within the matrix phase, a parametric analysis of the material properties associated with this phase was performed by varying the magnitude of the linear viscoelastic properties and the cohesive zone parameters. To reduce the computational time required to solve this problem, only 30 elements were selected to be multiscaled, as shown in Figure 72.

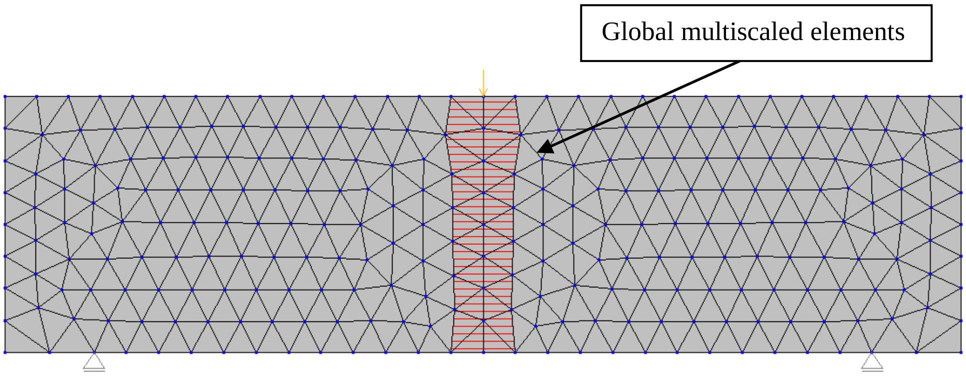

Figure 72: Rectangular beam highlighting the multiscaled element for parametric analysis.

Before changing the material properties, the bending beam problem (with 30 global elements multiscaled) was simulated using the properties obtained in the laboratory. This simulation was performed with two main purposes, i.e., i) to examine the efficiency of the model when not all elements were multiscaled, and ii) to serve as a reference case for comparisons with other simulations that varied the material properties.

Figure 73 presents the numerical results for simulations with all elements multiscaled and with only 30 selected global elements multiscaled. Also, experimental results were plotted for further discussions.

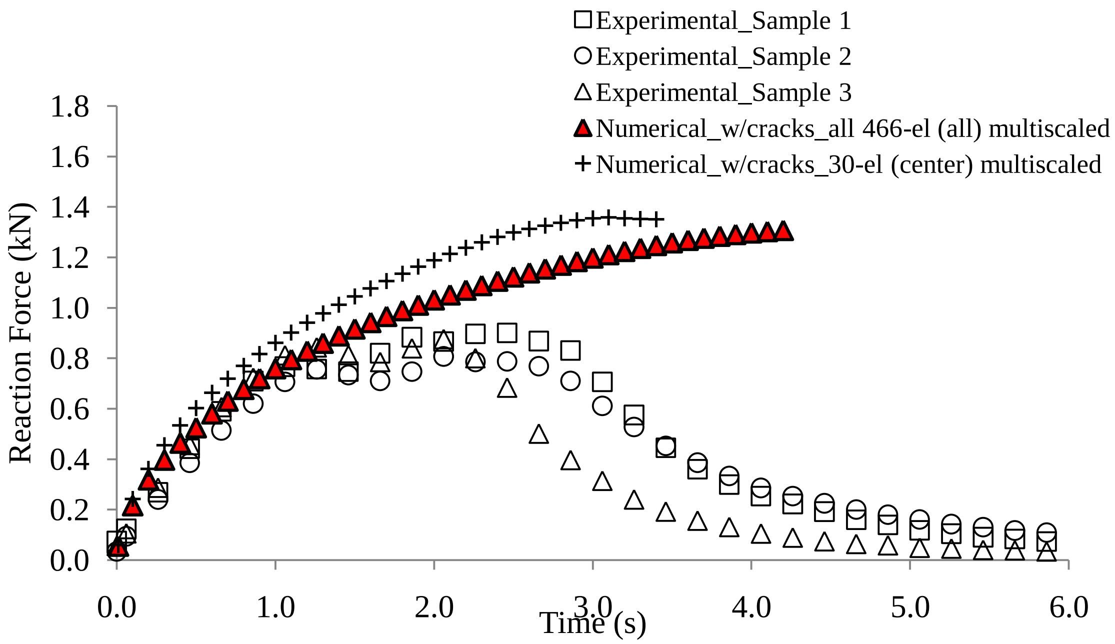

Figure 73: Simulation results varying the number of multiscaled elements and comparison to experimental results from bending beam test results.

As seen in Figure 73, the simulation accuracy decreased as the total number of multiscaled elements was reduced, and the specimen became more resistant to damage This is obvious because the less number of global scale elements involved in the multiscale modeling implies less consideration of overall damage process occurring in the specimen.

On the other hand, the computational time required to solve the problem multiscaling all global elements was about 360 hours, while the same problem multiscaling 30 elements took 72 hours in Dell workstation using eight Intel Xeon processors at 3.00 GHz running under Linux Fedora 10. Clearly, the number of multiscaled elements affected not only the accuracy of the model by also the computational efficiency. Thus, the user should carefully decide the elements to be multiscaled in order to optimize the accuracy/efficiency relation. The amount of computational power utilized in this study may be considered impractical, but it is important to note that the computer resource available at the time of this research was very limited. The computation time can be drastically decreased if one uses powerful supercomputers which have in general more than hundred processors.

Now, to study the effect of material properties on the overall composite performance, three cases were simulated and compared: 1) PA-1, the reference case, in which the material properties were kept the same as the ones used for model validation; 2) PA-2, to observe the effect the stiffness change, in which the linear-viscoelastic matrix properties were reduced by 50%, and 3) PA-3, to see the rate of damage propagation effect on the composite response by reducing the damage parameter m in 80%. Figure 74 shows a comparison of numerical results using original and changed material properties.

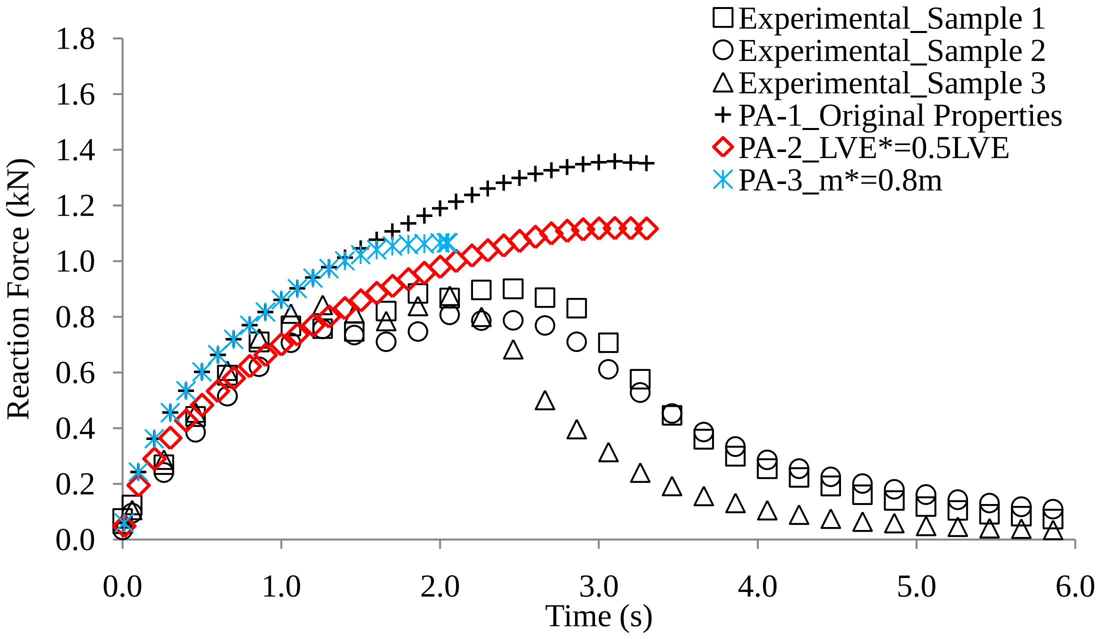

Figure 74: Parametric analysis results.

From Figure 74, it can be noticed that the lower stiffness of the matrix phase affected the overall stiffness of the bituminous composite. When the viscoelastic properties of the matrix were reduced by 50% from its original value, the overall composite stiffness was reduced, which was evidenced by the initial slope change in the force *versus* time curve. Regarding damage propagation, the rate of crack growth in the microstructure was increased when the parameter *m* was reduced, resulting in a faster degradation of the specimen compared to the reference case. Figure 75 shows the longitudinal stresses for the Local-21 microstructure.

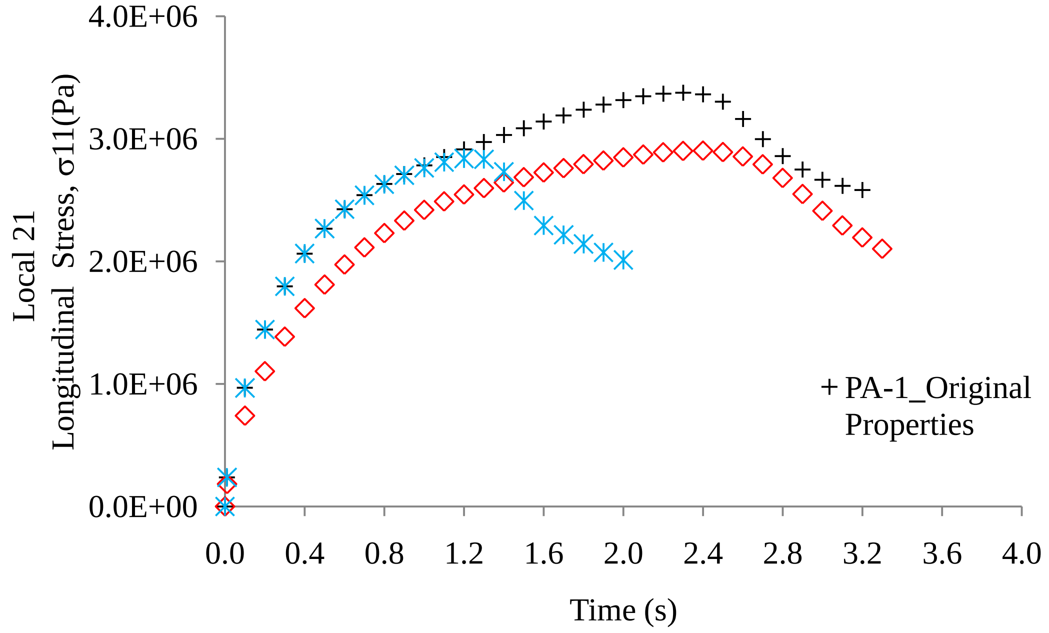

Figure 75: Local scale parametric for the local structure linked to the global element no. 21.

As seen in Figure 75, the overall microstructure stiffness was reduced by decreasing the linear-viscoelastic matrix properties. With that, the maximum stresses supported by the microstructure were also reduced. As mentioned before, the change in the damage parameter *m* affected the microstructure response. By reducing the magnitude of this parameter in 80%, the damage evolved faster compared to the one observed in the reference case.

For a better visualization of the physical phenomena described above, the deformed configuration of the global beam and the selected microstructure are shown at two selected loading times (Figure 76 and Figure 77). The contour plots represent the longitudinal stress responses in the composite.

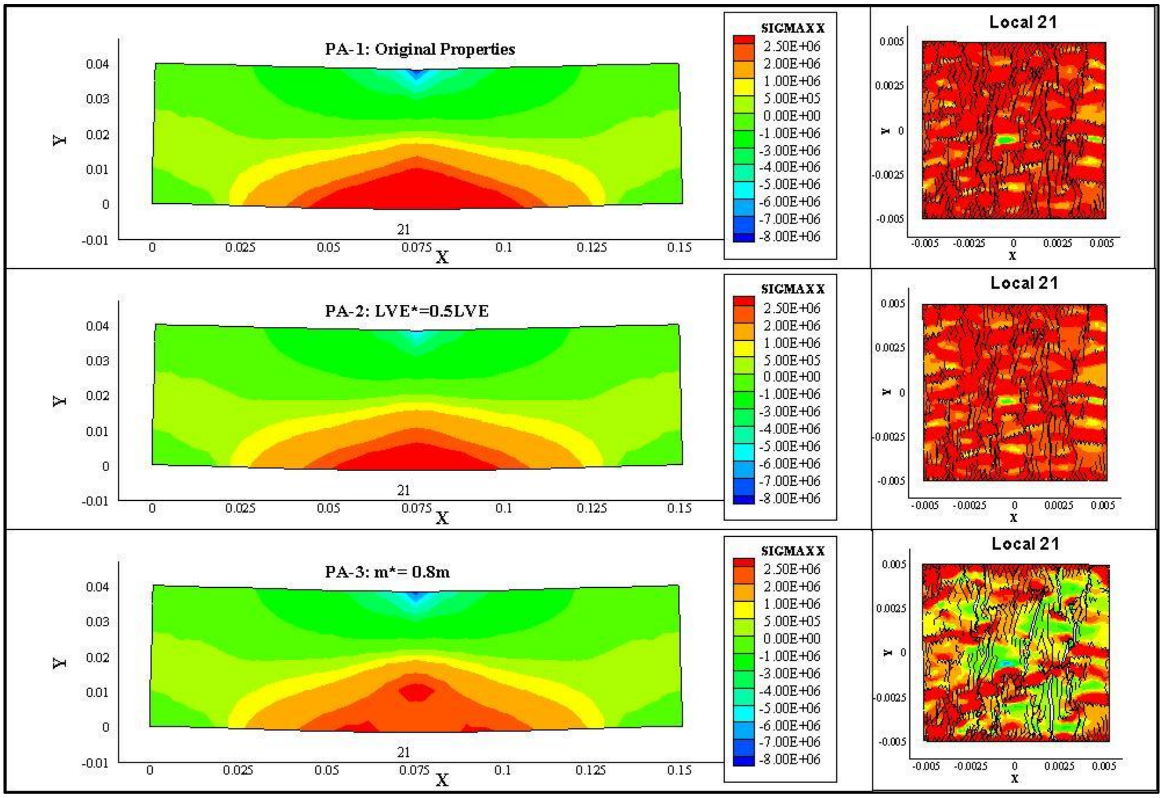

Figure 76: Parametric analysis snapshots at 2.0 seconds.

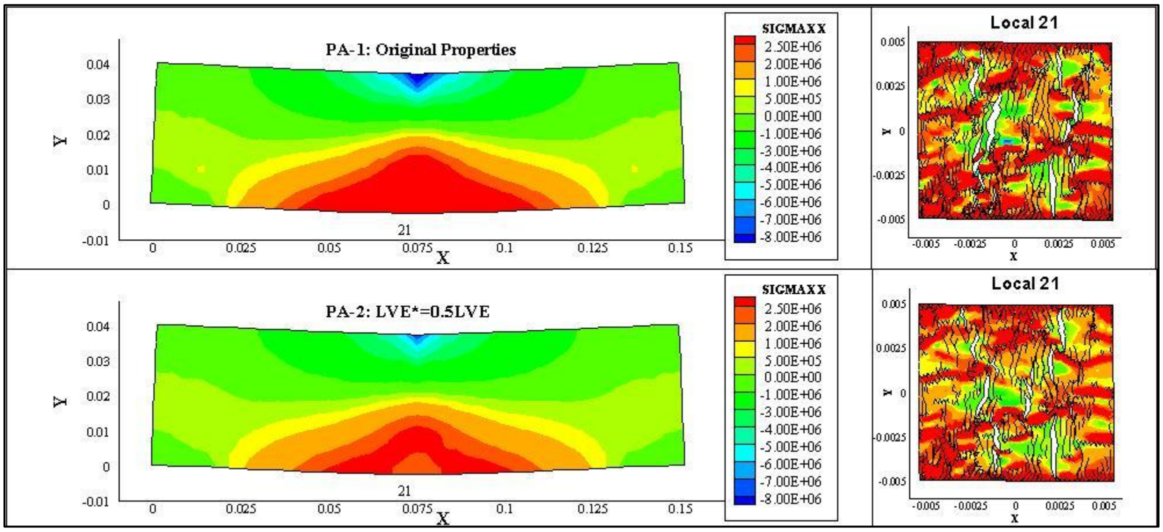

Figure 77: Parametric analysis snapshots at 3.3 seconds.

The beauty of the two-way coupled multiscale modeling is demonstrated herein, where one could verify the effect of component material properties on the overall composite performance without the need to perform new sets of time-consuming and costly experimental tests. That said, the two-way coupled multiscale model can allow engineers to better understand the mechanical effects of material-specific design variables on the overall damage-related responses and performance characteristics of structures.

Moreover, once the RVE has been determined for a particular bituminous mixture, it can be used to model a wide range of testing experiments, such as bending beam tests, indirect tension tests, fatigue tests, and even for pavement modeling. So, one could even generate a data basis with RVE for mixtures that are commonly used in practice, so engineers can design their mixtures without the need to perform experiments on the local scale constituents, and drastically reducing the number of tests to evaluate the performance of the mixture.

That said, the better understanding of small-scale design variables can help engineers to select mixture constituents in a more appropriate way and advance the current volumetric mix-design concepts, materials models, and performance models.

Chapter 8

Concluding Remarks

A two-way coupled multiscale computational model for predicting the damage-dependent mechanical behavior of bituminous composites was presented. The model accountted for composite heterogeneities, inelasticity, and anisotropic damage accumulation in the small scale on the overall performance of larger scale structures by taking into account individual mixture constituents through the unique scale-linking technique: a local scale in the form of the heterogeneous RVE and a global scale that was homogenized from the local scale responses. The model was implemented using the finite element formulation, to properly handle the geometric complexities and material inelasticity without a significant loss in accuracy.

- The non-linear rate dependent fracture behavior of bituminous composites was considered by employing a micromechanically based non-linear rate-dependent viscoelastic damage model.

- The model was verified by solving problems with closed-form solutions, and numerical results were compared with analytical results. In addition, comparing to single scale computational modeling of heterogeneous objects, the multiscale model demonstrated much higher computational efficiency by reducing simulation time based on the homogenization process to link scales which highlight the benefit of multiscale modeling approach.

- Unique consideration was taken to determine the representative volume element (RVE). Important geometrical variables were considered in the analysis throughout the use of image analysis techniques. Constitutive properties were also evaluated for different trial RVE's sizes by performing finite element simulations of the relaxation modulus.

- To validate the model, bending tests were simulated. The evolution of microcrack was evaluated by analyzing the local scale microstructure response. As a consequence, the model was capable of considering damage-induced anisotropy due to the distribution and orientation of cracks.

- To the end, a parametric study was carried out to verify the impact of the material properties on the overall composite performance. It is expected that a successfully developed multiscale computational model, such as the one presented herein, can be an efficient analysis-design-prediction tool for various types of mixtures and structures including bituminous mixtures targeted in this study.

8.1. Significance and Impacts of the this Study

The use of multiscale technique can be a significant tool to predict bituminous composites damage-dependent behavior, taking into account the material characteristics in different length scales. The model can account for essential characteristics of bituminous composites such as nonlinear inelastic constitutive behavior, mixture heterogeneity, material anisotropy and multiscale damage development. Significant benefits and potential impact of this study can be listed as follows:

- Since the multiscale model is based on micromechanics concepts, mechanical effects of bituminous composite constituents (volume fraction of matrix, aggregate particle distribution, binder properties, etc) can be evaluated. Thus, with clear assessment of those variables, pavement engineers and practitioners can make better decisions regarding materials' selection and mixture constituents' proportions;

- The use of multiscale technique gives a significant reduction in computational effort compared to single scale models, where a high level of refinement is required to account for the explicit heterogeneities, resulting in costly simulations.

- Using the unique two-scale coupled technique, small scale phenomena can be carefully assessed, and, therefore, damage associated responses of bulk composites can be predicted in a more detailed way;

- The clear understanding of the small scale phenomena will then be guidelines to select composite constituents in a more appropriate way and to improve current asphalt mixture design methodology so that better-performing and longer-lasting roadway mixtures can be produced;

- Since only small scale material properties are required in the model, this approach can reduce the amount of laboratory testing required, thereby providing substantial additional cost savings;
- Even though the multiscale model was applied herein for prediction of damage-dependent behavior of bituminous materials, it can be applied for other types of composite media, such as portland cement concrete mixtures, geologic media, and other complex structures by simply incorporating appropriate constitutive and damage functions into the model.

8.2. Future Research Work

Future research work includes:

- Validate the model for other types of laboratory test conditions as well as for other type of composite media;
- Consider cracks at the global length scale using the new developments in the *MULTIMECH* code based on eXtended Finite Element (XFEM)
- Verify and calibrate the model for problems in three dimensions;
- Perform a RVE study in three dimensions;
- Perform a rigorous study to determine fracture properties based on experimental observations of fracture tests;
- Verify the proposed methodology to determine fracture parameters using other types of mixture combinations and loading conditions;

References

1. AASHTO (2009), “Rough Roads Ahead, Fix Them Now or Pay for It Later”. A joint product of American Association of State Highway and Transportation Officials, and TRIP-a National Transportation Research Group.

2. Allen, D. H. (2001) “Homogenization principles and their application to continuum damage mechanics”. *Composites Science and Technology,* Vol. 61(15), pp. 2223–2230.

3. Allen, D. H. and Searcy, C. R. (2001) “A Micromechanical Model for a Viscoelastic Cohesive Zone”. *International Journal of Fracture*, Vol. 107, pp. 159-176.

4. Aragão, F. T. S., Kim, Y. R., Karki, P., and Little, D. N. (2010) “Semiempirical, Analytical, and Computational Predictions of Dynamic Modulus of Asphalt Concrete Mixtures”. *Transportation Research Board,* Vol. 2181 (3), pp. 19-27.

5. Aragão, F. T. S., and Kim, Y. R. (2010) “Characterization of Fracture Properties of Asphalt Mixtures Based on Cohesive Zone Modeling and Digital Image Correlation Technique”. *Transportation Research Board* CD-ROOM.

6. ASTM D-3497 (2003). “Standard Test Method for Dynamic Modulus of Asphalt Mixtures.” ASTM International, West Conshohocken, PA.

7. Ban, H., Im, S., and Kim, Y. R. (2011). “Characterization of Fracture Properties of Asphalt Mixture under Mixed-Mode Loading Configuration”. Unpublished manuscript.

8. Barksdale, R. D. (1993). *The Aggregate Handbook,* National Stone Association, Washington, D. C.

9. Barenblatt, G. I. (1962) “The Mathematical Theory of Equilibrium Cracks in Brittle Fracture”. *Advances in Applied Mechanics,* Vol. 7, pp. 55-129.

10. Birgisson, B., Montepara, A., Romeo, E., Roque, R., Roncellla, R., and Tebaldi, G. (2007). “Determination of Fundamental Tensile Failure Limits of Mixtures.” *Journal of the Association of Asphalt Paving Technologists*, 76, pp. 303-344.

11. Camacho, G. T. and Ortiz, M. (1996) “Computational Modeling of Impact Damage in Brittle Materials”. *International Journal of Solid Structures*, Vol. 33, No. 20-22, pp. 2899-2938.

12. Chehab, G. R., O’Quinn, E., and Kim, Y. R. (2000) “Specimen Geometry Study for Direct Tension Test Based on Mechanical Tests and Air Void Variation in Asphalt Concrete Speciemens Compacted by Superpave Gyratory Compactor.” *Transportation Research Record*, 1723, pp. 125-132.

13. Chehab, G., Kim, Y. R., Schapery, R. A., Witczak, M. W., and Bonaquist, R. (2003) “Characterization of Asphalt Concrete in Uniaxial Tension Using a

Viscoelastoplastic Continuum Damage Model." *Journal of the Association of Asphalt Paving Technologists*, Vol. 72, pp. 315-355.

14. Christensen, R. M. (1979). "Mechanics of Composite Materials". Wiley, New York.

15. Christensen, R. M. (1982) "Theory of viscoelasticity: An introduction". Academic, New York.

16. Christensen, D. W. (2002). NCHRP Project 9-25, Quarterly Report to the National Cooperative Highway Research Program.

17. Chong, K.P. and Kuruppu, M. D. (1984) "New specimen for fracture toughness determination for rock and other materials". *International Journal of Fracture,* Vol. 26, pp. R59–R62.

18. Costanzo, F. and Allen, D. H. (1993) "A Continuum Mechanics Approach to some Problems in Subcritical Crack Propagation". *International Journal of Fracture*, Vol. 63, pp. 27-57.

19. Daniel, J. S. and Kim, Y. R. (2002). "Development of a Simplified Fatigue Test and Analysis Procedure Using a Viscoelastic, Continuum Damage Model." *Journal of the Association of Asphalt Paving Technologists*, Vol. 71, pp. 619-650.

20. Dugdale, D.S. (1960) "Yielding of Steel Sheets Containing Slits". *Journal of Mechanics and Physics of Solids*, Vol. 8, pp. 100-104.

21. Feyel, F., and Chaboche, J. L. (2000) “FE2 Multiscale Approach for Modeling the Elastoviscoplastic Behavior of Long Fibre SiC/Ti Composite Materials”. *Computer Methods in Applied Mechanics and Engineering*, Vol. 183, pp. 309-330.

22. Fish, J., and Wagiman, A. (1993) “Multiscale Finite Element Method for a Lacally Nonperiodic Heterogeneous Medium”. *Computational Mechanics*, Vol. 12, pp. 164-180.

23. Fish, J. and Shek, K. (2000) “Multiscale Analysis of Composite Materials and Structures”. *Composites Science and Technology*, Vol. 60, pp. 2547-2556.

24. Freitas, F. A. C. (2007). “A Theoretical and Experimental Technique to Measure Fracture Properties in Viscoelastic Solids”. Ph.D. Dissertation, University of Nebraska–Lincoln.

25. Gibson, N. H., Schwartz, C. W., Schapery, R. A., and Witczak, M. W. (2003) “Viscoelastic, Viscoplastic, and Damage Modeling of Asphalt Concrete in Unconfined Compression.” *Journal of the Transportation Research Board*, 1860, pp. 3-15.

26. Griffti, A. A. (1920) “The Phenomena of Rupture and flow in Solids”. Philosophical *Transactions of the Royal Society of London*, Series A, Vol. 221, pp. 163-198.

27. Ghosh, S., Lee, K., and Raghavan, P. (2001) “A Multi-level Computational Model for Multiscale Damage Analysis in Composite and Porous Materials”. *International Journal of Solids and Structures*, Vol. 38, pp. 2335-2385.

28. Haj-Ali, R. M., and Muliana, A. H. (2004) “A Multi-scale Constitutive Formulation for the Nonlinear Viscoelastic Analysis of Laminated Composite Materials and Structures”. *International Journal of Solids and Structures*, Vo. 41, pp. 3461-3490.

29. Harvey, J., Guada, I., and Long, F. (2000). “Effects of Material Properties, Specimen Geometry, and Specimen Preparation Variables on Asphalt Concrete Tests for Rutting.” *Journal of the Association of Asphalt Paving Technologists*, 69, pp. 236-280.

30. Hashin, Z. (1983) “Analysis of Composite Materials. A survey.” *Journal of Applied Mechanics*, 50, pp. 481–505.

31. ImageTool: Image Analysis Program. (1997). Department of Dental Diagnostic Science, University of Texas Health Science Center, San Antonio.

32. Kachanov, L. M. (1958) “On the Creep Fracture Time”. *Izv. Acad. Nauk SSSR Otd. Tekhn*. Vol. 8, pp. 26-31.

33. Karki, P. (2010) “Computational and Experimental Characterization of bituminous Composites based on Experimentally Determined Properties of Constituents”. Master Thesis, University of Nebraska–Lincoln.

34. Kim, Y. R., Allen, and D. H., Little, D. (2007) “Computational Constitutive Model for Predicting Nonlinear Viscoelastic Damage and Fracture Failure of Asphalt Concrete Mixtures”. *International Journal of Geomechanics,* pp. 102–110.

35. Kim, Y. R., Allen, D. H., and Little, D. (2005) “Damage-Induced Modeling of Asphalt Mixtures through Computational Micromechanics and Cohesive Zone Fracture”. *Journal of Materials in Civil Engineering*, Vol. 17, No. 5, pp. 477-484.

36. Kim, Y., Lee, J., and Lutif, J. (2010) “Geometrical Evaluation and Experimental Verification to Determine Representative Volume Elements of Heterogeneous Asphalt Mixtures.” *Journal of Testing and Evaluation*, Vol. 38, No. 6.

37. Kim, Y. R., Lutif, J. E. S., Allen, D. H. (2009) “Determining Representative Volume Elements of Asphalt Concrete Mixtures without Damage”. *Journal of the Transportation Research Board*, Vol. 2127, pp. 52-59.

38. Kim, H., Wagoner, M. P., Buttlar, W. G. (2009) “Micromechanical Fracture Modeling of Asphalt Concrete Using a Single-Edge Notched Beam Test”. *Materials and Structures*, Vol. 42 (5), pp. 677-689.

39. Kim, Y. R., and Wen, H. (2002) “Fracture Energy from Indirect Tension Testing.” *Journal of the Association of Asphalt Paving Technologists*, Vol. 71, pp. 779-793.

40. Lee, H. J., Daniel, J. S., and Kim, Y. R. (2000). “Continuum Damage Mechanics-Based Fatigue Model of Asphalt Concrete.” *Journal of Materials in Civil Engineering*, ASCE, Vol. 12(2), pp. 105-112.

41. Lee, H. J. and Kim, Y. R. (1998) “Viscoelastic Continuum Damage Model of Asphalt Concrete with Healing”. *Journal of Engineering Mechanics*, Vol. 124, n.11, pp. 1224-1232.

42. Li, X. and Marasteanu, M. (2010) The Fracture Process Zone in Asphalt Mixture at Low Temperature”. Engineering Fracture Mechanics, Vol. 77(7), pp. 1175-1190.

43. Lutif, J. E. S., Souza, F. V., Kim, Y. R., Soares, J. B., and Allen, D. H. (2010) “Multiscale Modeling to Predict the Mechanical Behavior of Asphalt Mixtures.” *Transportation Research Record*, Vol. 2181 (3), pp. 28-35.

44. Marasteanu, M. O., Labuz, J. F., Dai, S., and Li, X., (2002) “Determining the Low-Temperature Fracture Toughness of Asphalt Mixtures”. *Transportation Research Record*, 1789, pp. 191–199.

45. Masad, E., Muhunthan, V., Shashidhar, N., and Harman, T. (1999) “Internal Structure Characterization of Asphalt Concrete Using Image Analysis.” *Journal of Computing in Civil Engineering*, 13(2), pp. 88-95.

46. Masad, E., Tashman, L., Little, D., and Zbib, H. (2005). “Viscoplastic Modeling of Asphalt Mixes with the Effects of Anisotropy, Damage and Aggregate Characteristics”. Journal *of Mechanics of Materials*, Vol. 37(12), pp. 1242-1256.

47. *MTOOL*: Bidimensional Mesh Tool, Versão 3.0. (1997) Grupo de Tecnologia em Computação Gráfica, TeCGraf5, Pontifícia Universidade Católica do Rio de Janeiro, Brazil.

48. Muhunthan, B., Masad, E., and Assaad, A. (2000) "Measurement of Uniformity and Anisotropy in Granular Materials." *Geotechnical Testing Journal,* 23(4), pp. 423-431.

49. Mura, T. (1987) "Micromechanics of Defects in Solids". 2nd Edition, Martinus Nijhoff Publishers, Dordrecht.

50. Needleman, A. (1987) "A Continuum Model for Void Nucleation by Inclusion Debonding". *Journal of Applied Mechanics,* Vol. 54, pp. 525-531.

51. Nemat-Nasser, S., and Hori, M. (1993) "Micromechanics: Overall Properties of Heterogeneous Materials". North Holland, New York.

52. Oden, J. T., Vemaganti, K., and Moes, N. (1999) "Hierarchical Modeling of Heterogeneous Solids". *Computer Methods in Applied Mechanics and Engineering,* 148, 367-391.

53. Park, S. W.; Kim, Y. R., and Schapery, R. A. (1996) "A Viscoelastic Continuum Damage Model and its Application to Uniaxial Behavior of Asphalt Concrete". *Mechanics of Materials,* Vol. 24, n.4, pp. 241-255.

54. Rabotnov, Y. N. (1969) "Creep Problems in Structural Members". North-Holland, London.

55. Romero, P. and Masad, E. (2001). “Relationship between the Representative Volume Element and Mechanical Properties of Asphalt Concrete.” *Journal of Materials in Civil Engineering*, 13(1), pp. 77-84.

56. Schapery, R. A. (1975) “A Theory of crack Initiation and Growth in Viscoelastic Media; Part I: Theoretical Development”. *International Journal of Fracture*, Vol. 11, n.1, pp. 141-159.

57. Schapery, R. A. (1984) “Corresponding Principles and a Generalized J Integral for Large Deformation and Fracture Analysis of Viscoelastic Media”. *International Journal of Fracture*, Vol. 25, pp. 195-223.

58. Schapery, R. A. (1990) “Simplifications in the Behavior of Viscoelastic Composites with Growing Damage”. *Proceedings of the IUTAM Symposium in Inelastic Deformation of Composite Materials*, troy, New York, pp. 193-214.

59. Seo, Y., Kim, Y. R., Witczak, M. W., and Bonaquist, R. (2002). “Application of Digital Image Correlation Method to Mechanical Testing of Asphalt-Aggregate Mixtures”. *Transportation Research Record*, 1789, pp. 162-172.

60. Seo, Y., Kim, Y. R., Schapery, R. A., Witczak, M. W., and Bonaquist, R. (2004). “A Study of Crack-Tip Deformation and Crack Growth in Asphalt Concrete Using Fracture Mechanics”. *Journal of the Association of Asphalt Paving Technologists*, 73, pp. 697-730.

61. Souza, F. V. (2009) “Multiscale modeling of impact on heterogeneous viscoelastic solids with evolving microcracks”. Ph.D. Dissertation, University of Nebraska–Lincoln.

62. Souza, F. V. (2005) “Modelo multi-escala para analise estrutural de compositos viscoelasticos susceptiveis a dano”. M.Sc. thesis, Universidade Federal do Ceara, Brasil. (In Portuguese).

63. Souza, F.V. and Allen, D.H., (2009) “Modeling failure of heterogeneous viscoelastic solids under dynamic/impact loading due to multiple evolving cracks using a two-way coupled multiscale”. *Mechanics of Time-Dependent Materials*, Vol. 14, Issue 2, pp.125-151.

64. Souza, F.V. and Allen, D.H., (2009) “Multiscale modeling of impact on heterogeneous viscoelastic solids containing evolving microcracks”. *International Journal for Numerical Methods in Engineering*, 82, pp. 464–504.

65. Souza, F. V. and Allen, D. H. (2011) “Computation of homogenized constitutive tensor of elastic solids containing evolving cracks”. *International Journal of Damage Mechanics, in print*.

66. Souza, F.V. and Allen, D. H. (2011) “Modeling the transition of microcracks into macrocracks in heterogeneous viscoelastic media using a two-way coupled multiscale model”. Submitted to the *International Journal of Solids and Structures*.

67. Souza, F. V., Allen , D. H., and Kim, Y. R. (2008) “Multiscale model for predicting damage evolution in composites due to impact loading”. *Composites Science and Technology,* Vol. 68(13), pp. 2624–2634.

68. Souza, F. V., Soares, J. B., Allen, D. H., Evangelista, F. (2004) “Model for Predicting Damage Evolution in Heterogeneous Viscoelastic Asphalt Mixtures”. *Transportation Research Record*, 1891, pp. 131-139.

69. Tashman, L., Masad, E., Little, D. N., and Lytton, R. L. (2004). “Damage Evolution in Triaxial Compression Tests of HMA at High Temperatures.” *Journal of the Association of Asphalt Paving Technologists*, Vol. 73, pp. 53-87.

70. Tvergaard, V. (1990) “Effect of Fiber Debonding in a Whisker-Reinforced Metal”. *Materials Science and Engineering*, Vol. A125, n. 2, pp. 203-213.

71. Wagoner, M. P. and Buttlar, W. G. (2007). “Influence of Specimen Size on Fracture Energy of Asphalt Concrete.” *Journal of the Association of Asphalt Paving Technologists*, Vol. 76, pp. 391-426.

72. Wagoner, M. P., Buttlar, W. G., and Paulino, G. (2005) “Development of a Single-Edge Notched Beam Test for Asphalt Concrete Mixtures”. *Journal of Testing and Evaluation,*Vol. 33, No. 6, pp. 1-9.

73. Weissman, A. L., Harvey, J., Sackman, J. L., and Long F. (1999). “Selection of Laboratory Test Specimen Dimension for Permanent Deformation of Asphalt Concrete Pavements.” *Transportation Research Record*, 1681, pp. 113-120.

74. Wen, H. and Kim, Y. R. (2002). “Simple Performance Test for Fatigue Cracking and Validation with WesTrack Mixtures.” *Transportation Research Record*, 1789, pp. 66-72.

75. Witczak, M. W., Bonaquist, R., Von Quintus, H., and Kaloush, K. (2000). “Specimen Geometry and Aggregate Size Effects in Uniaxial Compression and Constant Height Shear Tests.” *Journal of the Association of Asphalt Paving Technologists*, 69, pp. 733-793.